PhD Thesis

Mechanism of Liesegang Phenomenon Bifurcated by Thermodynamic Stability

熱力学的安定性で分岐するリーゼガング現象の機構解明

Masaki Itatani

Yamagata University, Graduate School of Science and Engineering

December 2021

Acknowledgement

First of all, I would like to express my sincere appreciation to my supervisor **Prof. Dr. Hideki Nabika** (Faculty of Science, Yamagata University), from the bottom of my heart, for his constant guidance, fruitful suggestions, encouragement, and precious discussion throughout this study.

I am also deeply grateful to **Prof. Dr. Jun Matsui** (Faculty of Science, Yamagata University), for his constant helps and substantial discussions, suggestions, physical and mental encouragements during the course of this study.

I am also grateful to **Prof. Dr. Qing Fang** (Faculty of Science, Yamagata University), for his kind comments, suggestion, supports, and guidance for numerical simulation in this study.

I am also grateful to **Dr. Kei Unoura** for his kind guidance, accurate comments, fruitful discussion, and encouragement.

I am also thankful to **Dr. István Lagzi** (Department of Physics, Budapest University of Technology and Economics), for his fruitful discussion, advice for the direction of this study.

I would also like to thanks to **Dr. Takanari Togashi** (Faculty of Science, Yamagata University), for his fruitful suggestions and comments.

I wish thanks to colleagues of Nabika lab.: **Mr. Yushiro Shimizu**, **Ms. Masayo Matsue**, **Mr. Daisuke Sato**, and **Mr. Kanta Tsukada** for giving me a lot of guidance and discussions in advancing this study. I would also like to thanks to the colleague of Nabika Lab., **Ms. Akane Iida**, for always stimulating my research life. Grateful is also extended other current and past members of Nabika Lab. for sharing a valuable and fulfilling time.

I also would like to express my gratitude to grant of **the Research Fellow grant of the Japan Society of the Promotion of Science** for full support to push forward with this research.

Finally, I would like to deeply appreciate to my parents (Masayoshi Itatani and Yuko Itatani), brother (Yoshiki Itatani), sisters (Haruna Itatani and Akina Itatani), grandfathers (Yoshitaka Itatani and Naoki Emori), grandmothers (Toshiko Itatani and Mariko Emori), and my wife (Rino Itatani) for their heartily helps and dedications.

December 2021

Masaki Itatani

Table of contents

Chapter 1 General Introduction

In nature, self-assembly and self-organization are central processes to form various structures. Dissipative structures, one of the self-organized structures, are ubiquitous in regardless nature and artificial systems.[1] Most of them are generated through bottom-up self-organizing processes under nonequilibrium conditions.[2-3] The meaning of dissipative structures ranges from temporal changes, such as rhythm formation,[4-5] to spatial changes such as pattern formation.[6-10] In this thesis, I focused on the latter spontaneously pattern formation phenomena. All that is needed to form them are carefully programmed initial conditions, triggers to execute them, and nonequilibrium environment to maintain their processes. They have precise structures and/or spatiotemporal periodicities on a wide range of scales from microscopic to the macroscopic scales.[11-12] There are two main attractions to such dissipative pattern formation. (i) All processes are spontaneous and do not require any additional operations other than an execution. Therefore, the mechanism of such formation provides us with simple ways to design complex and precise patterns. (ii) Most of the mechanisms are universal regardless of the target (but some require consideration of specific interactions). Namely, mechanisms can be generalized, and it allows to understand an origin of pattern formation that is ubiquitous among many disciplines. Given the above two attractive points, understanding the mechanism of spontaneous pattern formation will have an impact on researchers in all fields, including materials chemistry and natural science. However, it is difficult to prove the underlying mechanism because contained elements interact intricately and nonlinearly. Experimental and mathematical modeling are powerful tools for studying the mechanisms of these pattern formations (Figure 1.1).[13-18] This is because the effects of interactions can be examined separately and generalized mechanisms can be proposed based on them.

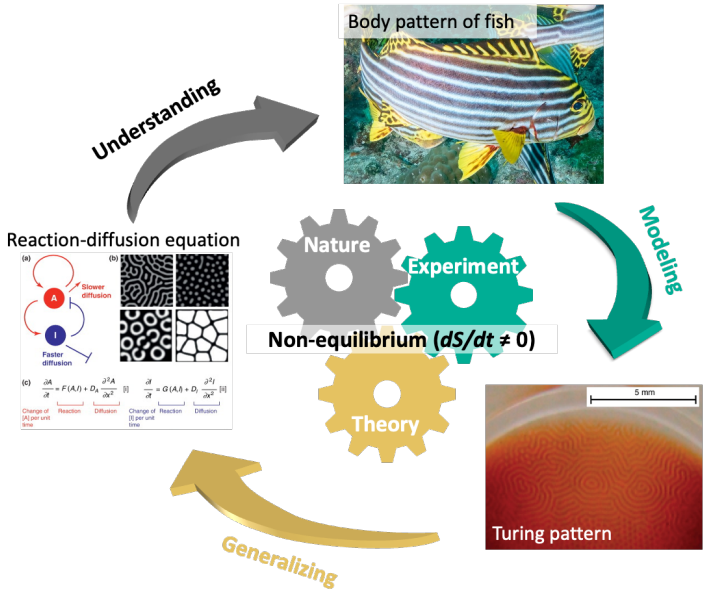

Figure 1.1. One of schemes of modeling study to prove the mechanism of pattern formations in dissipative systems. Turing pattern is adopted as an example for depicting this scheme. The first step is to determine a target (e.g. body pattern of fish) you want to study from various patterns in nature. As next step, an experimental model for the target (e.g. Turing pattern reprinted with permission from Ref. 18. Copyright 2011 American Chemical Society.) is built and the influence of key factors on pattern formation is verified. Then, obtained result are generalized by numerical simulations (e.g. reaction-diffusion equation reprinted with permission from Ref. 16. Copyright 2012 Elsevier.), which provides a universality of the constructed model. By comparing the model observations with the dynamics of the target (if possible) or natures, the formation mechanism can be proved.

Liesegang phenomenon is one example of a chemical model that possesses the ability to describe dissipative pattern formation arising from the coupling of mass transport with solid-phase transitions.[19-20] However, it lacks practicality as a model because of various conflicting theories regarding the formation mechanisms, even after 100 years since its discovery in 1896 by R. E. Liesegang. Therefore, the motivation of this thesis is to summarize various experimental and theoretical scenarios of Liesegang phenomenon so far, and to obtain the key to a comprehensive explanation of the formation mechanism. Toward this motivation, in the following sections, the thermodynamic basis of dissipative structure is firstly explained to understand the basic theory of dissipative structure formation. Then, several classes of dissipative structures are introduced with concrete examples, and the results of each model study are reviewed. Finally, after providing an extensive review of Liesegang phenomenon and the problems for proving the mechanism involved, the purpose of this thesis is stated.

1.1 Closed system and open system[1, 21-22]

When dealing with thermodynamic theory, a part of a subject whose thermodynamic properties are investigated is conventionally called a system, and the other part is called an externality. A system in which no energy or matter can enter or leave is called an isolated system, a system in which energy can enter and leave freely but matter cannot is called a closed system, and a system in which both energy and matter can enter or leave freely is called an open system. Dissipative structures are formed in an open system due to the constant dissipation of entropy. Namely, we should focus on the essence of difference among these systems. The entropy is the primary indicator that determines how chemical state in a system will spontaneously change to. Therefore, in order to better understand formation mechanism of dissipative structures, it is necessary to turn to the theoretical perspective of this phenomenon based on a relationship between system and thermodynamics of entropy.

1.1.1 Entropy[1, 21-22]

The direction of spontaneous change is related to the distribution of energy and matter, and spontaneous change always involves the dissipation or diffusion of energy and matter. In order to quantify this concept, it is necessary to introduce a physical quantity called "entropy", which is important to formulate the second law of thermodynamics, which defines the direction of spontaneous change of all events. Entropy (*S*) is a state function that describes the quality of energy of a system and is defined in terms of thermodynamic and statistical types as follows.

$$\text{Definition from thermodynamics: } \Delta S = \frac{\Delta q}{T} \qquad (1)$$

$$\text{Definition from statistics: } S = k_B \ln \mathcal{M} \qquad (2)$$

where Δq and T in eq. (1) are the sum of all heat transfers into and out of a system and temperature, and k_B and $\mathcal{M}$ in eq. (2) are the Boltzmann constant and the number of microstates compatible distribution of energy levels (i.e. degree of order in the system). Eq. (2) shows that entropy increases with the number of microscopic states (i.e., the number of molecular energy configurations when the total energy of a system is equal). When two systems with different temperatures are brought into contact, the heat will always diffuse from the higher temperature to the lower. The cause of this spontaneous change can be interpreted from eq. (2). Molecules in high temperature systems can exhibit a large number of energy levels due to their high molecular mobility, while in low

temperature systems, the number of energy levels is small due to reduced molecular mobility. The contact between the two systems increases the temperature of the system with the lower temperature, which increases the distribution of energy levels in the system and entropy. Namely, spontaneous change in a system is always governed by an increase in entropy. The second law of thermodynamics quantitively states a direction in which a system will spontaneously change from the entropy balance between a system and an externality, which is denoted as by using Gibbs free energy (ΔG) and enthalpy (ΔH)

$$\Delta G = \Delta H - T\Delta S \qquad (3)$$

As we can see from this equation, a system prefers the state with the highest entropy, namely the state with the lowest free energy. The second law of thermodynamics indicates that a system transits spontaneously toward the direction to the state with the lowest free energy, the steady state that is eventually reached is called the equilibrium steady state. Therefore, self-assembly in a system under equilibrium conditions is dominated by this principal in which entropy plays a leading role.

1.1.2 Thermodynamic states under equilibrium and nonequilibrium conditions[1, 21-22]

An assembling and organizing behaviors depend on final thermodynamic states in a system, in which there are four main types of thermodynamic steady states: the entropy change disappears ($dS/dt = 0$, the equilibrium steady state), becomes constant (*dS/dt = constant*, the nonequilibrium steady state), becomes periodic (*dS/dt = periodic change*), and becomes chaos (*dS/dt = chaos*). This difference between these steady states depends on the natures of the system. In a typical experiment conducted in a container such as a beaker or flask under constant temperature and constant pressure conditions, the system is basically considered as a closed system (Figure 1.2a).

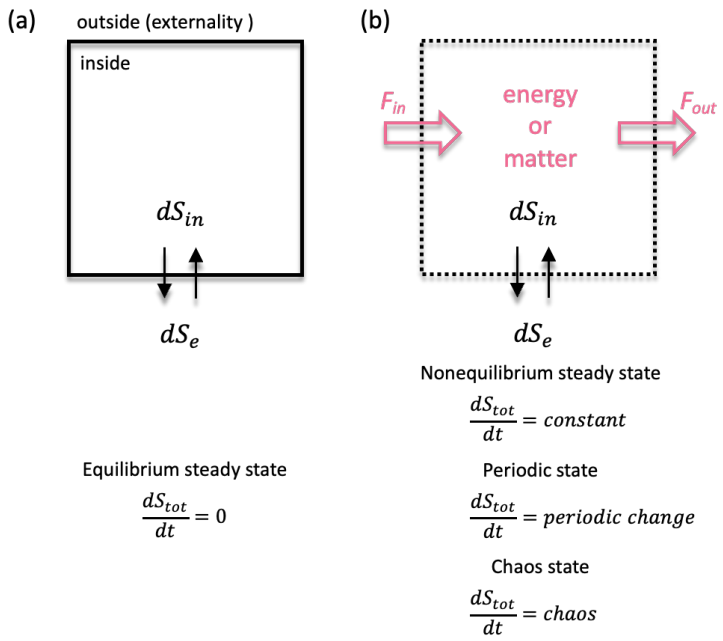

Figure 1.2. (a) Illustration of examples of the closed system and (b) the open system. The description at the bottom of each system represents the possible final state of the system. S_{in} and S_e are entropy inside and outside of the system, and S_{tot} is total entropy. Also, F_{in} and F_{out} represent fluxes corresponding to the supply and discharge of energy and matter.

Generally, a chemical process is an irreversible process that is entropy is produced. Inside of the system therefore generates entropy by various chemical processes such as chemical reactions, namely dS_{in} always becomes positive values ($dS_{in} > 0$). On the other hand, dS_e represents the entropy change of the eternality due to the exchange of matter and energy between the externality and the system. Therefore, dS_e can be positive or negative. In this case, the total entropy change of the system (dS_{tot}) is as follows:

$$\frac{dS_{tot}}{dt} = \frac{dS_{in}}{dt} + \frac{dS_e}{dt} \qquad (4)$$

When chemical processes are begun in the system, dS_{in}/dt becomes positive ($dS_{in}/dt > 0$) and dS_{tot}/dt changes to positive ($dS_{tot}/dt > 0$), namely spontaneous changes proceeds. Whereas dS_e/dt must be positive to initiate a spontaneous change without chemical processes ($dS_{in}/dt = 0$). In a closed system with chemical processes, dS_{tot}/dt mostly depends on dS_i/dt since there is no external supply of energy or matter. Therefore, the system finally represents the equilibrium steady state when the production of entropy from the system finish ($dS_{in}/dt = 0$) by reaching chemical processes to the equilibrium. On the other hand, the open system is realized by cutaneous supplying energy or matter

from the externality and discharging them from the system (Figure 1.2b). Namely, the flux of energy or matter is imposed in the open system. Since the chemical process is maintained by the flux from the externality, dS_{in}/dt is always positive and will never converge to zero unlike the closed system. Furthermore, dS_e/dt also keeps changing because there is a constant exchange of energy with the externality. Therefore, dS_{tot}/dt does not converge to zero, indicating that entropy is produced constantly in the open system. There are three main types of entropy production behavior, depending on the degree of imposed nonequilibrium. If the flux is relatively low and it is kept constant, the rate of entropy production in the system will be constant ($dS_{tot}/dt = constant$), in which this state is called a nonequilibrium steady state. Further enhancing the flux, chemical processes in the system exhibit cooperative dynamics, resulting in competitive changes in dS_{in} and dS_e. Thus, dS_{tot}/dt is modulated periodically ($dS_{tot}/dt = periodic\ change$), meaning that the system becomes a periodic state. In this state, the system exhibits the macroscopic coherent dynamics such as oscillation or pattern formation. If the flux is further enhanced from this situation, the order of entropy generation in the system is no longer maintained and the system becomes chaotic.

1.2 Self-assembly and self-organization

Building blocks (e.g. molecules, particles, cells, etc.) assembles depending on the thermodynamic state of the system, which forms various static or dynamic structures from micro (as well as molecular size) to macroscale.[12] I. Prigogine, a Belgian chemist who was awarded the Nobel Prize in Chemistry in 1977, reported that macroscopic spatiotemporal periodicity far beyond the size scale of building blocks appear in far-from-equilibrium states, such as open systems.[1] Different from equilibrium structure that follows the second law of thermodynamics, the building blocks work cooperatively to form such a macroscopic periodic structure which is called a dissipative structure. Therefore, the assemble process to form an equilibrium structure according to thermodynamic laws is called self-assembly, and the organization process under nonequilibrium conditions to form a dissipative structure is called self-organization. This distinction can be summarized in Figure 1.3.[23]

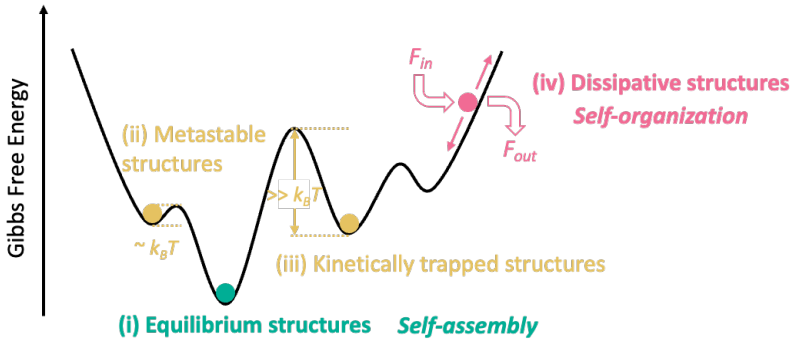

Figure 1.3. Difference between self-assembly and self-organization based on a perspective of Gibbs free energy. Characteristic structures are identified as four classes: (i) Equilibrium structure, and kinetic stabilization structures such as (ii) Metastable structures and (iii) Kinetically trapped structures, and (iv) Dissipative structurers that are structures specific to an open system.

Although an equilibrium structure is eventually formed depending on the experimental conditions (class (i)) in a closed system through self-assembling processes, it may go through several kinetically stabilized pathways to reach its structure (class (ii) and (iii)). These kinetic pathways identified based on energy barrier: (ii) Metastable structure is formed when the barrier is sufficiently low (namely almost equals to k_BT), whereas (iii) Kinetically trapped structure is formed when the barrier is high ($>> k_BT$). In the former case, the system relaxes spontaneously and slowly, eventually reaching an equilibrium structure. However, the latter is kinetically trapped, so no spontaneous structural relaxation occurs. Therefore, thermal perturbations from the outside are needed to promote relaxation of this structure. Since both kinetically stabilized structures are steady states in which no entropy generation occurs and can be regarded as transient structures on the way to equilibrium, they will not be treated primarily in this paper. On the other hand, a dissipative structure is formed in only an open system through self-organization processes (class (iv)). During self-organization, entropy is constantly generated due to the constant supply and discharge of energy and material fluxes. Therefore, the structure formed in this state is very unstable, not located in the energy groove, and requires a constant flux to maintain it. Thus, self-assembled equilibrium structures and self-organized dissipative structures are essentially different, the properties of those structures should be discussed separately.

1.3 Equilibrium and dissipative structures

To explain the difference of property between equilibrium and dissipative structures, we take Rayleigh-Bénard[24-25] convection as an example (Figure 1.4).

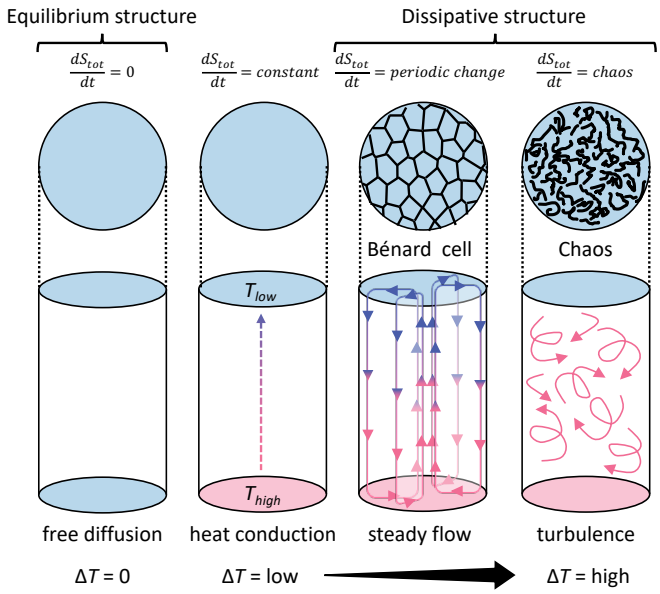

Figure 1.4. Transition of convection patterns with an increase in ΔT. When $\Delta T = 0$, there is no convection in the solution. When ΔT is applied, depending on its intensity, the structure transitions in the following order: heat conduction without convection, formation of convection pattern by steady flow, and formation of chaotic pattern by turbulence.[26]

Water in a vessel shows a liquid state under constant temperature ($0 < T < 100$ ˚C) and pressure (1 atm), meaning that these conditions represent that this vessel is a closed system. In water, H_2O molecules are molecular motion, but there is no change in structure in bulk scale, namely, water in such a solution state is the equilibrium structure. On the other hand, continue to heat the bottom of the vessel to impose a temperature gradient in the solution, and the system transition to an open system. When ΔT = low, the bulk water also shows the liquid state with no apparent change in appearance, however a heat conduction from the bottom of the vessel with high T to the top with low T occurs in water. At first glance, the bulk structure resembles an equilibrium structure, but this state is classified as a nonequilibrium steady state because it contains a constant entropy production mechanism due to heat conduction. When we increase ΔT further by heating temperature of the bottom, the uniform solution state is broken (i.e. entropy production is non-stationary.) and Rayleigh-Bénard convection as a steady flow occurs which promotes heat conduction. This convection is formed by macroscopic cooperative motion induced by ordered microscopic random molecular motion. Therefore, this structure deviates from

the second law of thermodynamics, and the macroscopic structure formed in such a far-from-equilibrium state is called a dissipative structure. In addition, a pattern called a Bénard cell is also formed due to this convection on the surface of a solution where Rayleigh-Bénard convection is occurring. Also, ΔT increases higher and higher, steady flow is broken and turbulence appears in the solution and a chaos pattern is formed on the surface of solution, in which entropy production rate become chaotic change in this state. Thus, the thermodynamic state of the system determines whether the emerging structure is an equilibrium structure or a dissipative structure. In particular, dissipative structures form only under certain imposed nonequilibrium conditions, which are due to the cooperative ordering of molecules that does not obey thermodynamic laws.

1.3.1 Example and property of equilibrium structures

In the preceding introduction of both structures, how the structural transition occurs is explained by the appearance of convection associated with closed and open systems. In following sections of 1.3.1 and 1.3.2, we focus on specific examples and details of each structure. Figure 1.5a-c shows examples of equilibrium structures.

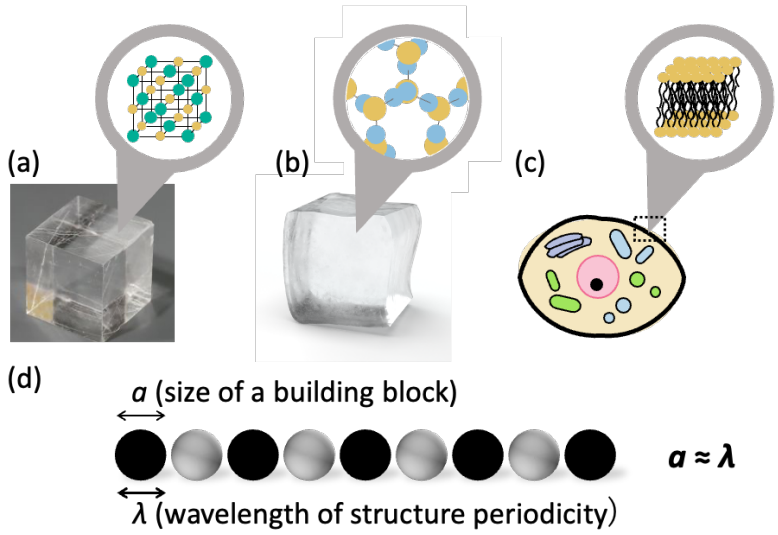

Figure 1.5. Examples of equilibrium structures: (a) NaCl crystal, (b) ice, and (c) living cell. Each enlarged illustration represents the crystal structure of NaCl, hydrogen-bonded network in an ice, and lipid bilayer structure at the cell membrane, respectively. (d) Structure property of an equilibrium structure.

As exemplified by the crystal structure and hydrogen-bonding network (Figure 1.5a,b), an equilibrium structure generally has robust structures. Due to this robustness, a shape of equilibrium structure shows high stability to perturbations such as mechanical strength and thermal resistance. Cell membrane is also one of the equilibrium structures (Figure

1.5c). Cell membrane has softness different from the crystal structure, mechanical strength is not that high. However, it serves as a stable barrier between the inside and outside of the cell, utilizing the hydrophilic effect of lipid molecules, and the barrier does not collapse spontaneously. Namely, what an equilibrium structure have in common is that they are very stable to perturbations from changes in the surrounding environment, and their structure is determined based on the equilibrium steady state. In addition, equilibrium structures also show characteristic periodicity (Figure 1.5d). In equilibrium structures, a wavelength of structure periodicity (λ) is almost equivalence to the size of a building block (a), such as ion, atom, and molecule in Figure 1.5a-c. Indeed, NaCl crystal is consisted of an assembles of alternating Na^+ and Cl^- bonds.

1.3.2 Example and property of dissipative structures

On the other hand, a dissipative structure has quite different property from an equilibrium structure. Figure 1.6a-d shows examples of them.

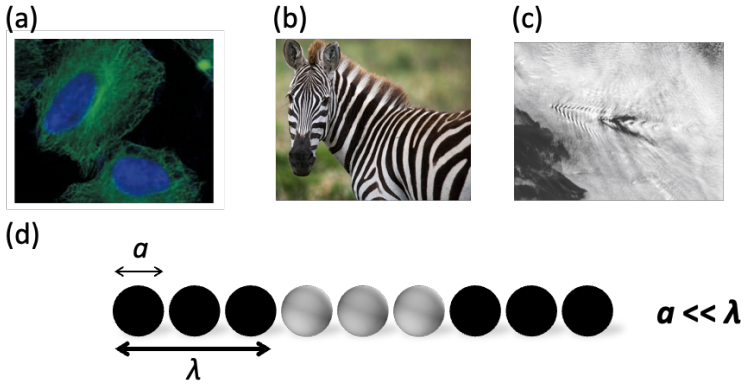

Figure 1.6. Examples of dissipative structures: (a) microtubes network structure reprinted with permission from Ref. 27. Copyright 2010 Springer Nature, (b) body pattern of animal, and (c) Kármán vortex reprinted with permission from Ref. 28. Copyright 2014 Springer Nature, (d) Structure property of a dissipative structure.

During the cell cycle, microtubes form a characteristic microtube structure as shown Figure 1.6a.[27] In this structure, microtubules assemble throughout the cell and form a network of them with spatial scales much larger than a single microtubule. Also, body patterns of animal are other typical examples for dissipative structures. For example, most of zebra has stripe pattern with alternating black and white on a body surface (Figure 1.6b). Each region is not composed of a single pigment cell, but of an assemble of each cell.[16-17] Same as the Rayleigh-Bénard convection described above, most convection patterns can be classified as dissipative structures, in which Kármán vortex is one of them (Figure 1.6c).[28] Such macroscopic convection structures are created when building

blocks (e.g., molecules, particles, and gases) interfere with each other and motioned cooperatively. Therefore, the key word in a dissipative structure is "coherence" and " cooperation" between building blocks. Thus, a dissipative structure shows interesting λ in which an assembly of building blocks with size a per a building block is distributed periodically (Figure 1.6d). This property leads to the bottom-up formation of dissipative structures at various scales from nano to micro regardless nature and artificial systems.[12] It is noted that dissipative structures is basically unstable to perturbations, namely stational structure requires maintaining an open system.

1.4 Dissipative structure formation via reaction-diffusion processes

In the previous sections, we have explained the property of the dissipative structure. In this section, a reaction-diffusion process (RD), which is actually the primary process that drives dissipative structure formation, is described. The RD process works through the cooperative interaction of reaction and diffusion of substances in a system.[9, 12, 17, 29] The system containing the RD process is called the RD system. In this system, the change in concentration of a substance (X) is a conjugated state caused by both reaction and diffusion, and the change in concentration of X is described as the sum of the two as follows:[30]

$$\left(\frac{\partial X}{\partial t}\right)_{total} = \left(\frac{\partial X}{\partial t}\right)_{reaction} + \left(\frac{\partial X}{\partial t}\right)_{diffusion} \qquad (5)$$

This equation, called the reaction-diffusion equation, is the basic form for describing phenomena in RD systems, and by reflecting information on the specific dynamics to each term, we can understand various RD phenomena.[31] RD processes form various attractive dissipative structures with temporal and/or spatial periodicities (Figure 1.7).

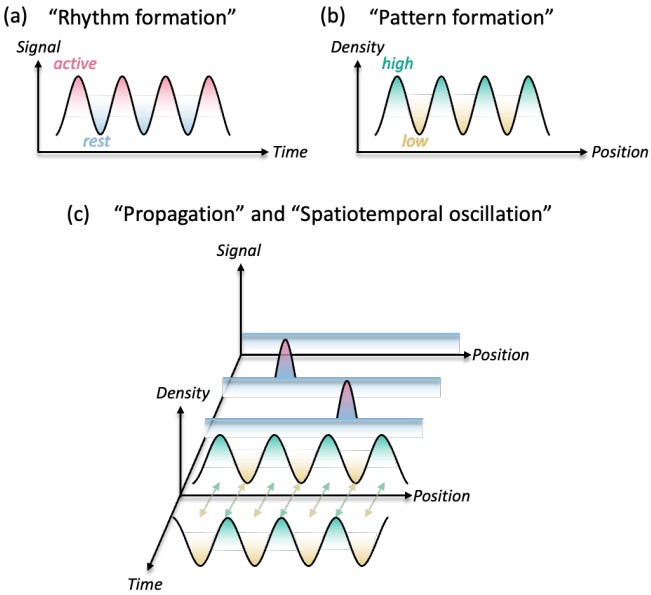

Figure 1.7. Various dissipative structures in RD systems: (a) Rhythm formation, (b) Pattern formation, and (c) Propagation phenomenon and Spatiotemporal oscillation.

Rhythm formation represents that a signal of activity modulates oscillatory with time, namely active and rest states repeat alternately (Figure 1.7a). Such rhythm is particularly ubiquitous in biological phenomena such as the heartbeat and cellular organization activities.[32-33] Pattern formation is another characteristic type of RD phenomenon (Figure 1.7b), which indicates that density or concentration of a component distributes discretely (in some cases, the two types of components are distributed alternately). The body surface pattern of animals is a typical example of this class,[15-17, 34] and pattern formation is also ubiquitous in other living and inanimate systems. Furthermore, the coupling of the above two classes forms a more complex structures, which are propagation phenomenon and spatiotemporal oscillation (Figure 1.7c). The characteristic feature of this special class is that the component concentration (density) changes with temporal periodicities. Also, the fascinating aspect of the study of dissipative structure formation in RD systems is that the pattern formation of each of the above classes can be modeled experimentally and mathematically. The following table lists the corresponding model systems and their characteristics.

Table 1.1 Spatiotemporal periodic dissipative phenomena in RD systems and corresponding models.

	Rhythm	Spatiotemporal pattern	Pattern	Pattern with solid-phase
Nature	Heartbeat…etc	Neuron network…etc	Body pattern…etc	Rock pattern…etc
Model	← Belousov-Zhabotinsky reaction →		Turing pattern	Liesegang phenomenon
Reaction process	← Positive and negative feedback →			Irreversible precipitation
Requirement	← Constant nonequilibrium →			Transient nonequilibrium

Rhythm formation and spatiotemporal pattern formation, such as heartbeats and neuron networks, are modeled by the Belousov-Zhabotinsky reaction.[13, 35-37] Also, pattern formation such as body patterns of animal is modeled by Turing pattern.[10, 14-18, 34, 38] These three reaction processes have positive and negative feedbacks and need to be maintained in a constant state of nonequilibrium conditions (mainly flux of substances) to sustain their competition. On the other hand, there is a class that do not require this condition to maintain a pattern, which is pattern formation with solid-phase transition by precipitation. Since this type of patterning involves irreversible precipitation as a reaction process, the structure is locked. Namely, the structure of such pattern reflects the transient nonequilibrium conditions during the progression of precipitation. Such pattern is seen as rock patterns and modeled by Liesegang phenomenon.[19-20]

1.5 Experiments and numerical simulation for reaction-diffusion patterns

Many of the aforementioned RD dissipative structures in nature deeply involves in biological phenomena and construct the hierarchical structure in nature, that is, RD phenomena play a crucial role in nature. Also, all processes for the formation are spontaneous and do not require any additional operations other than execution of pattern formation.[11] Nevertheless, it is possible to self-organize highly ordered structures like the above RD structures thorough bottom-up processes. Therefore, understanding the mechanism of RD dissipative structures will not only lead to an understanding of the fundamentals of pattern formation in nature, but also to the creation of novel ordered materials by applying these mechanisms. However, underlying mechanisms are so complex that it is difficult to understand them directly. Then, experimental and mathematical modeling becomes powerful tools for revealing their mechanisms because

it is possible to examine each of the elements necessary for pattern formation separately, and to propose a generalized mechanism based on this.

1.5.1 Belousov-Zhabotinsky reaction

The Belousov-Zhabotinsky (BZ) reaction has established itself as a typical model for the formation of rhythms and spatiotemporal periodic patterns,[13, 35-37] which is discovered by B. P. Belousov and A. M. Zhabotinsky who are soviet chemist. BZ reaction consists of a complex chemical reaction network with a feedback mechanism as shown in Figure 1.8a, in which the oxidation-reduction reaction of metal ions is repeated. Thus, bulk BZ solution shows a temporal periodic change in color due to the redox state of metal ion (Figure 1.8b).[39]

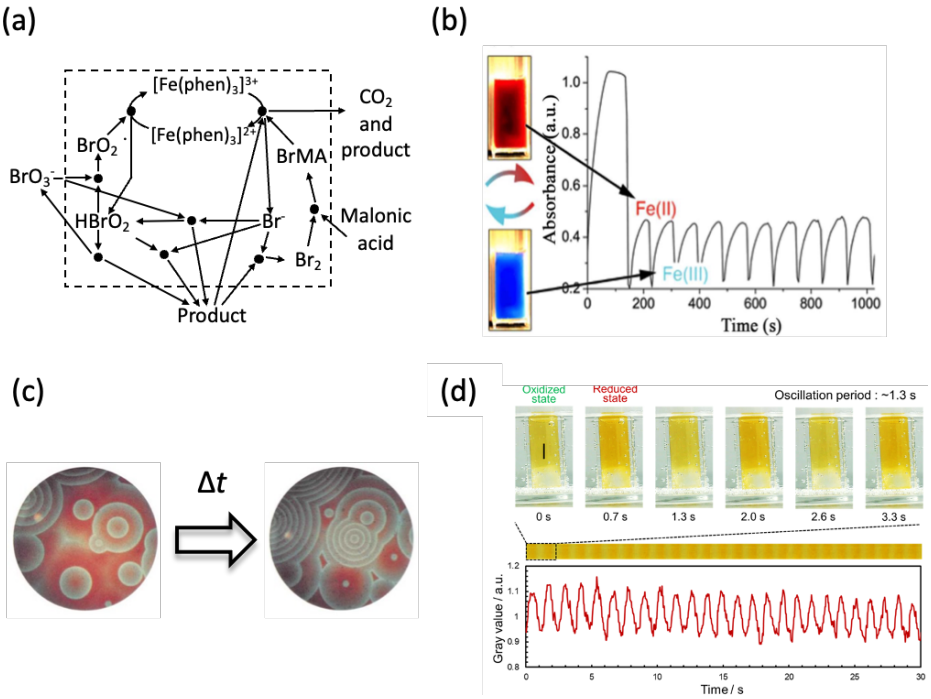

Figure 1.8. (a) Chemical reaction network in Belousov-Zhabotinsky (BZ) reaction. (b) Oscillation of color change in BZ solution reprinted with permission from Ref. 39. Copyright 2017 Royal Society of Chemistry. (c) Spatiotemporal BZ pattern in 2D reprinted with permission from Ref. 13. Copyright 2003 Royal Society of Chemistry. (d) Example of application of BZ reaction: Hydrogel with high-frequency swelling/deswelling following BZ oscillation reprinted with permission from Ref. 41. Copyright 2021 American Chemical Society.

When this solution is confined to a thin layer in a 2D space like a Petri dish, a BZ pattern is obtained in which periodic redox changes propagate through space (Figure 1.8c).[13] Furthermore, the coupling of BZ oscillation and changes in the mechanical properties of gels has created application objects with various self-sustaining mechanisms.[40-41] Figure

1.8d shows one example of such applications: creation of a hydrogel with high-frequency swelling/deswelling following BZ oscillation similar to heartbeats frequency. In addition to the BZ reaction, many other systems that exhibit chemical oscillations have been reported,[42] but most of the systems that exhibit rhythms, including the BZ reaction, have autocatalytic processes in the elementary reaction process. Brusselator and Oregonator are known as preferred numerical model to describe the dynamics of autocatalytic reaction processes.[43-44] For numerical simulations for BZ reaction, Brusselator and Oregonator are coupled with RD equation.[45-47] Figure 1.9 shows one example of the simulation result by using these techniques.[48]

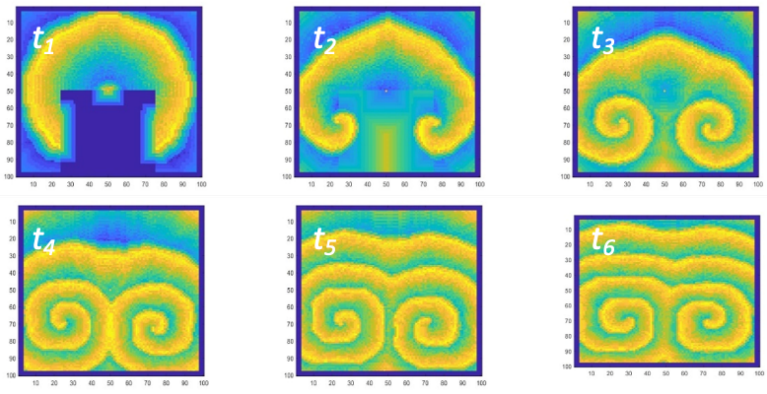

Figure 1.9. Time evolution of BZ pattern in the numerical simulation based on Oregonator model.[48]

These simulation results have reproduced well the self-organization dynamics and spatiotemporal periodicity of BZ oscillations and patterns. Thus, the experimental results and the mathematical model have been refined in BZ reaction. Therefore, the understanding of the mechanism is progressed, and many strategic approaches have been made for not only understanding the spatiotemporal dynamics exhibited by living organisms[49-51] but also the application as shown above.

1.5.2 Turing pattern

Turing pattern (TP) is a typical model for describing static RD pattern formation, whose mechanism is firstly proposed by A. M. Turing.[10, 14-18, 34, 38] In TPs formation, periodic structures are formed spontaneously from a uniform field by uniformly mixing active and inhibitory species that control each other's reactions through interaction. Although contained reaction processes is almost same as BZ reaction, TP is formed only when the diffusion coefficients of the interacting chemical species are significantly different. The main feature of TPs is that they can form patterns with various morphologies that are fixed in space. Figure 1.10 shows various morphologies of TPs formed experimentally by

changing concentrations of reagents.

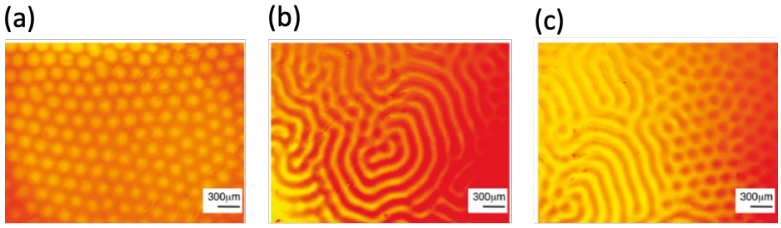

Figure 1.10. Various morphologies of TPs: (a) Hexagonal pattern, (b) Labyrinth pattern, and (c) Coexistence of the hexagonal and labyrinth patterns, reprinted with permission from Ref. 18. Copyright 2011 American Chemical Society.

The most important achievement in research on TP is the discussion of the mechanisms of these various pattern formations through numerical simulations based on RD equation, and the application of these findings to the demonstration of the mechanisms of body surface pattern formation of animals. This attempt was firstly made by S. Kondo et al..[14, 16] Figure 1.11 shows summery of numerical simulation to describe TP formation.[52]

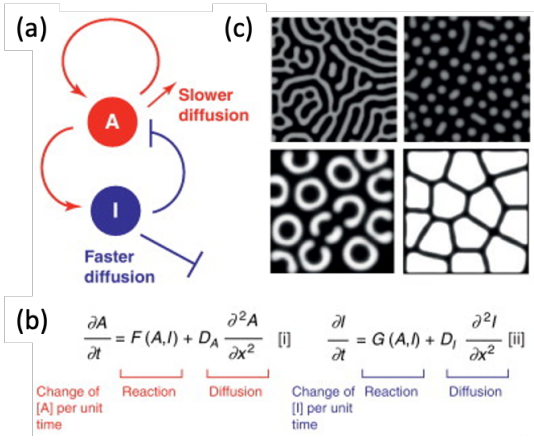

Figure 1.11. (a) Turing's RD model has at least two components, an activator (A) and an inhibitor (I). (b) Turing's equation. The change in [A] and [I] per unit time is determined by the reaction (the relationship between A and I) and the diffusion of A and I in unit space. For a Turing wave pattern to emerge, function F is defined so that [I] is inversely proportional to [A], and function G is defined so that [I] is positively dependent on [A]. (c) Turing's model can produce striking two-dimensional spatial patterns by varying various parameters. Many of these patterns resemble the spots and stripes found in nature, such as the stripes of a fish or the mesh pattern of a giraffe. This figure was reprinted with permission from Ref. 52. Copyright 2012 Elsevier.

It is noted that the system must be kept open conditions in order to maintain the structure of the BZ pattern and TP. To achieve it, continuous stirred tank reactor (CSTR) is used.[53-54] Thus, the structure of both depends on the F_{in} and F_{out} of substances, which is controlled by the CSTR. As described above, the mechanisms of both BZ reaction and TP are very well understood from both experimental and theoretical perspectives, and both

have already acquired practicality as models to explain RD dissipative structures such as rhythms, spatiotemporal patterns, and static patterns in nature.

1.6 Liesegang phenomenon

Liesegang phenomenon is a typical example to describe dissipative pattern formation with solid-phase transition, which is firstly discovered in 1896 by R. E. Liesegang.[19-20] This phenomenon is cause in the case of coupling of diffusion flux by directional mass transport into porous media (typically a hydrogel) with solid-phase transition processes. The obtained pattern by this phenomenon is called Liesegang pattern (LP), which shows an array of well-defined regular discrete precipitation bands (rings). A typical experimental set-up for LPs formation and property of obtained pattern is shown in Figure 1.12.

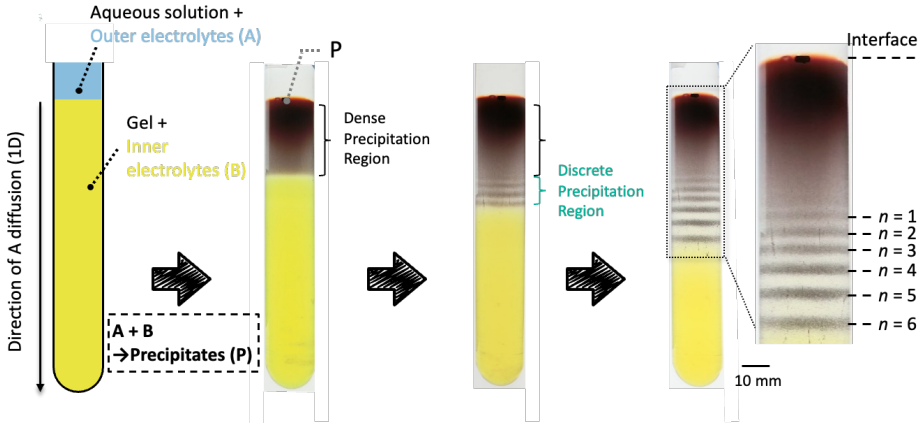

Figure 1.12. Typical experimental set-up for 1D LP formation (left) and evolution of pattern formation. Right image shows obtained 1D LP finally.

Firstly, a reservoir (typically aqueous solution) contained with metal ions (A) that is so-called outer electrolytes is poured on the top of a hydrogel made in elongated container (typically test tube). The gel is pre-doped with counter ions to A (B) that is so-called inner electrolytes (Figure 1.12 left). Subsequently, A diffuse into the gel media, where it reacts with pre-doped B to generate precipitates (P). Since A invades directionally into the gel according to Fick's diffusion law,[55] a diffusion concentration gradient is formed in the gel. Since P is generated with the diffusion, appearance of precipitation region propagates toward the bottom of the test tube, where head of the propagation is called as precipitation or reaction front. Near an interface between outer electrolytes solution and the inner electrolytes gel, diffusion flux of A (F_{diff}) is higher than a position closer to the bottom due to the diffusion gradient. Thus, the precipitation reaction proceeds rapidly there,

forming a continuous precipitation region. However, a region of discrete precipitation is formed in the region below the continuous region where the F_{diff} is somewhat lower, because of the exquisite competition between diffusion and reaction rates. Once a discrete band structure begins to form, the band formation is repeated in subsequent regions. Thus, the end result is a periodic precipitation pattern with several alternating bands (Figure 1.12 right), which can be clearly numbered using band number (n).

1.6.1 Empirical laws in Liesegang phenomenon

As an important point in Liesegang phenomenon, most of obtained LPs according to the above experimental set-up show well-defined spatiotemporal properties, which are represented as empirical laws. Information for each law is summarized in Figure 1.13.

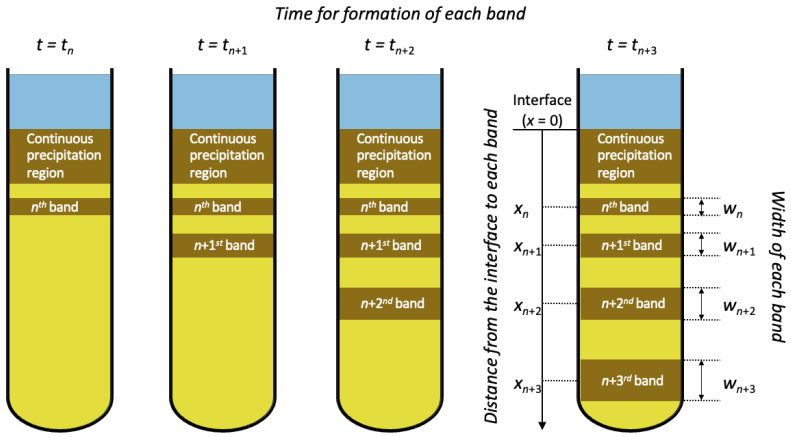

Figure 1.13. Information for empirical laws in in Liesegang phenomenon. The interface between the outer and inner electrolytes is defined as $x = 0$. The band position, width, and time for formation of the n^{th} band are x_n, w_n, and t_n, respectively. There are three empirical laws for concerning x_n, w_n, and t_n are known as spacing, width, and time laws, respectively.

The most famous of these is the spacing law (eq. (6)), which defines the spatial periodicity of each band of LP.[56]

$$\lim_{n\to\infty} \frac{x_{n+1}}{x_n} = 1 + p \qquad (6)$$

where x_n, x_{n+1}, and p are the distance from the interface between the invading and pre-doped electrolytes to the n^{th} and $(n+1)^{st}$ bands, and the spacing coefficient, which is constant at large values of n, respectively. From this equation, it is found that the precipitation region in the typical Liesegang set-up is formed alternately following geometric series. Also, an inter-band spacing Δx_n ($= x_{n+1} - x_n$) is represented by converting eq. (6) as below:

$$\Delta x_n = p x_n \qquad (7)$$

This equation indicates that Δx_n of typical LPs increase linearly with the increase of x_n. Since most experimental results follow eqs. (6) and (7), the spacing law has been widely used to study the Liesegang phenomenon. Furthermore, the effect of experimental conditions on the pattern geometry can be evaluated by using p as an indicator of evaluation.[57-60] Also, the value of p depends on concentrations of outer and inner electrolytes, which is known as Matalon-Packter (MP) law[61-62] denoted as

$$p = F(b_0) + G(b_0)\frac{b_0}{a_0} \qquad (8)$$

where a_0 and b_0 are the initial concentration of the outer electrolytes and the pre-doped concentration of inner electrolytes, respectively, and F and G are monotonously decreasing functions of b_0. Since a_0 is a variable independent of the functions F and G, it is easy to demonstrate the relationship between a_0 and p. Actually, some experimental studies demonstrated this dependency and showed good agreement of results with the MP law.[63-64] In contrast, an effect of b_0 is complex because b_0 is involved in F and G. Indeed, several studies have shown two contrast effects on the change in p relative to b_0: an increase[65-66] and a decrease.[67] In addition, p is also depends on the some other experimental conditions (e.g. gel thickness,[68] pH,[69] temperature,[70] gel concentration,[71] and existence of electric field[66, 72-73]). Therefore, evaluation using the MP law is very empirical, and its application needs to be cautious. Furthermore, the periodicity of LPs with respect to time is also often evaluated, although not as much as the spacing law.

$$x_n \propto \sqrt{t_n} \qquad (9)$$

Eq. (9) is so-called the time law,[74-75] where t_n represents time for formation of the n^{th} band. This relationship is a straightforward reflection of a diffusive nature of the pattern formation mechanism, as the characteristic distance in diffusion is linearly proportional to the square root of time. Also, the width law[76-77] is known as other empirical laws following as:

$$w_n \propto x_n^{\alpha} \qquad (10)$$

where w_n is the width of nth band, and α is a characteristic coefficient. However, accurate measurement is difficult because the resolution of the bandwidth can easily change depending on the image acquisition settings such as exposure time and CCD sensitivity. Thus, this law is not used as often as other empirical laws. Also, it is known that under general conditions, α becomes close to 1.[77]

1.6.2 Various morphologies and materials for LPs formation

In aforementioned explanations are based on the 1-dimensional (1D) set-up, indicating the gel media is column shape and outer electrolytes diffuse only in one macroscopic direction. However, depending in gel shapes, morphologies of obtained LPs are controllable (Figure 1.14).

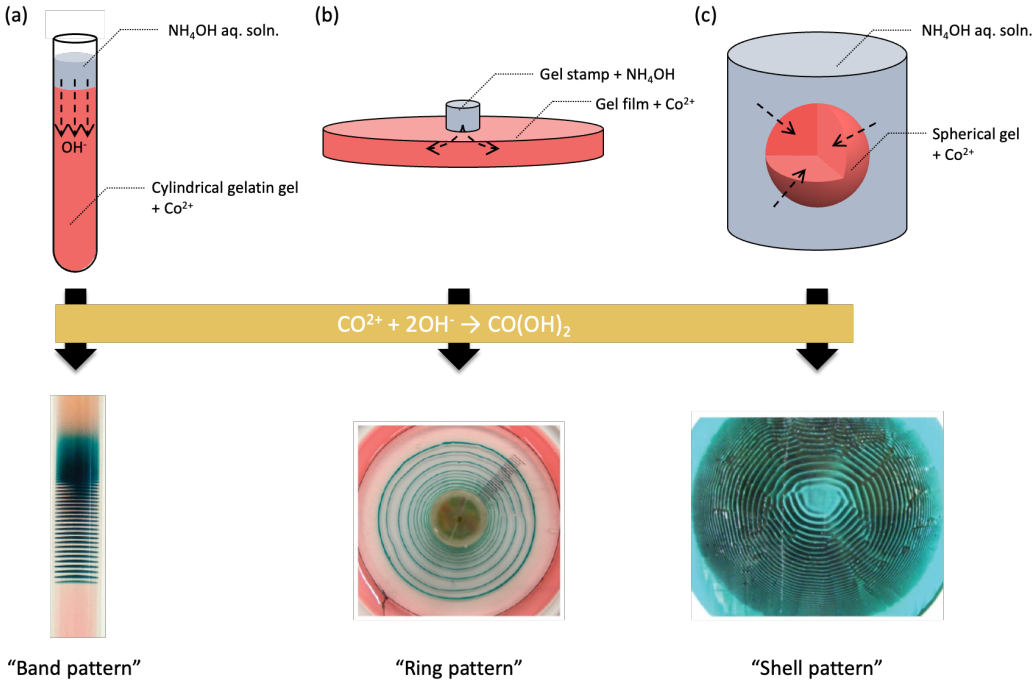

Figure 1.14. Various morphologies of LPs obtained by the reaction to generate $Co(OH)_2$ precipitates: (a) Band pattern in the 1D gel column reprinted with permission from Ref. 78. Copyright 2008 American Chemical Society, (b) Ring pattern in the 2D gel thin film reprinted with permission from Ref. 69. Copyright 2009 American Chemical Society, and (c) Shell pattern in the 3D gel sphere reprinted with permission from Ref. 85. Copyright 2011 American Physical Society.

When using. the1D set-up, the band pattern is typically obtained (Figure 1.14a).[71, 78] By placing a cylindrical gel (gel stamp) soaked with outer electrolytes at the center of the gel thin film doped with inner electrolytes, outer electrolytes can diffuse from the center of the gel thin film in the 2-dimensional plane direction (Figure 1.14b). This method is so-called the wet-stamping method.[79-81] As a result, obtained LPs show the ring pattern.[69, 82-84] However, note that if the gel film is too thick, the effect of diffusion in the film thickness direction become apparent. Also, the morphology is designable freely by tuning the stamp shape and way to array of multiple stamps.[79-80] When we use a gel sphere as the gel media for LPs formation, the 3D LP can be formed (Figure 1.14c).[85] In this experiment, the sphere gel doped with inner electrolytes is soaked in the bulk solution contained with outer electrolytes. Because the outer electrolytes invade into the gel from

the surround solution, the shell pattern is formed. Therefore, LP morphologies are very diverse, and it is needed to choose an experimental system depending on the desired morphology. In addition to the morphological characteristics of LPs, recent years have seen a lot of interest in materials that self-organize LPs (Figure 1.15). So far, sparingly soluble salt has been used as the conventional materials for LPs formation (e.g. copper chromate,[58, 63, 71, 86] silver chromate,[68, 87-89] and cobalt hydroxide[57, 66, 69, 78]). Recently, other functional materials are highlighted for LPs formation such as metal nanoparticles[59-60, 82, 90], metal-organic-frameworks (MOF)[91-93], polymers[94-96], and molecular crystal[97]. This is because Liesegang phenomenon has found its applicability in self-organizing pattern techniques and particle synthesis. LP formation is driven by a diffusion gradient, which imposes a gradient of supersaturation in the gel. As a result, different nucleation and particle growth rates are obtained depending on the distance from the interface with the diffusion source. This kinetic anisotropy allows various size and shape of nano and particles to be obtained during one pot procedure.[91, 93, 98-99]

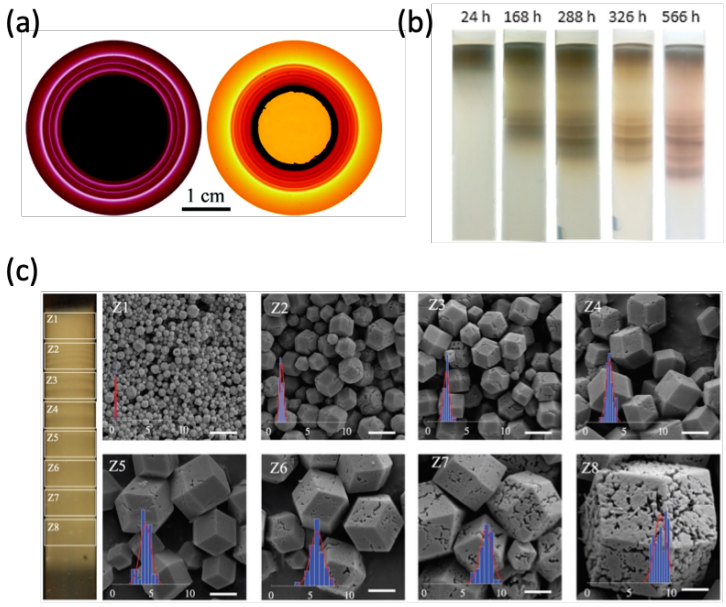

Figure 1.15. Formation of LPs from some functional materials. (a) Ring pattern made of oppositely charged nanoparticles: (left) gold nanoparticles and (right) silver nanoparticles modified by cationic and anionic alkane thiols, reprinted with permission from Ref. 90. Copyright 2010 American Chemical Society. One charged nanoparticle is pre-doped into the gel thin film, and the nanoparticle with the opposite charge is diffused from the center. (b) Band pattern engineered by poly(2-methoxyethyl acrylate) of hydrophilic polymer, which is obtained by diffusion of monomers under high temperature conditions into a gel containing a polymerization initiator. This image was reprinted with permission from Ref. 94. Copyright 2017 American Chemical Society. (c) Band pattern fomed by particles of zeolitic imidazolate frameworks. The size and shape are modulated depending on the position. This image was reprinted with permission from Ref. 91. Copyright 2019 John Wiley and Sons.

1.6.3 Various geometries of LPs

The above morphological changes are straightforward reflection of the effect of diffusion orientation, and although there are some differences,[85, 100] the obtained patterns basically satisfy the spacing law shown in eq. (6). However, LP sometimes show a special geometry regardless of experimental conditions (Figure 1.16).

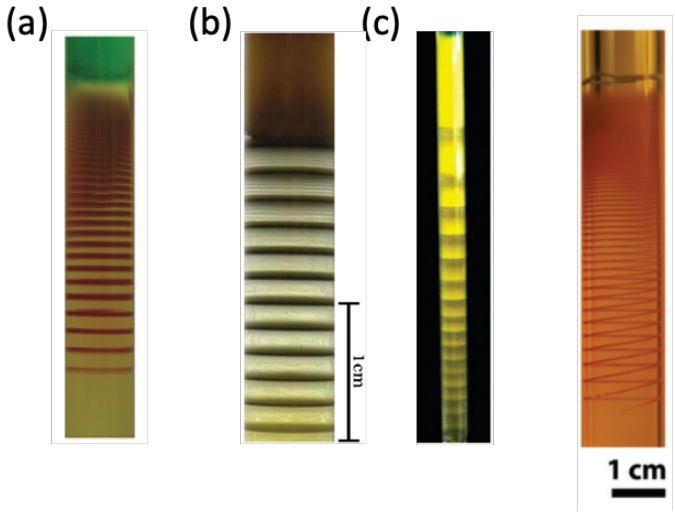

Figure 1.16. Various geometry of LPs. (a) Regular-type LPs (increasing Δx_n) of $CuCrO_4$, reprinted with permission from Ref. 71. Copyright 2012 American Chemical Society. (b) Equidistant-type (constant Δx_n) of $Ag_2Cr_2O_7$, reprinted with permission from Ref. 103. Copyright 2008 American Physical Society. (c) Revert-type LPs (decreasing Δx_n) of $PbCrO_4$, reprinted with permission from Ref. 108. Copyright 2011 American Chemical Society. (d) Helix-type LPs of $CuCrO_4$, reprinted with permission from Ref. 86. Copyright 2013 American Physical Society.

Figure 1.16a shows a typical obtained LP that obeying the spacing law, which is so-called a regular-type LP. While, Figure 1.16b,c shows exceptional examples in Liesegang phenomenon. Figure 1.16b shows an equidistant-type LP,[101-104] in which Δx_n is constant regardless of position. It was reported that controlling F_{diff} induced formation of this type. Also. Figure 1.16c represents a revert-type LP, in which Δx_n decreases with the increase in x_n. This exceptional periodical patterns were formed when AgI[105-107] and $PbCrO_4$[108-109] were selected as precipitation materials even though the experimental procedure was the same as for the regular-type experiment. The mechanism in these systems was discussed in terms of changes in the surface potential of colloidal particles as precursors of precipitates caused by the adsorption of excess ions, however the details remain to be elucidated. An important point in these three types of LPs mechanisms is that the factors determining the periodicity of the pattern are not clear. For example, the application of the electric field above did not form a revert-type. On the other hand, a reaction system that forms a revert-type will not form an equidistant-type. This inconsistency is very

strange, considering that both the strength of the electric field and the amount of ions adsorbed can be controlled to some extent by the experimental conditions. Therefore, whether the factors that determine these three types of LPs are unified or individual parameters needs to be further examined. Also, Figure 1.16d shows other special class of LP, that is helix-type.[64, 86] It was reported that emergence of this type was random, both regular-type and helix-type were formed under the same experimental conditions. However, factors that assist in the appearance of the helix-type have not yet been elucidated.

1.6.4 Analogy to pattern formation in nature

The reason why the Liesegang phenomenon is expected to be a model is that it shows similar morphology and periodicity to various periodic dissipative precipitation patterns that are ubiquitous in nature. Figure 1.17 shows such analogy between LPs and pattens in nature.

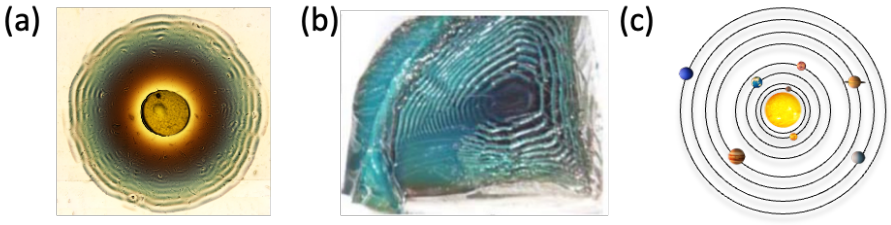

Figure 1.17. (a) Chemical 2D LP obtained from a reaction between Cu_2^+ and CrO_4^{2-}. Similar pattens in nature to LPs: (b) Ring pattern in agate rock, reprinted with permission from Ref. 112. Copyright 2018 American Chemical Society. (c) Planetary orbits in the solar system.

In agate rock, a ring-shaped discrete pattern similar to LP is formed.[110-112] Such patterns are formed by periodic precipitation of mineral components such as oxides, however the details of the formation mechanism have been uncleared. Also, planetary orbits in the solar system is one of the similar patterns (Figure 1.17c). Surprisingly, it was reported that Titius-Bode's law for the periodicity of orbits is consistent with the spacing law in the Liesegang phenomenon.[113] Direct observation of such geoscientific pattern formation is quite difficult because many events take place over a wide range of spatiotemporal scales. Therefore, the Liesegang phenomenon that has much in common with these patterns is expected to be applied as a practical model for elucidating these formation mechanisms. However, it lacks practicality as a model because of some conflicting theoretical scenario regarding the formation mechanisms, even after 100 years since its discovery in 1896 by R. E. Liesegang. Furthermore, there are still unexplained

phenomenon such as the change in geometry described above, even with each scenario. Therefore, it is needed to sort out the issues in each scenario and solve them from the ground up.

1.7 Bifurcated theoretical scenario for LP formation mechanism

1.7.1 Thermodynamics for precipitation

Reaction processes in most of the LPs include following processes:

(i) Chemical reaction: $A + B \rightarrow C$ (11)

(ii) Solid-phase transition (precipitation): $C \rightarrow P$ (12)

The first step (i) is chemical reaction between outer electrolyte (A) and inner electrolyte (B), and this reaction generates intermediate species (C) such as salt molecules or dispersible colloidal particles. Also, the second step (ii) represents a solid-phase transition precipitation process to form non-diffusive precipitates (P) from C. As In the phase transition process for such LP formation, two main pathways based on different scenarios have been proposed: nucleation based on classical nucleation theory[62, 114-115] and phase separation based on spinodal decomposition theory.[116-117] It is known that such bifurcation occurs depending on the thermodynamic state of the system. [116-117] Figure 1.18 shows principle of this bifurcation and a phase diagram.

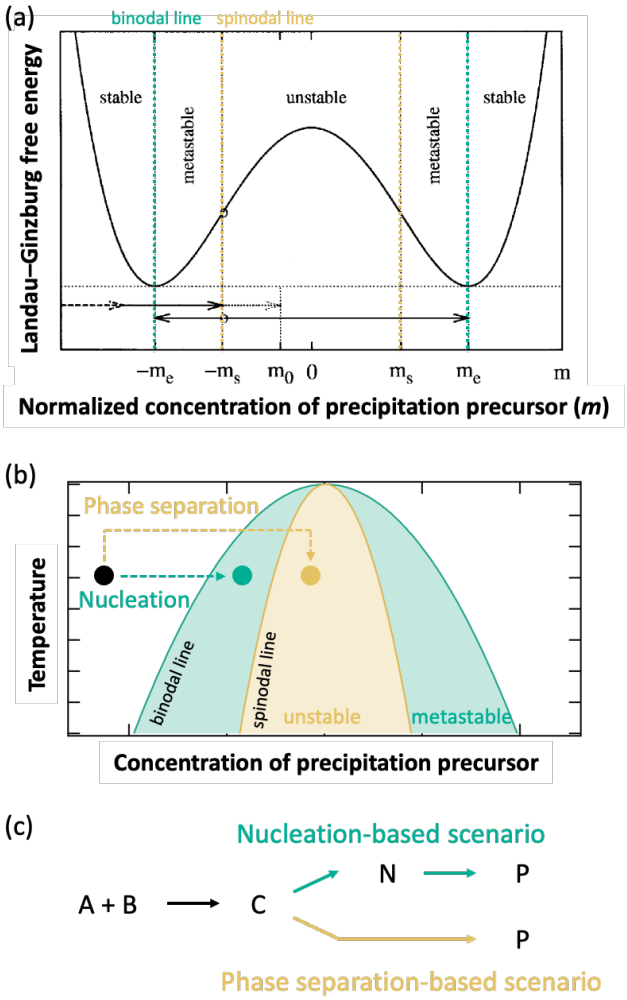

Figure 1.18. (a) Relationship between Landau–Ginzburg free energy ($\mathcal{F}$) and normalized concentration of precursor (m). The values of $\pm m_e$ are corresponding to the steady state with high (c_h) and law (c_l) concentrations. This image was reprinted with permission from Ref. 117. Copyright 1999 Elsevier. (b) Phase diagram of solid-phase transition. Phase separation based on spinodal decomposition is triggered under the unstable condition. Also, nucleation based on the classical nucleation theory is triggered under the metastable condition. (c) Bifurcated scenarios in LP formation mechanism. A, B, C, N, and P are outer, inner electrolytes, water soluble reaction inter mediate, nuclei, and precipitates.

In considering the two different scenarios we need to consider the dynamics of the phase transition and separation. However, we should explain about a free energy of a system to understand these dynamics. This energy is known as Landau–Ginzburg free energy ($\mathcal{F}$) for description of a stability of phase in a two-phase mixture system, denoted as below.[118-120]

$$\mathcal{F} = -\frac{1}{2}\varepsilon m^2 + \frac{1}{4}\gamma m^4 + \frac{1}{2}\sigma(\nabla m)^2 \qquad (13)$$

where $m = c - (c_l+c_h)/2$ is the normalized concentration of precipitation precursor (c), and c_l and c_h are concentrations at the steady state of $\mathcal{F}$ at $-m_e$ and $+m_e$ (Figure 1.18a). The parameters ε, γ, and σ are specific values for a system. Eq. 13 represents that a thermodynamics stability of a system is decided the precursor concentration. Actually, Figure 1.18a shows this relationship, where we can see how the initial system ($\mathcal{F}_0$) can be phase-separated from c_0 to c_l and c_h (cl is zero in Liesegang system because most Liesegang systems are single-phase systems). When system remains out of $-m_e$ ($m < -m_e$), the system is stable to any perturbation and no phase transition occurs because the $\mathcal{F}$ of the system after a perturbation is always higher than $\mathcal{F}_0$. On the other hand, the system shows different behavior when $-m_e < m < -m_s$. Although the system does not undergo a phase transition spontaneously, an external perturbation allows the system to cross the energy barrier at $m = 0$ and the phase transition occurs. Such a state that requires perturbation assistance is called a metastable state, and the phase transition that occurs in this case is a scenario requiring nucleation. Furthermore, the phase transition proceeds spontaneously without any perturbations when $-m_s < m$, in which this state is so-called unstable and phase separation based on spinodal decomposition is driving force. Thus, a dominant scenario for precipitation is bifurcated to whether nucleation or phase separation depending on the state of the system. Figure 1.18b shows a phase diagram about this bifurcation. The binodal and spinodal lines indicates the concentration thresholds to decides the state of system whether the metastable or the unstable regions. By matching the above branching theory with the typical reaction process of the Liesegang system shown in eqs. (11) and (12), LP formation scenarios can be described as shown in Figure 1.18c. The key parameter to determine the thermodynamic stability in the phase diagram is the precipitation precursor concentration, namely, water soluble or dispersible molecules or particles, which is corresponding to C in eqs. (11) and (12). In the nucleation-based scenario, C translates to nuclei (N) by nucleation, which is corresponding to the solid-phase transition process.[121] Afterwards, N becomes P thorough nuclei/particle growth and aggregation. On the other hand, C directly translates to P without undergoing nucleation in the phase separation-based scenario, which is a spontaneous process that does not require perturbation unlike nucleation.

1.7.2 Nucleation-based scenario (pre-nucleation model)

To discuss the LP formation based on the nucleation-based scenario, it is needed to know the principal of nucleation. The classical nucleation theory is the well-known theory to explain this process.[121] In this theory Gibbs's free energy (ΔG) for nucleation as a function of particle radius (r) is denoted as below.

$$\Delta G = 4\pi r^2\sigma + \frac{4}{3}\pi r^3 \Delta G_v \qquad (14)$$

The first term represents surface energy contribution, where σ is surface energy [J/m^2]. Also, the second term indicates contribution of chemical potential, where ΔG_v is chemical potential difference ($\Delta\mu$) between the liquid and solid phases per unit particle volume.

$$\Delta G_v = \frac{-N\Delta\mu}{v} \qquad (15)$$

$$\Delta\mu = \mu_L - \mu_S \qquad (16)$$

where N, v, μ_L, and μ_S are Avogadro constant [mol^{-1}], molar volume of particles [m^3/mol], chemical potentials of solutes in solution, and in a particle [J/molecule]. Also, $\Delta\mu$ is related to supersaturation ratio (X/X_s) shown below:

$$\Delta\mu = k_B T \ln\left(\frac{X}{X_s}\right) \qquad (17)$$

where X and X_s are concentration in solution and saturation solubility of chemical species X. In the case of a supersaturation condition ($X/X_S > 1$), $\Delta\mu$ becomes positive, namely ΔG_v shows negative values. While, ΔG_v shows positive value because $\Delta\mu$ becomes negative under below supersaturation ($X/X_S < 1$). Furthermore, surface energy contribution that is the first term in eq. (14) is always positive value. Therefore, changes in ΔG for nucleation that is denoted by eq. (14) represent a curve with a maximum value corresponding to an energy barrier (E_n) (Figure 1.19).

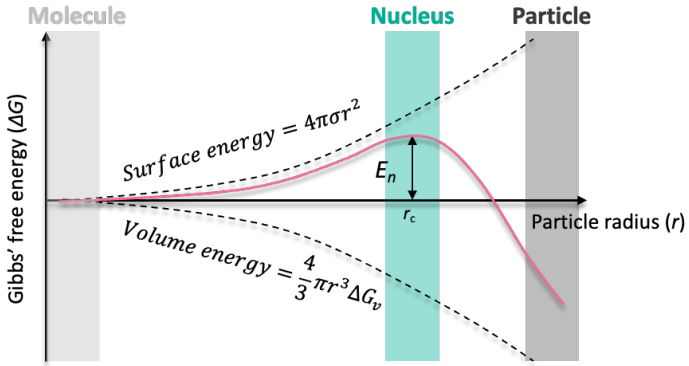

Figure 1.19. Relationship between Gibbs's free energy (ΔG) and particle radius (r) on the nucleation process, deduced by the classical nucleation theory. The changes in ΔG are calculated by a sum of the surface energy term and the volume energy term. E_c and r_c represent the energy barrier of nucleation and critical radius for it.

Although molecules uninucleate below the supersaturation because a system does not overcome E_n, molecules translate into nuclei when a concentration in a system reaches the supersaturation, in which this step corresponds to a solid-phase transition and the nucleus is defined as the initial formed solid with critical radius (r_c) at the maximum value of ΔG. Subsequently, formed nuclei growth spontaneously because ΔG decreases with the increase in r. The values of r_c and E_n is calculated following below.

$$r_c = \frac{2\sigma v}{RT \ln\left(\frac{X}{X_S}\right)} \tag{18}$$

$$E_n = \frac{16\pi\sigma^3 v^2}{3RT\ln^2\left(\frac{X}{X_S}\right)} \tag{19}$$

In summary, the reaction processes involved in LP formation of typical salt formation reaction in the nucleation-based scenario can be expressed as follows:

(i) Salt formation reaction: $A + B \rightarrow C$ when $[A][B] > K_1$ (20)

(ii) Nucleation: $C \rightarrow N$ when $[C] > K_2$ (21)

(iii) Particle growth and aggregation: $C \rightarrow P$ (22)

where C and N are molecules and nuclei; K_1 and K_2 are a solubility product and a nucleation threshold equaling X_s. The LP formation mechanism expressed by eqs. (20)-(22) is commonly called the Nucleation and Growth (NG) model.[62, 114-115] There is also a model called the sol-coagulation model,[62, 87, 122] which considers diffusive solid sol particles between C (diffusive) and P (non-diffusive). However, this model is not included in the nucleation-based and phase-separation-based scenarios in this paper because it may show complex mechanisms that span the phase-separation-based scenarios described below. The proposed pattern formation mechanism based on the NG model is depicted in Figure 1.20.

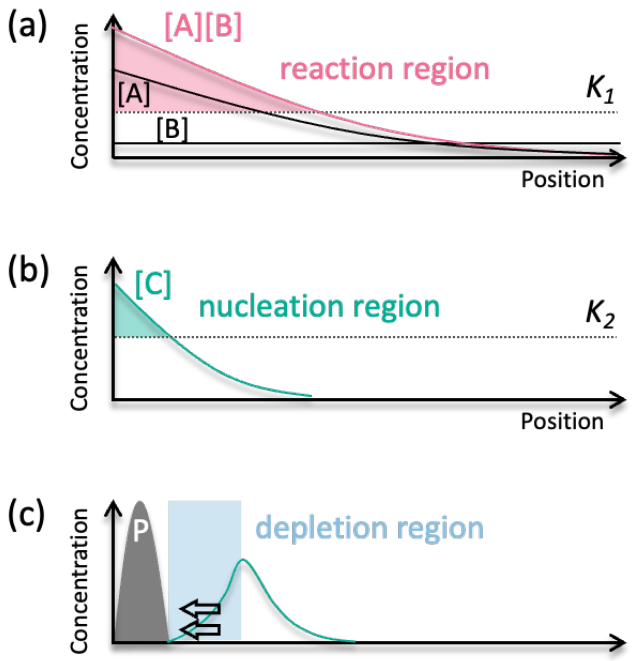

Figure 1.20. Proposed formation mechanism of LP based on the NG model. (a) Firstly, diffusion of A and homogeneously pre-doped B form a gradient (pink curve of the concentration product ([A][B]). The salt formation reaction in eq. (20) proceeds at a position where [A][B] > K_1, and (b) a concentration gradient of C is formed (green curve). (c) Subsequently, nucleation in eq. (21) occurs at a position when [C] > K_2, and precipitates region is formed through following growth and aggregation processes in eq. (22). At the same time, this process consumes the surrounding C, thus forming a depletion region (blue region). The above processes (a)-(c) are repeated to form a periodic precipitation pattern.

When a reservoir of A and a gel pre-doped with B come into contact, A diffuses into the gel and forms a concentration gradient of A (black curve in Figure 1.12a). Therefore, a gradient of concentration product between A and B ([A][B]) is formed (pink line). At a region where [A][B] exceeds K_1, a salt formation reaction is triggered to generates C (eq. (20)), and a concentration gradient is formed according to this reaction (green curve in Figure 1.20b). Subsequently, C transforms into N by nucleation at a region where [C] > K_2 (eq. (21)) (green region in Figure 1.20b). Since the formed N becomes P through particle growth and aggregation processes (eq. (22)), the concentration of C decreases significantly in this region, and C flows in from the surrounding region forming a "reverse" concentration gradient toward the P-forming region. This phenomenon leads to further growth/aggregation processes in the P-forming region and depletes the surrounding C. Thus, there is a region where [C] > K_2 is not satisfied, namely nucleation is not progressive in the neighborhood of the P region, and this region corresponds to the depletion zone of LP. Therefore, the dynamics of nucleation in space determines an

alternating precipitation/depletion periodicity of LP. (x_{n+1}/x_n). For this reason, the nucleation-based scenario is so-called a "pre-nucleation" model. The RD equation of this scenario for numerical simulation can typically be given as[60, 68, 82, 87]

$$\frac{\partial a}{\partial t} = D_a \frac{\partial^2 a}{\partial x^2} - k_1 ab\theta(ab - K_1) \quad (23)$$

$$\frac{\partial b}{\partial t} = D_b \frac{\partial^2 b}{\partial x^2} - k_1 ab\theta(ab - K_1) \quad (24)$$

$$\frac{\partial c}{\partial t} = D_c \frac{\partial^2 c}{\partial x^2} + k_1 ab\theta(ab - K_1) - k_2 c\theta(c - K_2) \quad (25)$$

$$\frac{\partial p}{\partial t} = k_2 c\theta(c - K_2) \quad (26)$$

where a, b, c, and p are concentrations of A, B, C, and P; D_a, D_b, and D_c are diffusion coefficients of A, B, and C; k_1 and k_2 are rate constants of salt formation reaction and nucleation. The function of θ represents the Heaviside step function, that is, $\theta(X - K) = 1$ when [X] $\geqq$ any threshold (K), whereas $\theta(X - K) = 0$ when [X] < K. Most of reaction systems in Liesegang experiments introduced in Sec. 1.6.2 includes the nucleation step. Therefore, understanding the nucleation-based scenario is basic and essential for revealing the underlying mechanism of the Liesegang phenomenon. Actually, mathematical modeling interpretations based on this scenario have helped us to understand the effects of many experimental conditions.[59-60, 71, 87] Despite the versatility of this nucleation-based scenario, the transition of LP geometries in reaction systems based on this scenario remains unexplored (Sec. 1.6.3). Furthermore, although this scenario is consistent and can describe a very wide range of phenomena in various reaction systems and experimental set-ups, MP law that is one of the tools used to evaluate its periodicity (eq. (8)) is only focused on the perspective of the relationship between concentration changes of A and B, namely the classical MP law alone may not be able to correctly interpret the various results in this scenario. Therefore, to understand the pre-nucleation model, it is important to discuss the extensibility of the MP law based on more general parameters that can take into account the effects of various experimental conditions and to elucidate the mechanism of the pattern transition phenomenon from the viewpoint of nucleation.

1.7.3 Phase separation-based scenario (post-nucleation model)

On the other hand, we should consider another thermodynamic process to understand the phase separation-based scenario as describing in Sec. 1.7.1. The typical reaction processes in this scenario are shown as

(i) Salt formation reaction: A + B → C when [A][B] > *K*' (27)

(ii) Phase separation: C → P (28)

where A and B are outer and inner electrolytes; C is a diffusive inter mediate such as sol particles; *K*' is a threshold that is sufficient to trigger salt formation reactions and nucleation. Most of studies for this scenario insisted that C was produced by the salt formation reaction and phase separation of diffusive solid colloid particles as C formed discrete precipitation patterns.[123-125] Therefore, this scenario is called the "post-nucleation" model because the process that determines the periodicity of the pattern is a process that occurs after nucleation. In order to distinguish whether the system is unstable enough to go through such the phase separation-based scenario, Derjaguin–Landau–Verwey–Overbeek (DLVO) theory is used,[126] which is one of the theories to describe an aggregation dynamics of colloid particles in solution. This theory is expressed by a total potential energy between two particles (W_{tot}) calculated by a sum of two potential energy terms: van der Waals attraction (W_{vdw}) and electrostatic repulsion derived from the surface potential of particles (W_e) as shown in following equations.[127]

$$W_{tot} = W_{vdw} + W_e \tag{29}$$

$$W_{vdw} = -\frac{Ar}{12(r+d)} \tag{30}$$

$$W_e = 4\pi\varepsilon r^2 Y^2 \left(\frac{kT}{e}\right)^2 \frac{exp(-\kappa d)}{d+2R} \tag{31}$$

$$\mathrm{Y} = \frac{8tanh\left(\frac{e\psi_0}{4k_BT}\right)}{1+\left[1-\frac{2\kappa r+1}{(\kappa r+1)^2}tanh^2\frac{e\psi_0}{4k_BT}\right]} \tag{32}$$

$$\frac{1}{\kappa} = \frac{q}{[electrolytes]} \tag{33}$$

where A, r, and d are the Hamaker constant, particle radius, and interparticle distance between two particles; ε, $1/\kappa$, and ψ_0 are the dielectric constant, Debye length (in nm unit), and surface potential of a particle; q is a coefficient that depends on the type of electrolyte: 0.304 (charge of cation: anion = 1:1, e.g. NaCl), 0.176 (2:1 or 1:2, e.g. $CaCl_2$ and Na_2SO_4),

and 0.152 (2:2, e.g. $MgSO_4$). Based on these equations, an example of W_{tot} can be illustrated as a function of r (Figure 1.21).

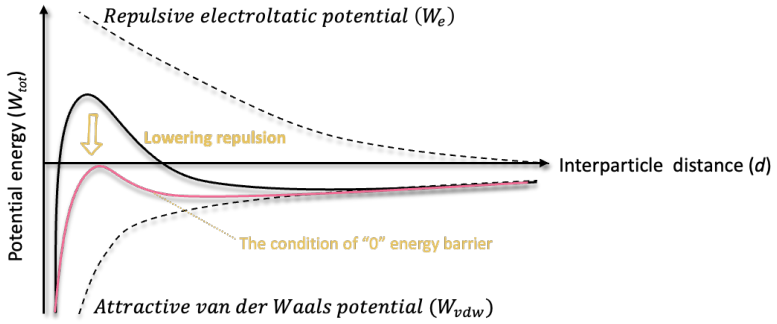

Figure 1.21. Interparticle interaction as a function of interparticle distance between two particles. Electrostatic and van der Waals interactions provide repulsive and attractive interactions, respectively, between particles of the same composition. The sum of the electrostatic and van der Waals interactions that control the aggregation behavior is shown by the pink curve.

From this figure, aggregation of the particles is inhibited due to the potential energy barrier when the repulsion between the particles is sufficiently effective (black curve). However, if the electrostatic repulsion decreases for some reason (e.g., decreasing in Debye lengthening due to increased electrolyte concentration or loss of surface charge), the barrier disappears and the system allows phase separation via spontaneous aggregation if particles (pink curve). Namely, this process can be regarded as the precipitation process that arises from an unstable state in Figure 1.18b that does not require a perturbation, unlike nucleation. Figure 1.22 shows a proposed mechanism of LP formation based on the phase separation-based scenario.

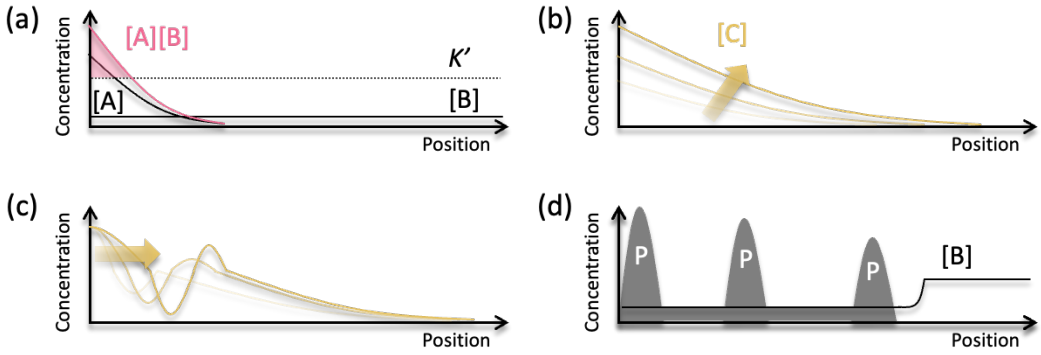

Figure 1.22. Proposed formation mechanism of LP based on the phase separation-based scenario. (a) Firstly, diffusion of A and homogeneously pre-doped B form a gradient (pink curve of the concentration product ([A][B]). (b) Subsequently, a concentration gradient of C is formed and evolved as proceeding salt formation reaction in eq. (27) (yellow curve). (c) Spontaneous phase separation occurs when the DLVO potential of the system allows for aggregation. (d) Finally, discrete precipitation patterns arising from repeating steps (a)-(c).

The starting point of the pattern formation is the formation of a gradient in the concentration product due to the diffusion of A, as in the nucleation-based scenario (Figure 1.22a). Subsequently, C is produced by the salt formation reaction and nucleation following eq. (27), and the formed gradient of C evolves as proceeding the reaction (Figure 1.22b). When DLVO potential reaches a critical value meaning the energy barrier is 0, phase separation via spontaneous aggregation is trigged (Figure 1.22c). Finally, LP is formed by repeating these processes (Figure 1.22d). In a typical LP formation set-up, the concentration of the outer electrolyte is excessive and may have the effect of decreasing the Debye length. However, it was reported that this Debye length can be controlled by further adding other electrolytes, thereby modulating the LP periodicity.[59, 128] Therefore, it is unclear whether the system had reached a thermodynamically unstable state that induces spontaneously precipitation, and the involvement of phase separation in the LP formation mechanism is unclear, in previous studies based on the above assuming the phase separation-based scenario with salt formation reactions. More troubling, all of these studies involve mixed nucleation to form colloidal particles, making it difficult to distinguish the discussion from a completely nucleation-based scenario in LP formation systems involving such salt formation reactions. Therefore, understanding LP formation based on the phase separation-based scenario progresses much more slowly than discussions based on the nucleation-based scenario, and this scenario validity is unclear. However, it is noted that many numerical simulation studies were carried out so far (Figure 1.23).[116-117, 129] These studies based on coupling RD equation with Cahn-Hilliard equation[118-119] that can explain pattern formation through phase separation.

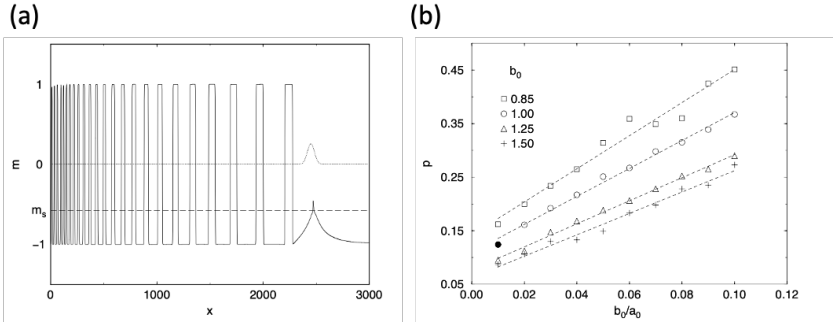

Figure 1.23. Simulation results based on the phase separation scenario. (a) evolution of pattern formation and (b) relationship between spacing coefficient (*p*) and electrolytes concentrations, which were reprinted with permission from Ref. 116. Copyright 1999 American Physical Society.

However, since there is no experimental system that can faithfully verify these results, we have not been able to jointly utilize experiments and mathematical models, which is an important research routine in RD model research (Figure 1.1).

1.8 Purpose in this study

Formation of dissipative structures is one of the characteristic phenomena for nonequilibrium self-organization. In particular, self-organization with RD processes provides various spatiotemporal pattens with complex and/or regular periodicities. In order to understand such complex phenomena, it is essential to conduct multifaceted investigations using a combination of experimental and mathematical modeling. The BZ reaction and TPs, which are models of RD dissipative structures, have acquired practicality as models because their mechanisms and controllability have been clarified through numerous studies in the past. However, a comprehensive understanding of the mechanism of Liesegang phenomenon, which is a candidate model for RD pattern formation with precipitation due to solid-phase transition, has not been achieved even though more than 100 years have passed since its first discovery. Thus, Liesegang phenomenon has not established a robust position as a practical model different from other models such as BZ reaction and TP. In order to understand the mechanism, we should focus on two precipitation scenarios that is bifurcated depending on the thermodynamic state of the system, as described in Sec. 1.7: one is the nucleation-based scenario (pre-nucleation model), and another is the phase separation-based scenario (post-nucleation model). As explained in section 1.6 onwards, the former has been justified in its scenario in LPs formation by many previous studies. As explained in 1.6 onwards, the former has been justified in its scenario in LPs formation by numerous previous studies. On the other hand, metrics to evaluate the patterns formed based on this scenario, especially the MP law, remain a classical formulation. The MP law specializes in evaluating the periodicity of changes in the concentration of electrolytes used for LPs formation. However, what essentially determines the LP periodicity should be the diffusion flux (F_{diff}) associated with a diffusion of outer electrolytes and a reaction flux associated with the subsequent deposition formation. As mentioned in Sec. 1.2 and 1.6, the flux is closely related to the dissipative structure. Indeed, although the change in electrolyte concentration is one factor that can change the $F_{diff,}$ other effects (such as the volume effect of the reservoir) cannot be taken into account. Therefore, it is needed a discussion that directly correlates F_{diff} with LP periodicity in order to further understand the nucleation-based scenario. Then, chapter 2 will directly demonstrate the relationship between LP periodicity and F_{diff}, and combine the results with the MP law, which will be modified into a tool to evaluate the essential factors determining periodicity. Furthermore, in Chapter 3, we will discuss the factor of the transition of the LP geometries described in Sec. 1.6.3 from the kinetic point of view of nucleation that is the dominant process in this scenario. This transition phenomenon has been discussed from the viewpoint of ion

adsorption on the particles, but the effect of nucleation has not been discussed, even though all the reaction systems in which the transition phenomenon was observed include the process of nucleation. Therefore, we demonstrate the utility of the nucleation-based scenario by investigating the involvement of nucleation in this phenomenon. In contrast to the nucleation-based scenario, the phase separation-based scenario, which is another bifurcated scenario in the Liesegang phenomenon, is little understood, described in Sec. 1.7.3. This is because the mathematical model for this scenario has been studied extensively but there is no experimental system that faithfully reproduces this scenario. Therefore, the construction of an experimental system based on this scenario provides an opportunity not only to clarify how phase separation that is the dominant process in this scenario is involved in the LP formation mechanism, but also to validate this scenario. It has been pointed out that this scenario may be closely related to exceptional class of LPs such as the helix pattern introduced in Sec. 1.6.3 and the geoscientific pattern described in Sec. 1.6.4.[86, 130-131] Therefore, understanding this scenario is essential to improve the status of the Liesegang phenomenon as a model. However, as mentioned in Sec. 1.7.3, all experimental demonstrations of this scenario so far have been discussed only in reaction systems where the above nucleation-based scenario may coexist. Therefore, in Chapter 4, we focus on this reaction system that induces precipitation formation without nucleation, and we aim to construct a new experimental system that can demonstrate the phase-separation-based scenario by using this focused system. And finally, in Chapter 5, we summarize the reach of each thermodynamic bifurcated scenario in the Liesegang phenomenon, based on the findings of Chapters 2-4 as conclusions. Furthermore, future issues will be mentioned in this chapter.

Chapter 2 Modification of Matalon-Packter Law

Based on a Diffusion Flux

2.1 Introduction

The periodicity of LPs depends on concentrations of outer and inner electrolytes (Figure 2.1).[62, 64, 83]

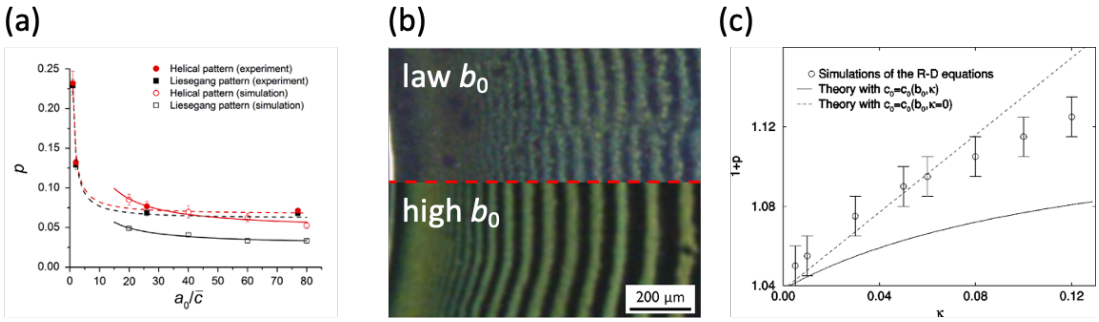

Figure 2.1. (a) The value of p is changed with an initial concentration of outer electrolytes (a_0). This figure was reprinted with permission from Ref. 64. Copyright 2013 Elsevier. (b) Difference of interband spacing (Δx_n) when an initial concentration of inner electrolytes (b_0) was changed. This picture was reprinted with permission from Ref. 83. Copyright 2016 American Chemical Society. (c) Simulation results of changes in p with κ (= b_0/a_0) based on the NG model. This data was reprinted with permission from Ref. 62. Copyright 1998 American Physical Society.

Figure 2.1a,b shows a clear dependence of spacing coefficient (p) on an initial concentration of outer electrolytes (a_0) and inner electrolytes (b_0). The initial concentration means the value before pattern formation (t = 0). Experimentally, we can see p decreases with the increase in a_0 (Figure 2.1a), and decreases with the increase in b_0 (Figure 2.1b). This trend was roughly consistent with the prediction of the MP law expressed in eq. (8). However, it is noted that since b_0 is a variable of the decreasing function included in the MP law, its dependence may vary from system to system. Simulations based on the nucleation-based scenarios also clearly showed that p depends on the initial concentration of each electrolyte (Figure 2.1c). Therefore, MP law is a useful tool for evaluating and predicting periodicity changes of obtained LPs experimentally in the different electrolyte concentration. As discussed in Sec. 1.7.2, the determinant of the periodicity in the nucleation-based scenario is nucleation triggered by the evolution of the diffusion gradient of the outer electrolyte. In other words, LP formation is sensitive to changes in diffusion flux (F_{diff}) of the outer electrolyte. Therefore, the classical MP law (eq. (8)) is specialized to reflect the modulation of F_{diff} due to electrolyte concentration

changes, especially changes in a_0. This is useful for evaluating a typical system such as the one shown in Figure 1.14. However, it was recently reported that the periodicity can be changed even under similar electrolyte concentration conditions by using the change in F_{diff} caused by imposing an electric field[101, 103] or gel mechanical changes of gel[132] during the pattern formation. In such cases, the classical MP law that considers only electrolyte concentration changes was not applicable. Therefore, this classical law needed to be modified as necessary to essentially evaluate the effect of F_{diff} in the nucleation-based scenario.

It is known that F_{diff} also depends on the volume of the outer electrolytes-containing solution reservoir in addition to a_0.[133] In other words, F_{diff} will change for different reservoir volumes even if a_0 is the same. However, it has been few experimental studies, demonstrating the dependence of F_{diff} on p at different reservoir volumes. This volume effect is determined by the equilibrium concentration of outer electrolytes in the reservoir (a_{res}) after the reservoir and gel is contact with each other (Figure 2.2).

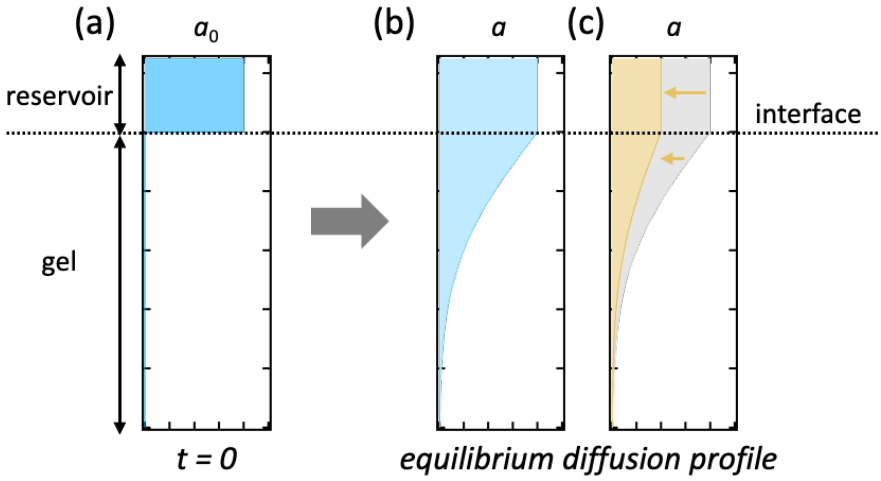

Figure 2.2. (a) Initial diffusion concentration profile of outer electrolytes at $t = 0$. Equilibrium diffusion profile when (b) $a_{res} = a_0$ and (c) $a_{res} < a_0$. Even though a_0 is the same, F_{diff} is smaller in (c) than in (b).

This value is calculated by using the reservoir volume (V_{res}) and the gel volume (V_{gel}) as below.

$$a_{res} = a_0 \frac{V_{res}}{V_{res}+V_{gel}} \tag{34}$$

If $V_{res} \gg V_{gel}$, a_{res} can be approximated to a_0 and the change in reservoir concentration due to diffusion into the gel can be ignored. Namely, the diffusion gradient of the outer electrolytes evolves while the reservoir concentration remains constant (Figure 2.2b). However, if the above assumptions are not satisfied, since the previous approximation is

no longer valid, a_{res} becomes smaller than a_0 ($a_{res} < a_0$). Therefore, the diffusion gradient changes with this decreasing a_{res} (Figure 2.2c). Depending on these two conditions, there are two solutions to the one-dimensional Fick's diffusion law. [133] When the condition other than $V_{res} \gg V_{gel}$, namely the amount of outer electrolyte in the reservoir is finite, the solution is:

$$a(x,t) = \frac{la_0}{2\sqrt{\pi Dt}} \exp\left(\frac{-x^2}{4Dt}\right) \quad (35)$$

where l, D, x, and t are the height of reservoir, the diffusion coefficient, distance from the reservoir, and time, respectively. On the other hand, when the condition of $V_{res} \gg V_{gel}$, namely, the amount of outer electrolyte in the reservoir is almost infinite, the solution is:

$$a(x,t) = a_0\left(1 - erf\frac{x}{2\sqrt{Dt}}\right) \quad (36)$$

where the function of *erf* represents the error function. Actually, simulations based on eqs. (35) and (36) with a_0 set to the same value reported that the diffusion gradient extends farther in the infinite reservoir, namely, the F_{diff} at the same position and time increases, as shown in Fig. 2.2b,c. Therefore, a detailed investigation of the effect of the volume effect on the periodicity of LP leads to a direct verification of the effect of F_{diff} on the MP law. Furthermore, such differences in F_{diff} due to volume effects are consideration when comparing LP periodicity in various studies, and may simplify the consideration of other experimental complicated effects on F_{diff} in the nucleation-based scenario. However, there has been no experimental study to examine the volume effect so far. Therefore, the purpose of this chapter is to demonstrate the relationship between a_0 and p under the above two volume conditions by both experiment and simulation, and to clarify the relationship between F_{diff} and p based on the results.

2.2 Experiments

2.2.1 Reagents and instruments

Agarose (fine powder) as a gel medium (Figure 2.3), copper (II) chloride dihydrate ($CuCl_2$•$2H_2O$) as the outer electrolyte, and potassium chromate (K_2CrO_4) as the inner electrolyte were purchased from FUJIFILM Wako Pure Chemical Industry (Japan). All reagents were used without further purification. The formed patterns were observed using a stereomicroscope system (Olympus SZ-61). Image analysis was performed using ImageJ software.

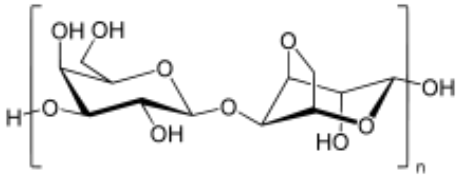

Figure 2.3. Structure of agarose.

2.2.2 Sample preparation and pattern formation

The agarose powder was added to ultra-purified water to be the concentration at 1.0 w/w% and heated in a microwave oven to dissolve roughly it. Then, it was immediately heated at 90°C for 10 min with stirring at 150 rpm to dissolve it completely. A concentrated aqueous solution of K_2CrO_4 (typically 1.0×10^{-1} M) was added to this agarose solution to reach a final concentration of 1.0×10^{-2} M. This hot agarose sol was poured into a glass test tube (∅ =1.0 cm) to a gel height (h) of 12 cm and left at 18°C for 6 hours to complete gelation. Subsequently, the test tube was placed upside down in a reservoir solution containing $CuCl_2$ (0.50-2.0 M), and the top of the gel was completely immersed (Figure 2.4).

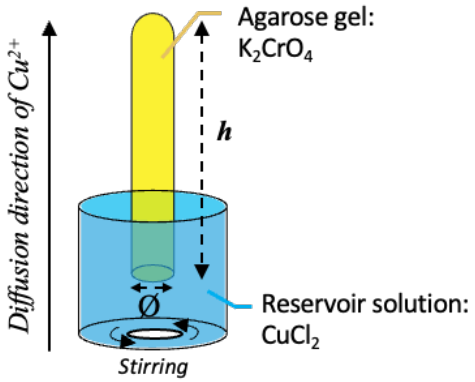

Figure 2.4. Experimental setup to explore the volume effect (h: gel height, ∅: inner diameter of test tube).

As soon as this was done, Cu^{2+} started invading into the gel by the diffusion and reacted with CrO_4^{2-} as below.

$$Cu^{2+} + CrO_4^{2-} \rightarrow CuCrO_4 \qquad (37)$$

According to this reaction, precipitates of $CuCrO_4$ was generated. This precipitation region expanded upward from the interface as the diffusion of Cu^{2+} proceeded. To keep the Cu^{2+} concentration in the reservoir uniform, the solution was stirred during the patterning experiments (Figure 2.4). In all cases, the reaction system was kept in an incubator at 18°C, and the patterning period was fixed at one week.

2.2.3 Observation and analysis of obtained patterns

After the reaction, the test tubes were withdrawn from the $CuCl_2$ solution and the light transmitted through each sample was observed using a stereomicroscope equipped with a CCD camera. In the image analysis, the gray value change along the diffusion direction of Cu^{2+} from the interface was determined using the line profile tool. In the image analysis, the line profile tool was used to determine the change in gray value along the diffusion direction of Cu^{2+} from the interface, and the position of the peak of the gray value was defined as x_n (Figure 2.5).

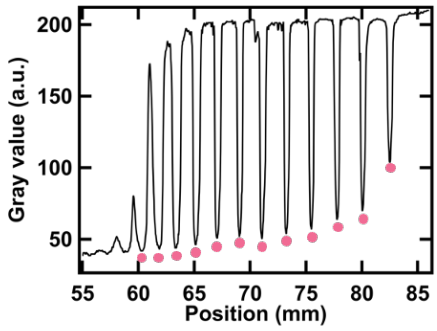

Figure 2.5. Typical example of obtained line profile. The pink circle corresponds to the band position (x_n).

2.2.4 Determination of the reservoir volume

The volume of the Cu^{2+} reservoir for each of the finite and infinite conditions was determined based on eq. (34). According to the Sec 2.2.2, V_{gel} was calculated as 9.5 mL from h and ∅, and was fixed at this value in all experiments. As a small reservoir that corresponds the finite condition, I adopted V_{res} = 5.0 mL. When this condition, the equilibrium concentration of Cu^{2+} in the reservoir ($[Cu^{2+}]_{res}$) was calculated as

$0.34\times[Cu^{2+}]_{0,}$ meaning that Cu^{2+} concentration in the reservoir decreases by about 65% at equilibrium. This situation represented the same condition shown as Figure 2.2c. On the other hand, for V_{res} = 50 mL, $[Cu^{2+}]_{res} = 0.84\times[Cu^{2+}]_0$, indicating that the Cu^{2+} concentration in the reservoir decreased by only about 15% at equilibrium. Therefore, compared to the 5 mL small reservoir, the 50 mL larger reservoir maintained a higher concentration after pattern formation, which corresponded the situation shown as Figure 2.2b.

2.3 Results and discussion

2.3.1 Pattern formation with a small reservoir

Figure 2.6 shows results of formed patterns with the small reservoir and analysis based on spacing law (eq. (6)) when $[Cu^{2+}]_0$ was changed from 0.5 to 2.0 M. From near the top green edge (the interface between the CuCl2 solution and the gel) of the gel in obtained images (Figure 2.6a-d), a dense precipitation region of $CuCrO_4$ was formed and expanded with the diffusion of Cu^{2+} until half the length of the gel, followed by a discrete precipitation band below it. This was because the F_{diff} near the interface was too high, and the fine balance required for LP formation by the RD process was further satisfied in the gel only when the F_{diff} was sufficiently reduced. As evidence of this effect, this dense region expanded and the discrete band formation position was farther from the interface with the increase in $[Cu^{2+}]_0$ (Figure 2.6a to d) because F_{diff} increased as $[Cu^{2+}]_0$. At the same time, as $[Cu^{2+}]_0$ increased, the green translucent region without precipitates expanded from the edge of the gel. Although the expansion of the dense region was within our expectation, the expansion of the green colored translucent region with the increase of $[Cu^{2+}]_0$ was unexpected. Previous studies have shown that as ionic strength increases, the structure of the agarose gel is disrupted by local aggregation of agarose chains.[134] In LPs formation, it is important that the precipitates are immobilized by the gel network.[20] Therefore, this disturbance of the gel structure might have interfered with this effect. However, it was necessary to analyze a time-course change using time-lapse observation and other methods in order to clarify this effect. In any case, this region did not preclude the analysis of periodicity based on the spacing law (eq. (6)) with multiple bands because the dense and translucent regions were not included in spacing law. Then, we carried out the spacing analysis for Figure 2.6a-d. Figure 2.6e shows the relationship between the x_{n+1}/x_n ratio and the number of bands (n). For $[Cu^{2+}]_0$ = 0.5 M (Figure 2.6e●), x_{n+1}/x_n increases as n increases from 1 to 4, eventually reaching a constant value as n increases. The reason for this initial increase could be understand that the RD process had not reached a steady state due to excess F_{diff} in the early stages of band formation. This initial increase and subsequent saturation of x_{n+1}/x_n was also observed for other values of $[Cu^{2+}]_0$ (Figure 2.6e▲-▼). However, the saturation value of x_{n+1}/x_n decreased with increasing $[Cu^{2+}]_0$ (corresponding to a_0 in eq. (8).), which is consistent with the prediction from the classical MP law.

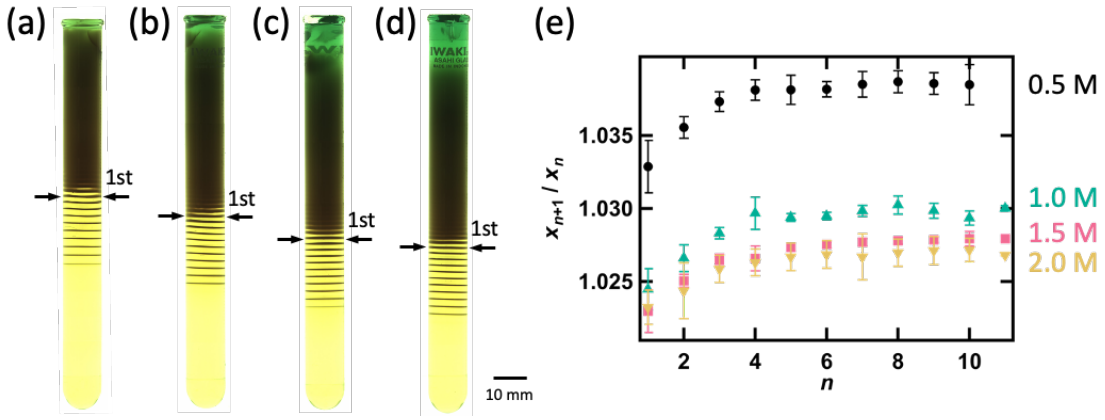

Figure 2.6. Images of obtained patterns with the small reservoir (V_{res} = 5.0 mL) at $[Cu^{2+}]_0$ = (a) 0.5 M, (b) 1.0 M, (c) 1.5 M, and (d) 2.0 M. The pair of arrows indicates the 1st precipitate band (defined as n = 1) in the analysis based on spacing law. (e) Plot of spacing law (eq. (6)): changes in x_{n+1}/x_n with n ($[Cu^{2+}]_0$ = ●: 0.50 M, ▲: 1.0 M, ■: 1.5 M, and ▼: 2.0 M).

2.3.2 Pattern formation with a large reservoir

Since such experiments using a few mL of reagent are realistic and easy to set up, similar LP experiments using small reservoirs have been demonstrated in the past.[69, 108, 123] Indeed, the previous one with the $CuCrO_4$ precipitates system used V_{res}:V_{gel} = 1: 3.5,[123] and $[Cu^{2+}]_{res}$ was calculated as 0.22× $[Cu^{2+}]_0$ in this condition. This condition corresponded to a truly finite condition; however, a distinct LP was formed. Thus, it was difficult to see the volume effect from the clarity of the resulting pattern. Therefore, similar experiments with the larger reservoirs were needed to explore the difference in the effects of the smaller and larger reservoirs. However, to the best of our knowledge, few experiments have been reported using a large reservoir with a volume is sufficiently larger ($V_{res} \gg V_{gel}$) than the typical experiment described above ($V_{res} < V_{gel}$). Therefore, we then carried out the same experiments with the large reservoir (V_{res} = 50 mL ≫ V_{gel} = 9.5 mL) (Figure 2.7). Figure 2.7a-d shows obtained patterns in this condition with the same $[Cu^{2+}]_0$ values as the conditions for the small reservoir. These patterns were generally similar to the patterns obtained in the case of the small reservoir (Figure 2.6a-d). However, both the front of the periodic banding and the dense region appear to be more advanced than the small condition, which is probably due to the relatively large F_{diff}. As a possible reason for the expansion of the dense region, the aggregation dynamics of $CuCrO_4$ colloidal particles is a key process, which is promoted by the increase in ionic strength due to high F_{diff} of Cu^{2+}. From DLVO theory (Sec. 1.7.3), the energy barrier determining the aggregation dynamics depends on a surrounding ion concentration (ionic strength) because Debye length included in the term of electric repulsion is modulated by

it.[127] Previous studies have investigated the effect of ionic strength on the geometrical changes in LPs and have shown that the width of the band increases with increasing ionic strength[128] and that the effect of ionic strength was related to the kinetics of particle growth and aggregation in the RD process based on the RD simulation.[59] Therefore, the large reservoir has a higher F_{diff}, which promote the aggregation of colloidal particles, namely reduce the resolution of the bands. This is presumed to cause the bands to coalesce into regions of densification at positions where would have been discrete in the small reservoir. Furthermore, the relationship between x_{n+1}/x_n and n in the large reservoir is shown in Figure 2.7e. As in the small reservoir, x_{n+1}/x_n approaches constant around $n = 4$ for all $[Cu^{2+}]_0$, and this constant value also decreases with increasing $[Cu^{2+}]_0$. Thus, the MP law can be applied to both small and large reservoirs, and the classical MP law found to be useful when the reservoir volumes are same.

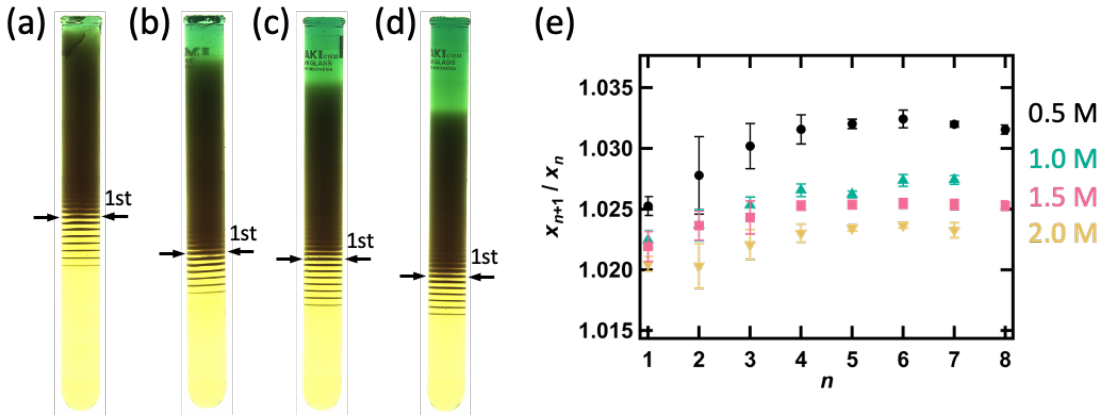

Figure 2.7. Images of obtained patterns with the large reservoir (V_{res} = 50 mL) at $[Cu^{2+}]_0$ = (a) 0.5 M, (b) 1.0 M, (c) 1.5 M, and (d) 2.0 M. The pair of arrows indicates the 1st precipitate band (defined as $n = 1$) in the analysis based on spacing law. (e) Plot of changes in x_{n+1}/x_n with n ($[Cu^{2+}]_0$ = ●: 0.50 M, ▲: 1.0 M, ■: 1.5 M, and ▼: 2.0 M).

2.3.3 Comparison of 1+*p* between small and large reservoirs

Figure 2.8 shows the average saturation of x_{n+1}/x_n (namely $1+p$) in Figures 2.6e and 2.7e as a function of $[Cu^{2+}]_0$ in the large and small reservoirs. For a small reservoir (Figure 2.8●), $1+p$ gradually decreases, and changes with conditions of $[Cu^{2+}]_0$ are in good agreement with the approximate fitting curve drawn based on the classical MP law in eq. (8) (dashed line). Similar behavior was observed even with the large reservoir (Figure 2.8▲). However, the value of $1+p$ is lower than the value under the small volume condition at the same $[Cu^{2+}]_0$ (e.g. for $[Cu^{2+}]_0$ = 1.0 M, $1+p$ = 1.030 with the small reservoir, while 1.026 with the large reservoir). Based on eq. (8), this result was difficult to interpret, because the classical MP law describes only the dependence of p on the

electrolyte concentration, and under such same $[Cu^{2+}]_0$ conditions p should be equal. This difference could have been caused by a change in the functions of $F(b_0)$ and $G(b_0)$ in the classical MP law. However, the past study denoted that these functions depended only reagent type and b_0.[62] Therefore, the influence of these functions can be ignored. Thus, such lowering the p value by in the case of using the large reservoir cannot be explained by the classical MP law. Namely, when b_0 is fixed, it is suggested that the limit of describing the effect of F_{diff} caused by other than changes in a_0. However, previous studies of chemical LP formation did not take into account the above volumetric effects. Thus, this effect can be important when comparing systems with the same reservoir concentration but different volumes.

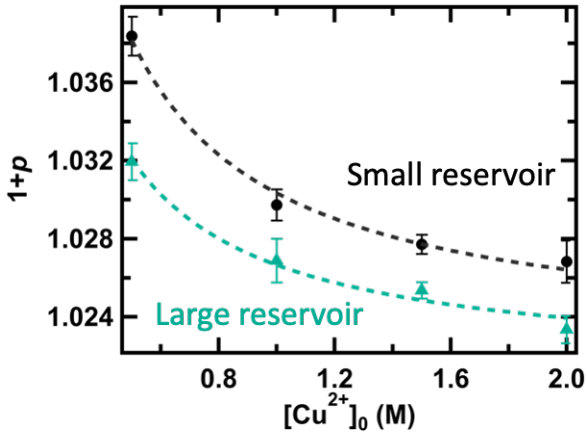

Figure 2.8. Plot of $1+p$ as a function of $[Cu^{2+}]_0$. The value of p is calculated by the average saturation value of x_{n+1}/x_n in Figures 2.3e and 2.4e. Black circles and red triangles represent the data of the small and large volume conditions, respectively. Dashed line is fitting curve based on eq. (8).

2.3.4 Numerical simulation based on RD equation

In order to interpret the volume effects observed in Sec. 2.3.1-2.3.3 in direct relation to the F_{diff} and LP formation dynamics, numerical simulations using the RD equation have been performed in this section. The RD equation of an LP system based on the nucleation-based scenario usually consists of the terms of electrolyte diffusion, reactions between electrolytes, nucleation, particle growth, aggregation, and precipitation, as described in Sec. 1.7.2. In particular, LPs formation by salt formation reactions have been modeled by the pre-nucleation model so far.[60, 68, 82, 87] In previous studies, simulations using this model were in good agreement with the experimental results using salt formation reactions, so this study adopted this model.[60, 71, 115] The expected reactions in this study,

nucleation, growth, and precipitation processes are:

$Cu^{2+}(aq) + CrO_4^{2-}(aq) \rightarrow CuCrO_4(aq)$ when $[Cu^{2+}][CrO_4^{2-}] \geq K_1$ (38)

$mCuCrO_4(aq) \rightarrow CuCrO_4(s)$ when $[CuCrO_4] \geq K_2$ (39)

where m is the number of salt molecules in a $CuCrO_4$ colloid particle, and these reactions represented based on eqs. (20)-(22). Based on eqs. (38) and (39), the RD equations in this study can be written as follows:

$$\frac{\partial a}{\partial t} = D_a \frac{\partial^2 a}{\partial x^2} - k_1 R(a,b)\theta(ab - K_1) \quad (40)$$

$$\frac{\partial b}{\partial t} = D_b \frac{\partial^2 b}{\partial x^2} - k_1 R(a,b)\theta(ab - K_1) \quad (41)$$

$$\frac{\partial c}{\partial t} = D_c \frac{\partial^2 c}{\partial x^2} + k_1 R(a,b)\theta(ab - K_1) - k_2 c\theta(c - K_2) - k_3 cN(c,p) \quad (42)$$

$$\frac{\partial p}{\partial t} = k_2 c\theta(c - K_2) + k_3 cN(c,p) \quad (43)$$

where a, b, c, and p are the concentrations of A (Cu^{2+}), B (CrO_4^{2-}), C ($CuCrO_4(aq)$), and P ($CuCrO_4$ precipitates); D_A, D_B, and D_C are the diffusion coefficients of these species; and k_1, k_2, and k_3 are the rate constants for salt formation reaction, nucleation, and growth, respectively. We used no-flux boundary conditions at the end of the calculation space (1 cm×14.5 cm). Also, the function R is the reaction function given by

$$R = \delta(a,b)[c_r + (1 - c_r)r] \quad (44)$$

where c_r is the coefficient determining the degree of stochasticity of the reaction ($0 \leq c_r \leq 1$), and r is a random number uniformly distributed within [0, 1]. The value of δ depends on the electrolyte concentrations: $\delta = a$ if $a < b$, and $\delta = b$ if $a > b$. Functions of $\theta(ab - K_1)$ and $\theta(c - K_2)$ are step functions: $\theta(ab - K_1) = 1$ and 0 when $ab - K_1 \geq 0$ and < 0, and $\theta(c - K_2) = 1$ and 0 when $c - K_2 \geq 0$ and < 0, respectively. In addition, the function $N(c, p)$ represents the growth and precipitation pathway at a banding position x_p with pre-formed precipitates: $N(c, p) = 1$ when either (i) $p(x_p) > 0$ or (ii) when $p(x_p) = 0$ but $p(x_{p+1}) > 0$ and $c(x_p) >$ growth threshold (K_3), otherwise $N(c, p) = 0$. This function implies that the growth-precipitation process occurs only at and/or near pre-existing precipitates. Furthermore, the initial parameters used in our simulation are as follows: $a_0 = 0.50$–2.0 M, $b_0 = 1.0 \times 10^{-2}$ M, $D_a = D_b = D_c = 1.0 \times 10^{-5}$ cm^{-2} s^{-1}, $k_1 = 1.0$ M^{-1} s^{-1}, $k_2 = k_3 = 1.0$ s^{-1}, $K_1 = 1.0 \times 10^{-12}$ M^2, $K_2 = 3.0 \times 10^{-3}$ M, $K_3 = 2.0 \times 10^{-3}$ M, and total time $t =$ 604800 s. The five-point formula with the space grid $\Delta x = 0.01$ cm was employed on a 1 cm × 14.5 cm grid (in which an area of 1 cm × 12.0 cm is the reaction space corresponding

to the gel in experiments, and another one of 1 cm × 2.5 cm is the reservoir of A), and the fourth-order Runge-Kutta method with time step Δt = 1 s was used to integrate the semi-discretized ordinary differential equations. This simulation used $K_1 = 1.0 \times 10^{-12}$ M^2, however the correct K_1 value for $CuCrO_4$ is much higher (~10^{-6} M^2).[135] However, previous study's RD simulations were performed without considering the correct K_1.[71] Since the experimental results were faithfully reproduced in such condition, it is unlikely that this difference will affect the simulation results. Also, the value of $D_{A\text{-}C}$ was chosen close to an actual value of Cu^{2+} diffusion in water and a hydrogel.[136-137] Therefore, the simulated values, especially the diffusion concentration profile of A, were close to the actual results of Cu^{2+} diffusion. Furthermore, the most important issue of parameters setting in this simulation is how to incorporate the effects of reservoir volume. Experimentally, we only changed the volume of the reservoir with constant stirring to maintain a constant uniform concentration of the reservoir solution, however it was difficult to incorporate such a stirring effect. If this uniformity cannot be guaranteed diffusion in the reservoir cannot be ignored in simulations with large reservoirs and the concentration gradient in the reservoir must be considered. Instead, we made the reservoir concentration (a_{res}) a function of elapsed time (expressed as $a_{res}(t)$). In the condition corresponding to the small reservoir, this concentration decreases over time as A diffuses into the reaction space according to the Fick's law, namely the concentration in the reaction space and the concentration in the reservoir approaches equilibrium. Therefore, $a_{res}(t)$ decrease with the amount of diffusion over time in this condition, which is called the "decreased $a_{res}(t)$ condition" in this study. This corresponds to the behavior described in Figure 2.2c. In contrast, in a sufficiently large reservoir, the concentration should remain fairly constant during pattern formation. Therefore, in this study, $a_{res}(t)$ is fixed at a constant value, which was achieved by applying the Dirichlet boundary condition at the boundary between the A reservoir and the reaction space. Thus, this condition is called a "fixed $a_{\mathrm{res}}(\mathrm{t})$ condition" and must correspond to the behavior described in Figure 2.2b.

Figure 2.9 shows simulation results of concentration profile of P with different a_0 both the decreased $a_{res}(t)$ and the fixed $a_{res}(t)$. A clear discrete precipitation profile was formed in all conditions and there is no significant visual difference. From this figure, x_n then was read as a position of each peak. Figure 2.10 shows simulation results of x_{n+1}/x_n under decreased and fixed $a_{res}(t)$ conditions. When the decreased $a_{res}(t)$ condition, x_{n+1}/x_n is almost constant for all n, and this constant value increases as a_0 decreases, then becomes maximal at a_0 = 0.5 M for all given a_0 values (Figure 2.10a). However, the experimentally observed increase in x_{n+1}/x_n when n was small was not reproduced in the simulation. Based on mentioned earlier in the discussion for Figure 2.6, this discrepancy might be

due to the exclusion of unsteady states from the simulation. Such unsteady states corresponded to excessive aggregation or precipitation, which produces the dense precipitation region (without discrete bands) in the experiment, but not in the simulation. In other words, the simulation reproduced only the band structure in experiments, where the ratio of x_{n+1}/x_n converges to a constant. This is because our simulation model considers only the pure RD process, which consists of a combination of diffusion, nonlinear chemical reactions and precipitation, and excludes other related experimental factors such as variation in nucleation probability due to gel structure heterogeneity. However, such simplifications are very important to demonstrate the effect of experimentally controlled factors (e.g, the condition of reservoir in this study) on the pattern formation mechanism. Similar to the decreased $a_{res}(t)$ condition in Figure 2.10a, the constant value also becomes maximal at a_0 = 0.5 M in the case of the fixed $a_{res}(t)$ condition (Figure 2.10b). To compare the results of the two conditions in terms of the MP law, the value of $1+p$ is estimated using the same procedure shown in Figure 2.8 and plotted against a_0 in Figure 2.10c. As a result, it was found that $1+p$ gradually decreases with increasing a_0 under both $a_{res}(t)$ conditions. And these data shows good agreement with the fitted curves form the classical MP law. Furthermore, in the condition where $a_{res}(t)$ is decreasing (Figure 2.10c●), the value of $1+p$ shows a maximum value at a_0 = 0.5 M and finally decreases to 1.12 at a_0 = 2.0 M. Similarly, in the condition where $a_{res}(t)$ is fixed (Figure 2.10c▲), the value of $1+p$ shows a maximum value at a_0 = 0.5 M and gradually decreases as a_0 increases. For the same a_0, $1+p$ is smaller in the condition with fixed $a_{res}(t)$ than in the condition with decreased $a_{res}(t)$, which is also good agreement with the experimental results in Figure 2.8. The difference between the two $a_{res}(t)$ gives rise to a difference in the evolution of the concentration gradient (shown as Figure 2.2), namely, in the change in F_{diff} as expressed in equations (35) and (36). Therefore, the experimentally observed difference in $1+p$ when changing the volume of the $CuCl_2$ reservoir was caused by the difference in diffusion behavior expressed by the eqs. (35) and (36).

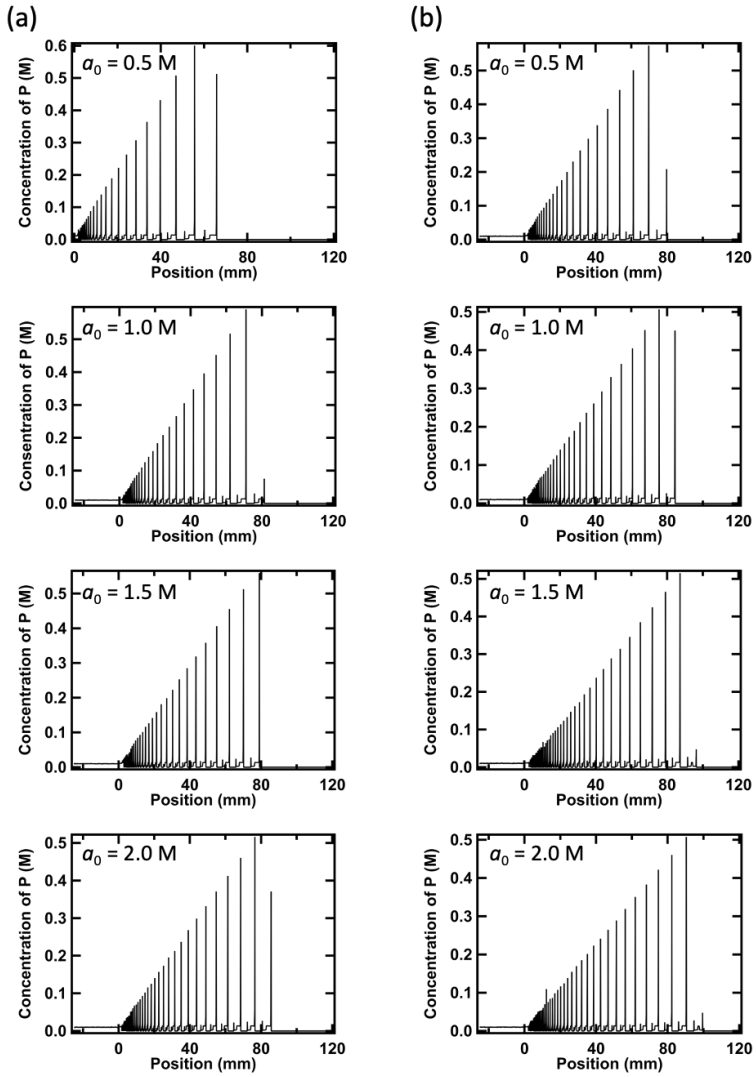

Figure 2.9. Simulation results of concentration profiles of P under different a_0. (a) deceased $a_{res}(t)$ and (b) fixed $a_{res}(t)$ conditions. The x_n value is a position where existence of a peak for p.

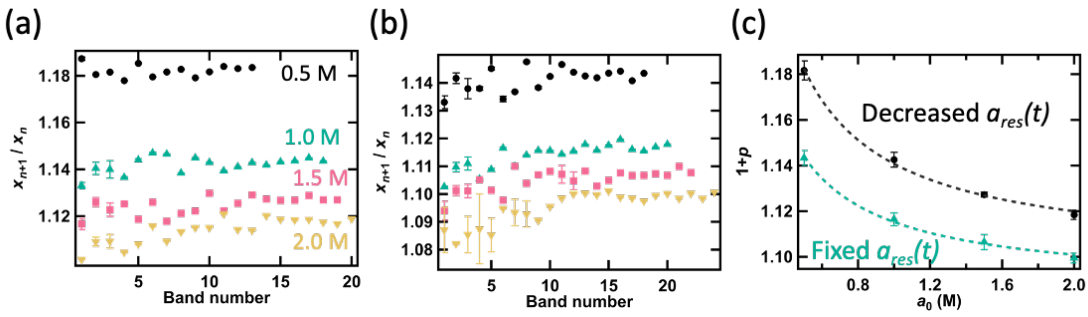

Figure 2.10. Variation of x_{n+1}/x_n with any a_0 values under two reservoir conditions: (a) decreased $a_{res}(t)$ and (b) fixed $a_{res}(t)$ (a_0 = ●: 0.5 M, ▲: 1.0 M, ■: 1.5 M, and ▼: 2.0). (c) Dependency of 1+p to a_0. The black circles and green triangles represent the data under decreased $a_{res}(t)$ and fixed $a_{res}(t)$. The dashed line shows the curve approximated based on eq. (8).

In order to discuss the difference in the $1+p$ due to the reservoir condition even at the same a_0 from the perspective of evolution of the diffusion gradient, the time-course changing of the diffusion profile under the two conditions is shown in Figure 2.11. This simulation was performed by deleting terms for all reaction substrates except A, namely, applying Fick's diffusion equation using only the diffusion term in eq. (40) to obtain the time course of the diffusion gradient under each reservoir condition. The time variation of the concentration of A was simulated based on Fick's law for the diffusion behavior with decreasing and fixed $ar_{es}(t)$ corresponding to equations (35) and (36). Figure 2.11a and b show the time evolution of the diffusion profiles every 21 hours when $a_{res}(t)$ was decreased from $a_0 = 0.5$ M (the small reservoir) and $a_{res}(t)$ was fixed with a_0=0.5 M (the large reservoir). Under the decreased $a_{res}(t)$ condition, electrolyte in the reservoir was gradually decreased with time, as the diffusion profile evolved toward the edge of reaction space (Figure 2.11a) due to the diffusion of A. On the other hand, electrolyte concentration in the reservoir under the fixed $a_{res}(t)$ condition remained constant with time (Figure 2.11b). According to Fick's law, F_{diff} is proportional to the concentration gradient,[55] and so a steeper diffusion gradient should promote diffusion. Namely, the concentration gradient in the case of decreased $a_{res}(t)$ condition becomes gentler as A is depleted, while for the fixed $a_{res}(t)$ condition the concentration gradient remains steep. Indeed, F_{diff} for the case of fixed $a_{res}(t)$ is relatively high with time. This fact becomes clear when comparing the area under the final diffusion profile at $x > 0$ cm after 168 hours (Figure 2.11c). For the same $a_0 = 0.5$ M, the area under the fixed $a_{res}(t)$ condition (dashed line) is larger than the area under the decreases $a_{res}(t)$ condition (solid line).

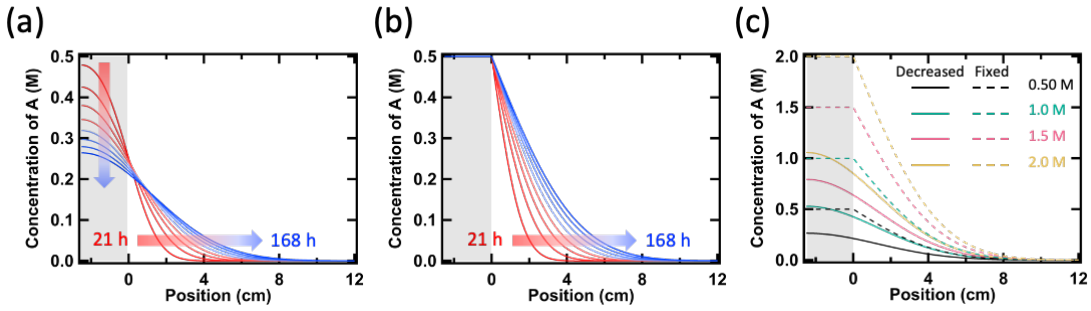

Figure 2.11. Diffusion concentration profile of A every 21 h under (a) decreased and (b) fixed $a_{res}(t)$ conditions, both with $a_0 = 0.5$ M. (c) Final diffusion profiles after 168 h for different a_0 values. The solid and dashed line represent the decreased and fixed reservoir conditions, respectively. The pale gray area at $x < 0$ cm represents the reservoir region. In addition, the interface between the reservoir and the reaction space is defined as $x = 0$ cm, which is needed as a reference to find x_n.

Furthermore, the fact that the gradient was still maintained in all profiles after 168 h indicates that a system has not reached equilibrium state. Therefore, the actual $[Cu^{2+}]_{res}$ in the large reservoir after 168 h was higher than the corresponding the calculated $[Cu^{2+}]_{res}$ equilibrium value of $0.84\times[Cu^{2+}]_0$ in the experimental section. On the other hand, the actual $[Cu^{2+}]_{res}$ after 168 h could be calculated by comparing the amount of diffusing Cu^{2+} (n_{diff}) with the initial amount in the reservoir (n_{res}). n_{diff} is calculated using the following equation:

$$n_{diff} = (\int_0^h [Cu^{2+}]_{diff} dx) \times S \times 10^{-3} \qquad (45)$$

where $[Cu^{2+}]_{diff}$ is the concentration of Cu^{2+} at each position ($x > 0$) in Figure 2.11c, and its integral value corresponds to the area under each profile at x > 0 in Figure 2.11c. S is the cross-sectional area of the gel (cm^2) calculated from ∅ and h. Also, n_{res} is calculated by multiplying $[Cu^{2+}]_0$ and V_{res}. The calculation of eq. (45) allows us to check whether the large reservoir condition used in this study (V_{res} = 50 mL) corresponded the infinite condition represented by eq. (36). As a result, $[Cu^{2+}]_0$ = 2.0 M had $n_{res} = 1.0\times10^{-1}$ mol for the large reservoir (V_{res} = 50mL). The value of n_{diff} after 168 h was calculated from eq. (45) to be 8.3×10^{-3}mol. Thus, $n_{diff}/n_{res} \approx 1/10$, i.e. the actual $[Cu^{2+}]_{res}$ was $0.92\times[Cu^{2+}]_0$. Therefore, since the Cu^{2+} concentration in the reservoir hardly changed, it was appropriate to use a fixed a_{res}(t) condition to simulate the large reservoir conditions used in the experiment.

2.3.5 Expression of periodicity as a function of F_{diff}

As we mentioned above, F_{diff} was the key factor determining the periodicity of LPs.[101, 103, 132] Recently, it has been reported that when F_{diff} of OH^- (as an outer electrolyte) was controlled using a polymer hydrogel containing carboxylic acid residues as the reaction medium, the morphology of the obtained pattern was changed between band (ring) and spot structures.[125] The common denominator in all the above studies is that F_{diff} is strongly involved in the LP formation mechanism, irrespective of the intrinsic or extrinsic control techniques used in the system. However, the classical MP law did not take into account factors other than the initial concentrations of outer and inner electrolytes, in particular the variation of F_{diff}. Therefore, by expressing the MP law directly in terms of F_{diff}, it is possible to describe the periodicity modulation of LP by reservoir and other conditions in a unified way. Then, we attempted to estimate the F_{diff} for each reservoir condition using the following procedure. Firstly, F_{diff} was defined as the amount of Cu^{2+} diffusion per unit time and unit area (mol $cm^{-2}s^{-1}$). Although it actually changed with time

because diffusion is proportional to the diffusion gradient, we assumed it to be a constant during the pattern formation as:

$$F_{diff} = n_{diff}/2St \qquad (46)$$

where t = 604800 s (corresponding to 168 h). This estimated F_{diff} represents the average diffusion flux during pattern formation according to the above approximation. To estimate the F_{diff}, we first calculated n_{diff} under each reservoir condition and $[Cu^{2+}]_0$ using equation (45) and Figure 2.11c. The obtained values of n_{diff} are shown in Tables 2.1 and 2.2.

Table 2.1 Values of n_{diff} and F_{diff} for all $[Cu^{2+}]_0$, calculated using eqs. (45) and (46) in the small reservoir (decreased $a_{res}(t)$) condition.

$[Cu^{2+}]_0$ (M)	0.50	1.0	1.5	2.0
n_{diff} (mol)	0.99×10^{-3}	2.0×10^{-3}	3.0×10^{-3}	4.0×10^{-3}
F_{diff} (mol/m^2 s)	1.0×10^{-5}	2.1×10^{-5}	3.1×10^{-5}	4.1×10^{-5}

Table 2.2 Values of n_{diff} and F_{diff} for all $[Cu^{2+}]_0$, calculated using eqs. (45) and (46) in the large reservoir (fixed $a_{res}(t)$) condition.

$[Cu^{2+}]_0$ (M)	0.50 M	1.0 M	1.5 M	2.0 M
n_{diff} (mol)	2.1×10^{-3}	4.2×10^{-3}	6.3×10^{-3}	8.3×10^{-3}
F_{diff} (mol/m^2 s)	2.2×10^{-5}	4.4×10^{-5}	6.6×10^{-5}	8.7×10^{-5}

We then converted the calculated n_{diff} into F_{diff} using eq. (46) and the results of the conversion to F_{diff} are also shown in Tables 2.1 and 2.2. The above procedure converted the $[Cu^{2+}]_0$ for each reservoir condition into the corresponding F_{diff} via n_{diff} and transformed the plot of the classical MP law as a function of $[Cu^{2+}]_0$ into a modified one as a function of F_{diff} (Figure 2.12). While Figures 2.8 and 2.10c showed that the small and large reservoirs had different values of $1+p$ regardless the same $[Cu^{2+}]_0$, the experimentally obtained value ($1+p_{exp}$) gradually decreases with increasing F_{diff} (Figure 2.12a) in the case of re-plotted by using F_{diff} and finally settles at about 1.02.

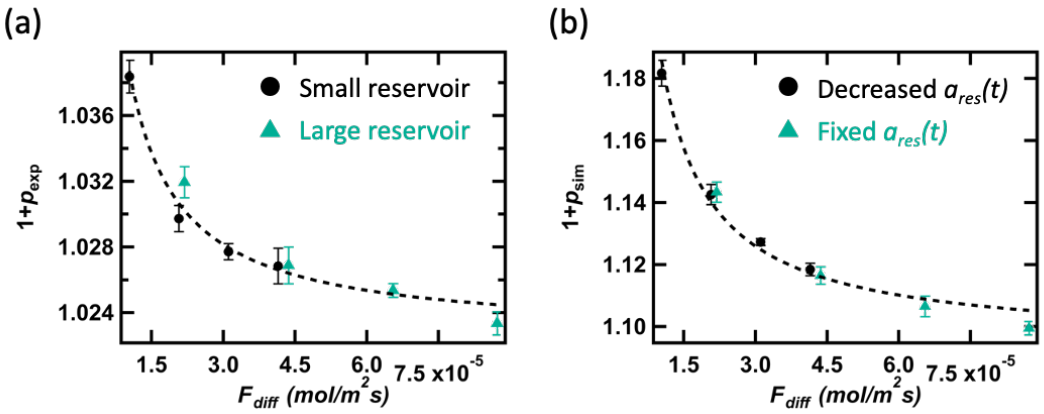

Figure 2.12. Variation of obtained 1+p as a function of estimated F_{diff} from (a) experiments and (b) simulation. The closed circle and triangle indicate data for the small (decreased $a_{res}(t)$) and large (fixed $a_{res}(t)$) reservoir conditions. The dashed lines show the fitted curves based on the equation replacing a_0 with F_{diff} in eq. (8).

Furthermore, the plot agrees well with the fitted curve based on the modified equation (8) where a_0 was replaced by F_{diff} (dashed line). Similarly, the simulated value (1+p_{sim}) gradually decreases and converges to a constant value (Figure 2.12b), and in good agreement with the fitted curve and the experimental results. It is therefore clear that the change in periodicity due to reservoir conditions is correctly described by F_{diff}, which is estimated by the time evolution of the diffusion gradient profile, instead of pre-defined $[Cu^{2+}]_0$ as used in the classical MP law. This practical expression using F_{diff} can also be applied to previous work where F_{diff} was controlled without changing the electrolyte concentration (as discussed in the Introduction). As F_{diff} increases, the local supersaturation near the reservoir increases. This results in the formation of a band of precipitates is closer to the interface and a decrease in 1+p. This explains how 1+p can vary with reservoir conditions for the same $[Cu^{2+}]_0$. From the above consistent results, when discussing the spatial periodicity in various LP systems, it is necessary to modify the MP law by using F_{diff} instead of a_0 to describe the dependence of diffusion behavior caused by other than changes in electrolyte concentration (e.g. the volume effect). This will increase the versatility of the MP law.

2.4 Conclusions

The effect of the volume of the reservoir on the periodicity of the formed LP was experimentally investigated in this study. Good agreement with the classical MP law was obtained for both large and small volumes, however different values of $1+p$ were obtained for the same $[Cu^{2+}]_0$. This result was inconsistent with the classical MP law, which describes 1+p as a function of the initial electrolyte concentrations only. The reason for this discrepancy was investigated on the basis of RD simulations, after introducing reservoir conditions suitable for temporal concentration changes in the reservoir. As expected, F_{diff} was higher when a larger reservoir was used instead of a smaller one for the same $[Cu^{2+}]_0$. We then determined the value of $1+p$ for the two reservoir conditions as a function of the F_{diff} estimated by the final diffusion gradient from both experiment and simulation. The results showed that $1+p$ was almost identical for these reservoir volume conditions when plotted as a function of F_{diff} instead of a_0 as used in the classical MP method. Furthermore, this behavior was not only observed experimentally, but was also reproduced in simulations incorporating F_{diff}. Thus, the classical MP method can be modified to be a function of F_{diff} instead of a_0, to accurately describe systems with the same a_0 but different diffusion gradients. This modification leads to a scaling of the MP law for a more tool to evaluate LP formation under the nucleation-based scenario. However, this modification of the MP law only applies to the outer electrolyte and the influence of the inner electrolyte on the formation mechanism is unknown. Further systematic investigations are needed to clarify the relationship between the inner electrolyte and the MP law, in order to build a more robust tool. To the best of our knowledge, this is the first quantitative example of the relationship between LP periodicity and the diffusion flux, a key parameter characterizing the dissipative structure. This work will allow us to read the periodicity of the analogous LPs formed by the nucleation-based scenario in nature, and to understand the nonequilibrium environment to form of them, namely the conditions of the fluxes.

Chapter 3 Revealing the Factor of Geometrical Transition Based on a Spatial Modulation of Nucleation

3.1 Introduction

Most of LPs formed in experiments show the regular-type introduced in Sec. 1.6.3, where an interband spacing (Δx_n) increases linearly with increasing x_n (Figure 3.1 black line). This relationship is shown in eq. (7), which is derived from the spatial law. However, it has been reported that the equidistant-type (Figure 3.1 green line) and the revert-type (Figure 3.1 yellow line) was rarely formed in some salt formation systems (e.g. silver halides[105-107, 138] and $PbCrO_4$[108-109, 139]).

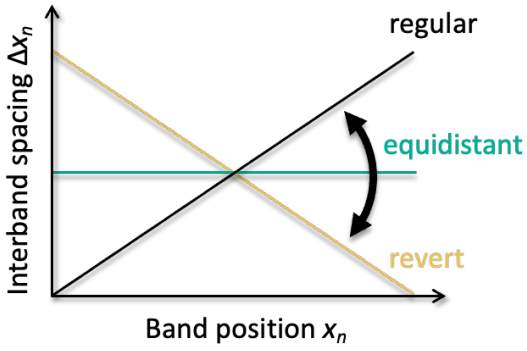

Figure 3.1. Variation of Δx_n as a function of x_n in cases of three types of LPs.

These exceptional patterns are characterized by the spontaneous formation of structures, even though they involve a reaction system similar to that of the regular-type of pattern formation. As we mentioned Sec. 1.7.2, the periodicity in the nucleation-based scenario is defined by the nucleation process. Actually, my previous study revealed that modulating a nucleation threshold (K_2) that is a controlling parameter of nucleation rate in Liesegang reaction processes controlled the regular-type LP periodicity.[60] Thus, although the kinetics of nucleation is an important parameter for understanding the self-organization process in the nucleation-based scenario, few studies have discussed the transition of geometries to the above-mentioned exceptional LPs in terms based on it. In nature, especially in geological analogue patterns such as agate rocks, complex periodicities consisting of single or combined patterns of such transitions are found.[140] Therefore, understanding exceptional LP formation in terms of nucleation is an essential process in modelling the formation of these similar patterns.

In this context, the previous simulation study based on the nucleation-based scenario

showed that a spatiotemporal K_2 modulation controls such transition phenomena (Figure 3.2).[102]

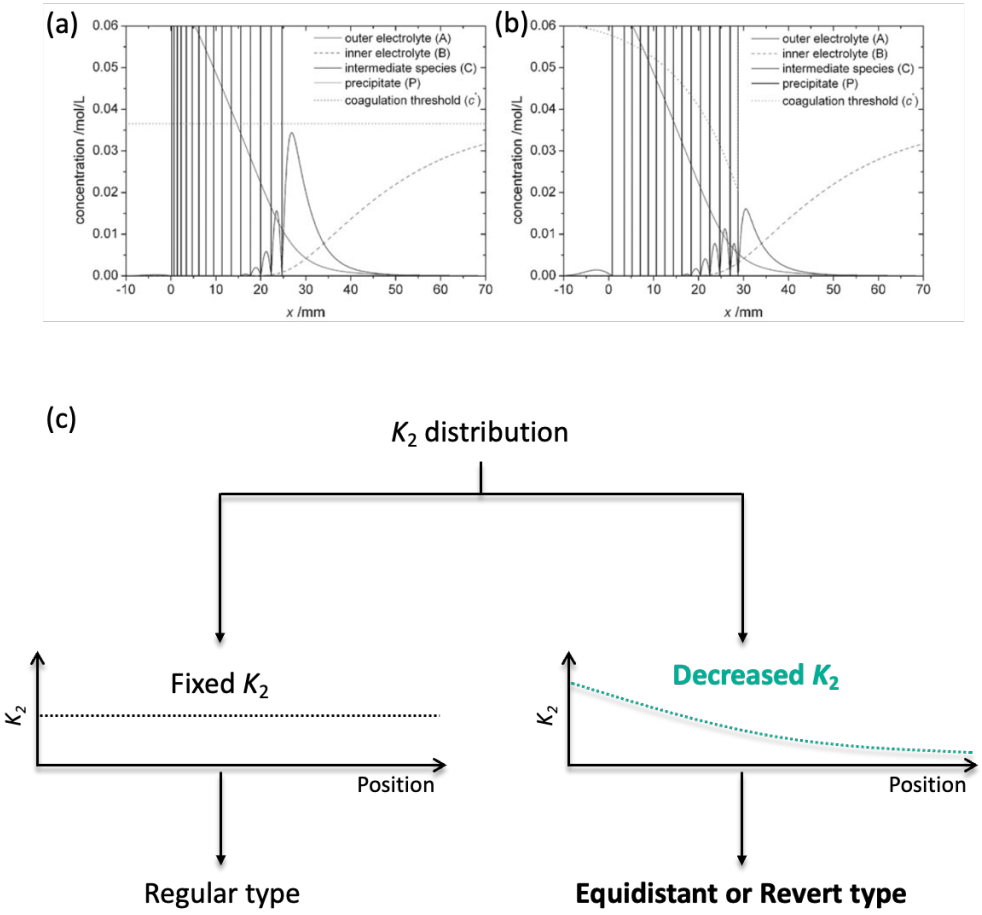

Figure 3.2. Pattern formation by numerical simulation based on the nucleation-based scenario in (a) fixed K_2 and (b) spatial decreased K_2. In the former condition a regular-type was formed, while in the latter an equidistant-type of LP was formed. These figures were reprinted with permission from Ref. 102. Copyright 2008 Royal Society of Chemistry. (c) Scenario of pattern transition based on the spatial distribution of K_2.

When K_2 was distributed spatially, which is a condition typically expected in LP formation (Figure 1.20), the regular-type was formed (Figure 3.2a). On the other hand, the equidistant- or revert-type were formed when K_2 was decreased further away from the interface of the gel (Figure 3.2b). Therefore, this simulation indicated that the spatial distribution of K_2 determines the pattern periodicity whether the regular-type or exceptional types (Figure 3.2c). Since K_2 is an equilibrium constant, the simplest way to spatially modulate it is to make the temperature of the system non-uniform. However, it was reported that such temperature changes not only modulated the balance of the elementary processes of LP formation, but also induced unexpected morphological

changes (e.g. helix formation).[123] Therefore, this seemingly simple technique highlights the factors other than nucleation kinetics, making it difficult to focus on the importance of nucleation. While, it has been found that the concentration of the gel modulates only K_2 and thus controls the periodicity of the pattern (Figure 3.3).[71]

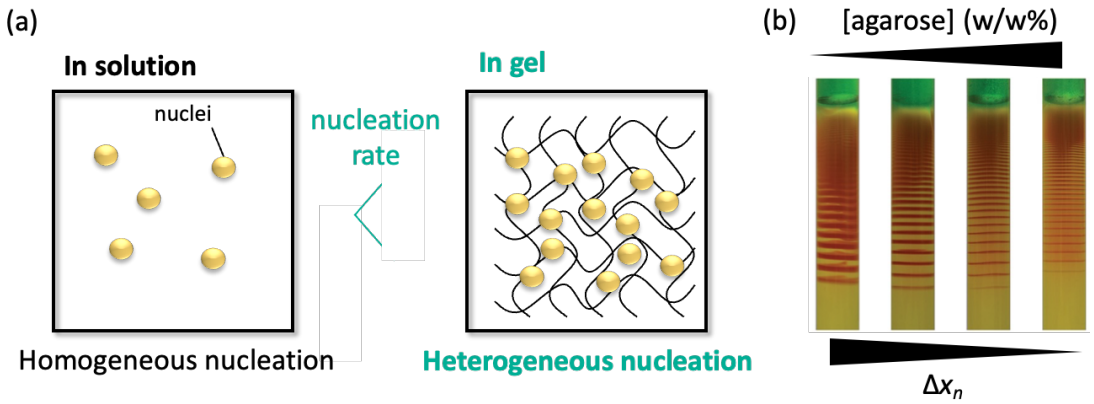

Figure 3.3. (a) Difference of nucleation rate between in a solution and a gel. (b) Variation of Δx_n with the change in an agarose concentration, which was reprinted with permission from Ref. 71. Copyright 2008 American Chemical Society.

The hydrogel is consisted of network structure of hydrophilic polymers in water, which is acting as a nucleation cite.[70, 141] In other words, it shows homogeneous nucleation in clean solutions, whereas heterogeneous nucleation occurs preferentially in gels (Figure 3.3). Therefore, gels promote nucleation more than solutions, and this promotion is proportional to the density of the gel, namely the concentration, because the gel network is denser in proportion to the concentration.[134] The above previous studies have found that increasing gel concentration actually promotes nucleation, namely decreases K_2, and that the pattern becomes finer with increasing gel concentration (Figure 3.3). However, all previous studies of LPs formation have used mono-layered gels with spatially uniform K_2, so that the variation of K_2 remains within a constant spatial change (Figure 3.4a). Therefore, this study focused on modulating the spatial distribution of the gel concentration by making multi-layered gels with different gel concentrations as the most optimal method to modulate the spatial distribution of K_2 (Figure 3.4b). The aim of this chapter is to discuss the transition of LP's geometries based on such a spatial modulation of K_2.

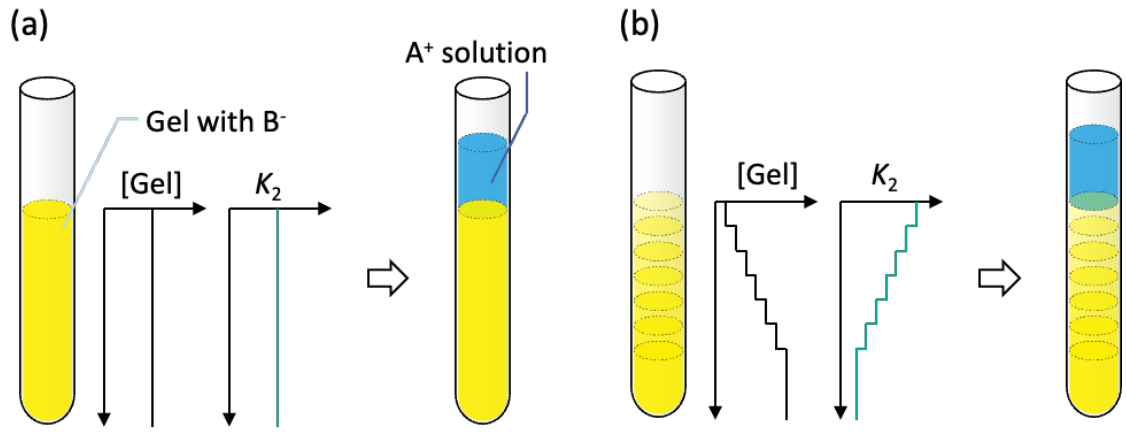

Figure 3.4. Illustration of gel preparation based on (a) a conventional study and (b) this study. The K_2 distribution is correlated with the gel concentration distribution.

3.2 Experiments

3.2.1 Reagents and instruments

Agarose (fine powder), $CuCl_2 \cdot 2H_2O$, and K_2CrO_4 the same as those used in chapter 2. Also, observation and analysis of obtained patterns were carried out using the same equipment and software as in Chapter 2.

3.2.2 Sample preparation for mono-layered gel systems

The agarose sol doped with K_2CrO_4 was preparade following the same procedure described in Sec. 2.2.2, where the agarose concentration ([agarose]) was adjusted range from 0.25 to 4.0 w/w%. Then, prepared this hot sol was poured into a glass tube ($\varnothing$ =1.0 mm) to a height of 90 mm (Figure 3.5a). The sample was allowed to gelation completely by standing at 18°C for 6 h. After gelation, an aqueous solution of $CuCl_2$ (0.50 M, 5.0 mL) was poured on the gel. Immediately after that, Cu^{2+} started to diffuse into the gel, and $CuCrO_4$ precipitates appeared from the interface by salt formation reaction denoted as eq. (37). The duration of pattern formation was fixed at 1 week in all cases with different agarose concentrations, and all reactions were carried out in an incubator at 18°C. After pattern formation, the $CuCl_2$ solution was removed and the light transmitted through each sample was observed under a stereomicroscope with a CCD camera.

3.2.3 Sample preparation for bi-layered gel systems

The agarose sol prepared as described above was poured into a glass tube to a height of 30 mm (Figure 3.5b). This part of the gel was the lower part, and the agarose concentration, expressed as $[agarose]_{lower}$, was adjusted range from 1.0 to 4.0 w/w%. After the gelation of this part, another hot agarose sol was poured on the top of this part up to a height of 60 mm. This upper gel part was called as the upper gel and its agarose concentration ($[agarose]_{upper}$) was fixed at 0.25 w/w% for all samples. Pattern formation and image analysis were then carried out using the procedure described in the previous section.

3.2.4 Sample preparation for multi-layered gel systems

Pattern formation in multi-layered gels was carried out under following two conditions: (i) a stepwise decrease in agarose concentration (Figure 3.5c), and (ii) repetition of high and low agarose concentrations (Figure 3.5d). The detail procedure for the preparation of each gel was as follows.

Condition (i): Stepwise decrease in agarose concentration (Figure 3.5c)

Firstly, a 9th (the lowest) agarose gel layer ([agarose] = 4.0 w/w%) was prepared at a height of 15 mm from the bottom of the glass tube. The next gel layer (8th layer) was prepared at a height of 5 mm. This procedure was repeated six times to obtain a total of seven thin gel layers. The final agarose concentrations were fixed at 3.5 (8th layer), 3.0 (7th layer), 2.5 (6th layer), 2.0 (5th layer), 1.5 (4th layer), 1.0 (3rd layer) and 0.50 w/w% (2nd layer). After gelation of the 2nd layer, 0.25 w/w% agarose sol was poured up to a height of 40 mm from the 2nd layer to form the 1st gel layer (the topmost layer). As a micropipette (Eppendorf, Eppendorf Reference® 2, 100-1000 µL) was used to inject each sol, the error in the height of these layers was 0.18 mm, estimated by the systematic error (±0.6%) of this micropipette. Thus, a stepwise decrease in agarose concentration was obtained from the end of the 1st gel layer to the beginning of the 9th gel layer.

Condition (ii): Repeated high and low agarose concentrations (Figure 3.5d)

A 4th agarose gel layer (3.0 w/w%) was prepared at a height of 20 mm from the bottom of the glass tube. Then, a 3rd gel layer (0.25w/w%) was prepared at a height of 10 mm, a 2nd gel layer (3.0w/w%) at a height of 10 mm, and finally a 1st gel layer (0.25w/w%) at a height of 50 mm. In this way, regions of progressively higher and lower agarose concentration were repeatedly formed from the edge of the 1st gel layer to the edge of the 4th gel layer.

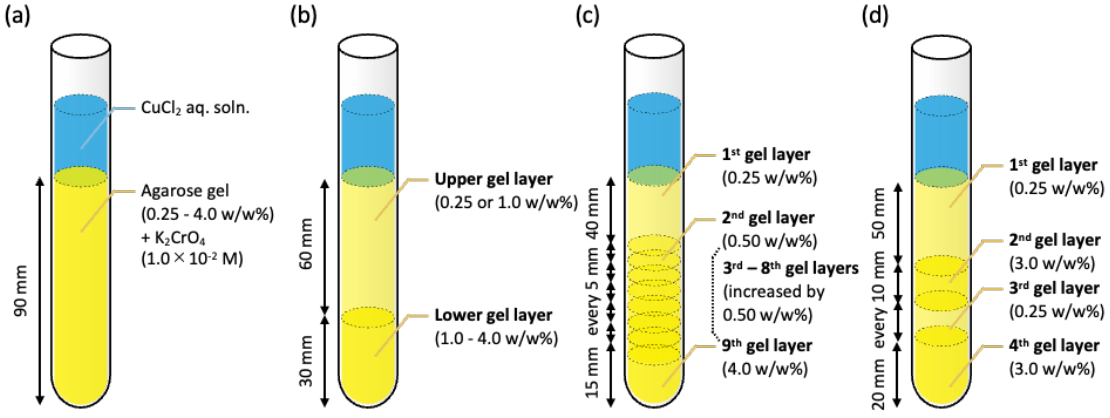

Figure 3.5. Illustration of the experimental set-up. (a) mono-layered gel, (b) bi-layered gel, (c) multi-layered gel with stepwise decrease in agarose concentration, (d) multilayer gel with stepwise increasing and decreasing agarose concentration.

3.3 Results and discussion

3.3.1 Pattern formation in mono-layered gels

Figure 3.6 shows the pattern formation in multi-layered gels when the concentration of agarose is varied from 0.25 to 4.0 w/w%.

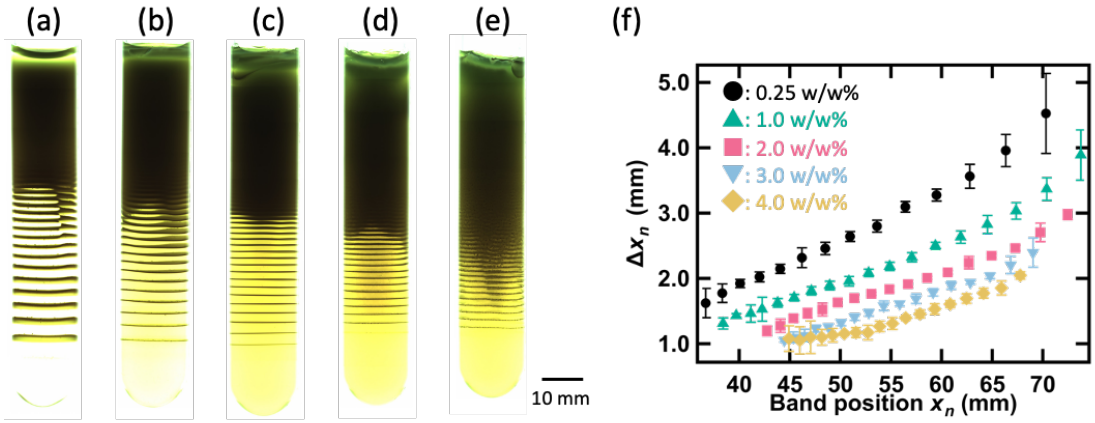

Figure 3.6. Pattern formation in in mono-layered agarose gels. (a) [agarose] = 0.25 w/w%, (b) 1.0 w/w% (c) 2.0 w/w%, (d) 3.0 w/w%, (e) 4.0 w/w%. (f) Relationship between Δx_n and x_n (●: [agarose] = 0.25w/w%, ▲: 1.0w/w%, ■: 2.0w/w%, ▼: 3.0w/w%, ◆: 4.0w/w%).

In all cases, discrete precipitates of $CuCrO_4$ were formed below the dense precipitate regions (Figure 3.6a-e), whose character was similar to the experiments in Chapter 2. Furthermore, the dense precipitates region appears to expand with increasing agarose concentration. This was because the increase in [agarose] reduced K_2 and promoted nucleation, Δx_n decreased and the bands were combined. We then calculated Δx_n from Figure 3.6a-e and plotted it in Figure 3.6f as a function of x_n. As a result, for [agarose] = 0.25 w/w%, Δx_n increases from 1.5 mm to 4.5 mm with increasing x_n (Figure 3.6f●). This positive linear proportional relationship indicates that a regular type of LP is formed (eq. (7)). Consistent with this result, Δx_n also increases at other agarose concentrations (Figure 3.6f▲-◆), indicating that regular-type LPs were formed at all agarose concentrations when the mono-layered gels were used. However, a comparison of the maximum values of Δx_n, it decreased from approximately 4.5 mm (0.25 w/w%) to 2.0 mm (4.0 w/w%) with increasing [agarose]. These results were good agreement with the previous study demonstrating the effect of gel concentrations in mono-layered gels.[71]

3.3.2 Numerical simulation under fixed K_2

In order to discuss changes in agarose concentration in mono-layered gels in relation to the kinetics of the nucleation process in the nucleation-based scenario, numerical simulations based on the RD equation were then performed. For the RD equations I have used eqs. (40)-(43) as described in Sec. 2.3.4 because the chemical reaction to form $CuCrO_4$ precipitates was same as the used system in Chapter 2. Also, we used same no-flux boundary conditions at the end of the calculation space (10 mm×120 mm), and the fixed $a_{res}(t)$ condition was used at the interface between the reservoir and the reaction space. Detail of simulation parameters were showed in Table 3.1.

Table 3.1 Parameters of the RD simulations

Total time steps (s)	a_0[a] (M)	b_0[b] (M)	D_a, D_b, D_c (cm^2s^{-1})	k_1 ($M^{-1}s^{-1}$)	k_1, k_2 (s^{-1})	K_1 (M^2)	K_3 (M)
604800	0.5	1.0×10^{-2}	1.0×10^{-5}	1.0	1.0	1.0×10^{-12}	1.8×10^{-3}

The key point in this simulation is the K_2 modulation, which controls the kinetics of nucleation in a nucleation-based scenario. Since we used the mono-layered gels in above experiments, K_2 was set to a fixed and spatial constant value in the calculation space. Figure 3.7a-d shows simulation results with different fixed K_2 ranged from 2.2×10^{-3} M to 3.7×10^{-3} M. Obtained patterns showed the Δx_n of each band pair decreases with decreasing K_2. In order to evaluate this trend more quantitatively, a Δx_n-x_n plot similar to that of Figure 3.6f was created (Figure 3.7e). As a consequence, as K_2 decreases, the system shows the decrease in a slope of Δx_n-x_n plot while retaining the regular-type features, which is very consistent with the results of the experiments in mono-layered gels described above. Therefore, it was clear that the increasing gel concentration induced the decreasing K_2, and by controlling the spatial distribution of this concentration it became possible to impose a spatial modulation of K_2.

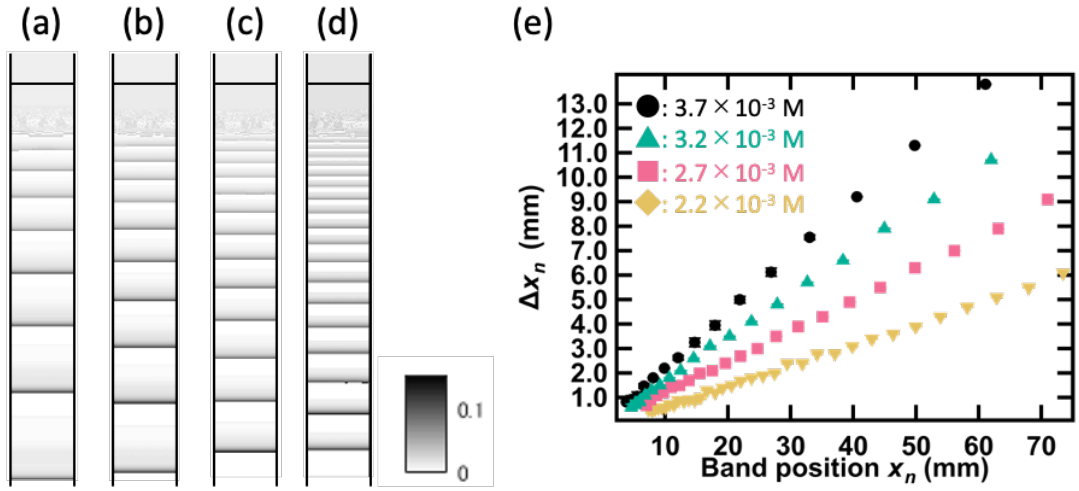

Figure 3.7. Output images of P distribution obtained from simulations with fixed K_2, where the solid horizontal black line in the column represents the boundary of the reservoir. (a) $K_2 = 3.7 \times 10^{-3}$ M, (b) 3.2×10^{-3} M, (c) 2.7×10^{-3} M, and (d) 2.2×10^{-3} M, respectively. (e) Variation of Δx_n as a function of x_n (●: $K_2 = 3.7 \times 10^{-3}$ M, ▲: 3.2×10^{-3} M, ■: 2.7×10^{-3} M, ▼: 2.2×10^{-3} M).

3.3.3 Pattern formation in bi-layered gels

Before demonstrating the effect of spatial changes in gel concentrations, we needed to investigate physical effects of the interface between two or more gel layers. To investigate it, pattern formation was carried out in the bi-layered gel with equal concentrations of the upper and lower gels ([agarose] = 1.0 w/w%) as a preliminary experiment (Figure 3.8).

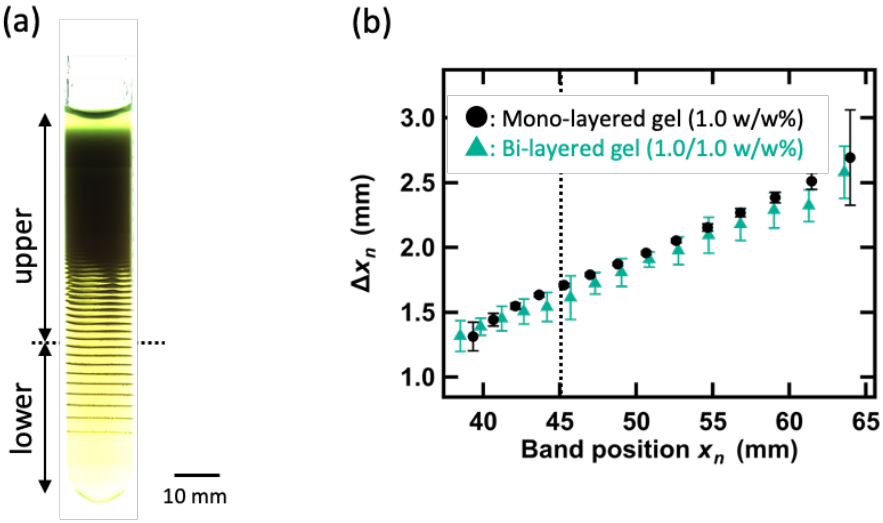

Figure 3.8. (a) Pattern formation in the bi-layered agarose gel constructed by 1.0 w/w% upper and lower agarose gels. (b) The relationship between Δx_n and x_n (●: 1.0 w/w% mono-layered gel, ▲: 1.0–1.0 w/w% bi-layered gel). The dotted line shows the gel–gel interface.

In this experiment, the interface was positioned at half of the gel (height of 45 mm). The results showed that the physical effect of the presence of the gel-gel interface on the pattern periodicity is negligible, as the pattern appearance and the change in Δx_n agree well with the 1.0 w/w% mono-layered gel.

Since these preliminary experiments made it clear that only the effect of spatial modulation of concentration could be considered in experiments with gels consisting of some layers, we then carried out pattern formation in bi-layered gels with different agarose concentrations in order to simply extract the intrinsic effect of modulation of gel concentration. Such bi-layered gels were made according to the procedures described in experimental section. Figures 3.9a-d show the typical LPs formed in bi-layered agarose gels with an upper layer with a fixed concentration ($[\text{agarose}]_{\text{upper}}$ = 0.25 w/w%) and a lower layer with different concentrations ($[\text{agarose}]_{\text{lower}}$ = 1.0-4.0 w/w%). In order to compare Δx_n variation between in mono-layered and bi-layered agarose gels, Δx_n-x_n plots obtained from both gel conditions were shown in Figure 3.9e,f. In the 0.25 w/w% mono-layered gel, Δx_n increases monotonically (Figure 3.9f●), which has already been found at the early results used the mono-layered gels, and indicated that only the regular-type LP were formed in the mono-layered gels. On the other hand, in the bi-layered gel, a complex Δx_n change as a function of x_n was observed near the interface between the upper and lower agarose gels (x_n = 60 mm, black dotted line). When $[\text{agarose}]_{\text{lower}}$ = 1.0 w/w% (Figure 3.9f▲), Δx_n increases monotonically, and this change was observed until a point behind the interface (x_n = 55 mm). On the other hand, Δx_n approaches a constant value from x_n = 55 mm to 65 mm, showing a different trend from that of the result of mono-layered agarose gel. The linear increase of Δx_n behind the interface suggested that the nucleation kinetics was already modulated even within the region of [agarose] = $[\text{agarose}]_{\text{upper}}$. A similar behavior was observed in the other conditions, $[\text{agarose}]_{\text{lower}}$ = 2.0-4.0 w/w% (Figure 3.9f■-◆). Furthermore, when the plots near the gel-gel interface in Figure 3.9f was enlarged in Figure 3.9g, the slope decreases and transitions from positive to negative as the magnitude of the gel concentration gap Δ[agarose] (= $|[\text{agarose}]_{\text{lower}} - [\text{agarose}]_{\text{upper}}|$) increases, where the zero and negative value of the slope indicates that obtained periodicity is equidistant- and revert-types. Thus, it is clear that both equidistant- and revert-type LPs are locally formed only near the gel interface in the bi-layered agarose gel, and that the type of LP can be transited following the pre-adjusted magnitude of Δ[agarose].

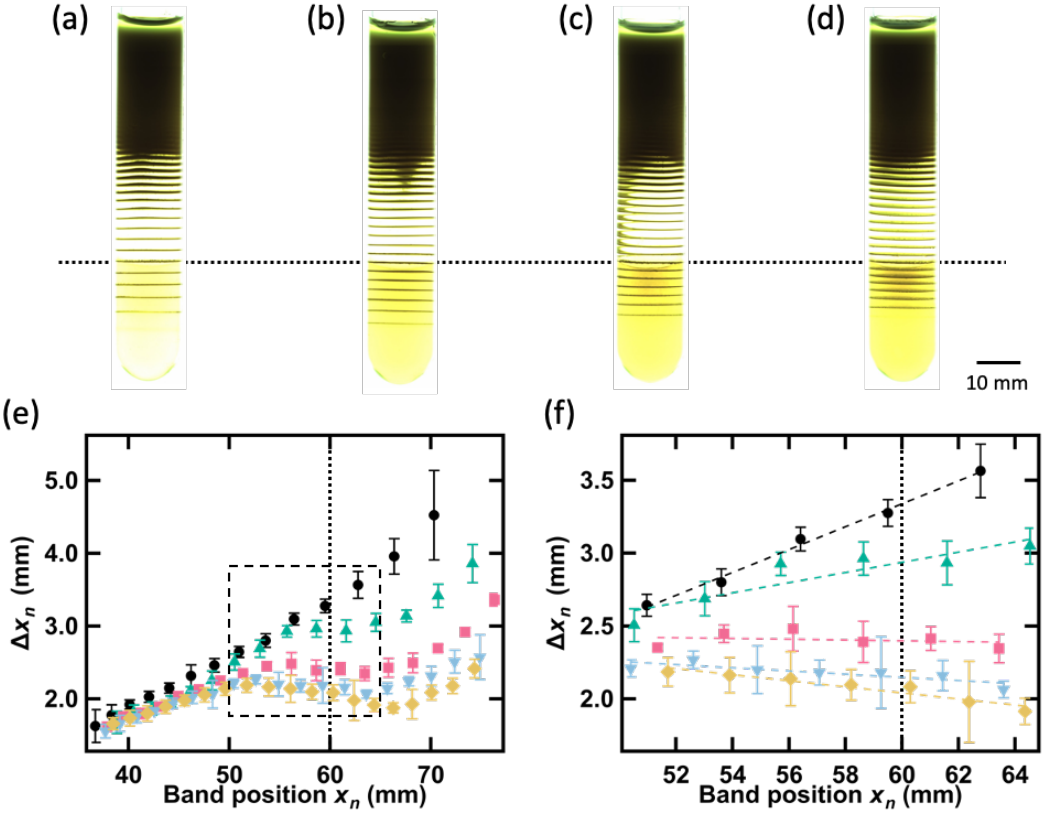

Figure 3.9. Pattern formation in bi-layered agarose gels constructed with a 0.25 w/w% upper agarose gel and (a) 1.0 w/w%, (b) 2.0 w/w%, (c) 3.0 w/w%, or (d) 4.0 w/w% lower agarose gel. (e) Relationship Δx_n and x_n (●: fixed [agarose] = 0.25 w/w% (mono-layered gel), $[\text{agarose}]_{\text{lower}}$ = ▲: 1.0 w/w%, ■: 2.0 w/w%, ▼: 3.0 w/w%, and ◆: 4.0 w/w%), and (f) magnified view at $50 < x_n < 65$ mm corresponding to the region enclosed in a black dashed square in (e). Dotted horizontal line in (a)-(d) and dotted vertical lines in (e) and (f) indicate the interface between the upper and lower gel layers.

3.3.4 Numerical simulation under spatially modulated K_2

To gain insight of the reason for the formation of above locally exceptional LPs in the bi-layered gels, I performed RD simulation based on the same method using in Sec. 3.3.2, but K_2 was spatially modulated at 40 mm from the reservoir boundary to reproduce the K_2 condition in the bi-layered gel. Figure 3.10a-c shows the output images of P distribution when K_2 was modulated at x = 40 mm between fixed $K_2^{\text{upper}} = 3.7 \times 10^{-3}$ M and $K_2^{\text{lower}} = 3.2 \times 10^{-3}$ M, 2.7×10^{-3} M, and 2.2×10^{-3} M, respectively. Based on the image analysis for them, the variation of Δx_n for each modulated condition is shown in Figure 3.10d and e. As mentioned above, under the condition of spatially fixed K_2 (Figure 3.10d●), Δx_n increases monotonically because this condition corresponds to the condition of mono-layered gel as discussion in Sec. 3.3.2. On the other hand, under the condition

of spatially modulated K_2, Δx_n changes dramatically after crossing the K_2 boundary (Figure 3.10d▲-▼). To discuss these changes in more detail, a magnified view around the K_2 boundary is shown in Figure 3.10e. For $K_2^{lower} = 3.2\times10^{-3}$ M, Δx_n approaches a constant value after crossing (Figure 3.10e▲), whereas for $K_2^{lower} = 2.2\times10^{-3}$ M, Δx_n decreases dramatically (Figure 3.10e▼). These results showed that as the gap of K_2 modulation ΔK_2 (= $|K_2^{upper}-K_2^{lower}|$) increases, the regular-type LP transitions to equidistant and revert type LP around the boundary. Therefore, the trend in the Δx_n-x_n plots for spatial modulation of K_2 was consistent with that observed in the experimental Δx_n-x_n plots for bi-layered gels.

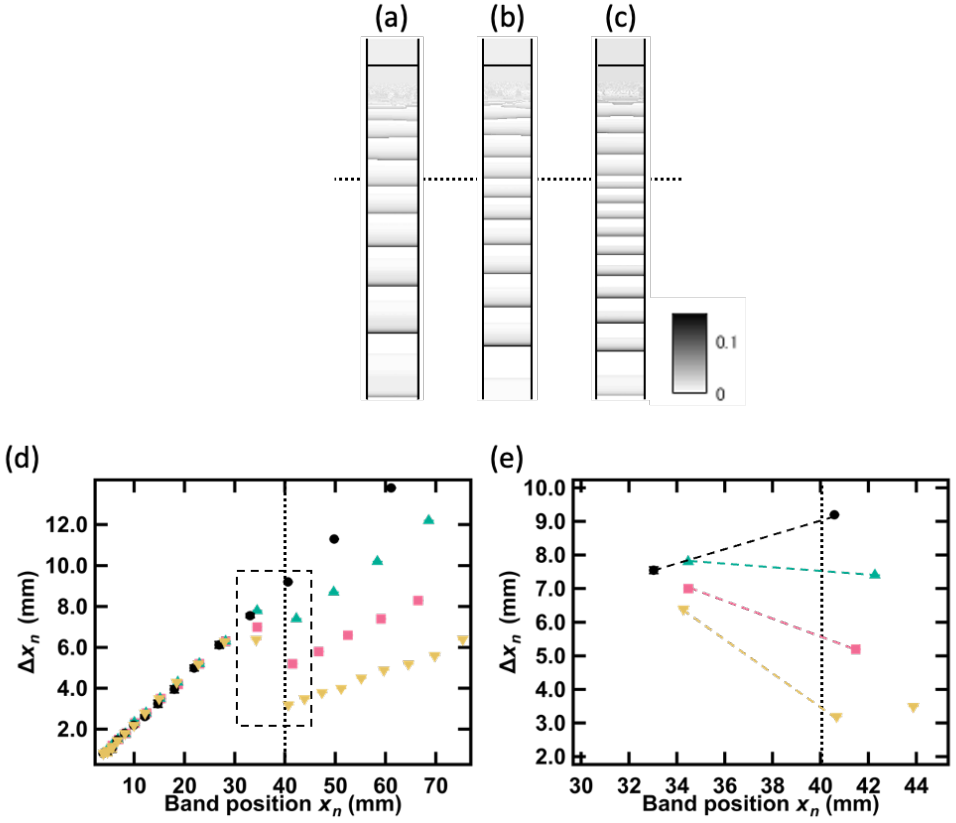

Figure 3.10. Output images of P distribution obtained from simulations with spatially modulated K_2, where the solid horizontal black line in the column represents the boundary of the reservoir, and the dotted line indicates the boundary of K_2 modulation. K_2 was modulated at x = 40 mm between $K_2^{upper} = 3.7 \times 10^{-3}$ M (fixed) and (a) $K_2^{lower} = 3.2 \times 10^{-3}$ M, 2.7×10^{-3} M, and 2.2×10^{-3} M. (d) Changes in Δx_n as a function of x_n (●: fixed $K_2 = 3.7 \times 10^{-3}$ M, modulated K_2 between $K_2^{upper} = 3.7 \times 10^{-3}$ M and K_2^{lower} = ▲: 3.2×10^{-3} M, ■: 2.7×10^{-3} M, and ▼: 2.2×10^{-3} M), and (e) magnified view at $30 < x_n < 45$ mm, corresponding to the region marked by a dashed rectangle in (d). The dotted vertical lines in (d) and (e) represent the boundary of K_2 modulation.

However, there was a slight difference between the experiment and the simulation in terms of responsiveness to such modulation. Although the earlier change in Δx_n depending on the K_2 modulation was observed from a point behind the gel interface in the experiment, the simulation results showed the change only after crossing the K_2 boundary. This discrepancy can be attributed to following two main factors. (i) The first is the melting and elution of the lower gel layer due to the pouring of hot sol (ca. 90 °C) on the top of the solidified lower gel (melting temperature of agarose = ca. 85 °C[142-143]). In this experiment, $[\text{agarose}]_{\text{lower}} > [\text{agarose}]_{\text{upper}}$, suggesting that a local gradient of gel concentration might have formed from the gel-gel interface towards the newly stacked upper gel (Figure 3.11a). Namely, it was possible that K_2 started to change behind the boundary (on the upper gel side), rather than rapidly changing at just the boundary (Figure 3.11b). (ii) The second factor is the change in diffusion rate of Cu^{2+} due to the change in gel concentration. In this study, an agarose gel was used as the reaction medium. Agarose reagents are composed mainly of non-ionic monosaccharides and contain small amounts of ionic agaropectin.[144] The agarose used in this experiment also contained small amounts of agaropectin, whether purified or not. The structure of agaropectin is similar to agarose, but it contains sulphate, methoxy, pyruvate and carboxyl groups. Therefore, these anionic functional groups were expected to affect the diffusion of Cu^{2+} through electrostatic interactions. Indeed, it was reported that the diffusion rate of Cu^{2+} is decelerated by agaropectin due to decreasing the diffusion coefficient (D).[145] Therefore, in this study, D was assumed to be uniform in space, independent of the number of gel layers, however, in fact it may have changed in conjunction with the modulation of the gel concentration. It is noted that the size of the 3D network of the gel structure, estimated to be 200-500 nm in the concentration range of the agarose used in this study,[134] is considerably larger than the size of the ions, the gel structure is unlikely to affect the diffusion rate. Therefore, we then performed some experiments and simulations considering the above factors as below.

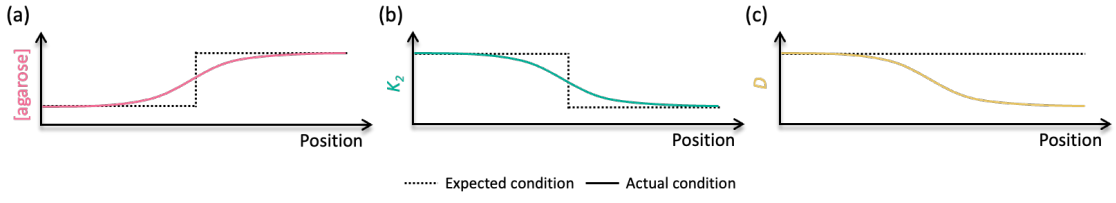

Figure 3.11. Difference between expected (dotted line) and actual (solid line) conditions for (a) agarose concentration, (b) nucleation threshold, and (c) diffusion coefficient.

3.3.5 Elution of a lower agarose gel layer

To investigate the elution of the gel from the lower layer, the profile of the gel concentration in the prepared multi-layered gel was measured. The prepared gel is shown as Figure 3.12a, which was made following the procedures described in Sec. 3.2.4. The concentration of agarose was 0.25 w/w% from the top of the gel up to 20 mm, after which the concentration was increased at 10 mm intervals to 1.0, 2.0, 3.0, and 4.0 w/w%. After the topmost gel layer had completely gelled, the gels were cut out at 2 mm intervals (0.35 mL/piece) from the top and the weight of each gel piece obtained was measured. Subsequently, these pieces were freeze-dried until they are completely dry. Then, I measured the weight of obtained dried pieces, where this weight corresponds to the weight of agarose polymer contained in a fixed volume of hydrogel fragments. Thus, the concentration of agarose in the gel pieces obtained was calculated from the weights before and after freeze-drying. From this calculation, the concentration profile was obtained shown in Figure 3.12b. As a result, a gradual local gradient of gel concentration over 2-3 mm was formed behind each gel-gel interface, indicating that a lower gel layer (higher concentration) was melted and eluted toward an upper layer by pouring the hot sol on a lower one. Therefore, when the gels were stacked using the above method, it was found that the K_2 change did not occur just at the interface as in the simulation, but in fact was induced from behind the interface (Figure 3.11b, green line) due to the gradual change in gel concentration shown by the pink line in Figure 3.11a.

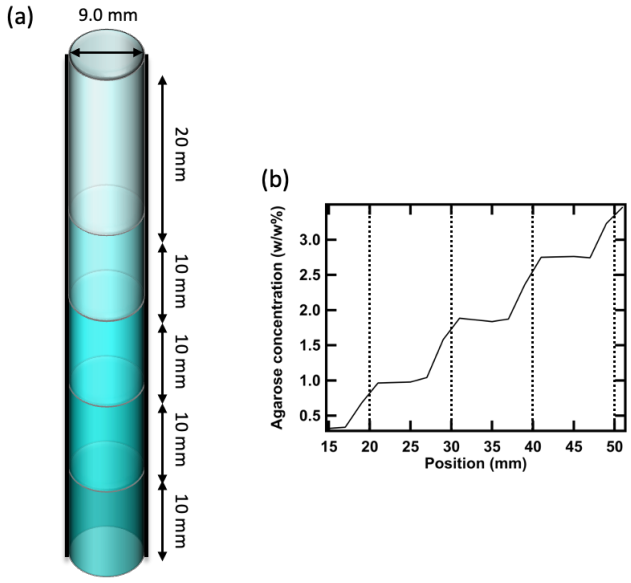

Figure 3.12. (a) Prepared multi-layered agarose gel without K_2CrO_4 for demonstrating the elution of lower agarose gels. The gel was made with reference to Sec. 3.2.4. (b) Concentration profile of agarose measured by weight difference before and after freeze-drying. The dotted lines show the gel-gel interfaces.

Furthermore, I investigated a dependence of this elution on Δ[agarose] (Figure 3.13). Experiment was carried out using the bi-layered gel under fixed $[agarose]_{upper}$ = 0.25 w/w% and variable $[agarose]_{lower}$ from 1.0 to 4.0 w/w%. With increasing $[agarose]_{lower}$, i.e. Δ[agarose], the change in gel concentration became more rapid, however the elution position remained within a range of about 3-4 mm from the gel-gel- interface independent of concentration. Therefore, the modulation of K_2 by the elution of agarose was found to be limited in extent regardless of $[agarose]_{lower}$.

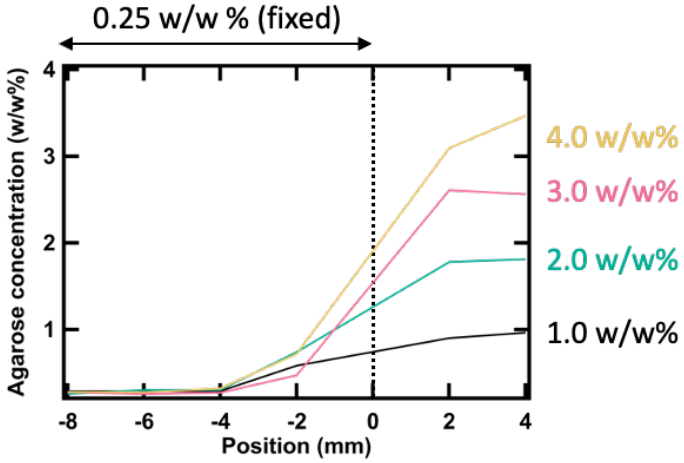

Figure 3.13. Effect of dissolution on the increase of Δ[agarose] with increasing $[agarose]_{lower}$. The concentration of upper gel was fixed at 0.25 w/w%. The position "0" means the gel-gel interface.

3.3.6 Effect of modulating diffusion rate

Then, I investigated the effect of another factor, diffusion rate, based on RD simulation. The previous study reported that the value of D was reduced to 60% as in previous results when the concentration of agarose was varied from 0.25 to 4.0 w/w%.[145] Therefore, I performed the RD simulations under two conditions: modulation of K_2 only (Figure 5a●) and modulation of K_2 with changes in $D_{A\text{-}C}$ (Figure 5a▲). In both cases, although there is perfect agreement of Δx_n-x_n plots behind the modulation boundary, Δx_n show an earlier decrease just before the boundary only when both K_2 and $D_{A\text{-}C}$ were modulated (green ▲ at approximately x_n = 37 mm n Figure 3.14a). This result was clearly in agreement with the experimental results of the bi-layered gels, showing earlier Δx_n change behind of the gel-gel interface (Figure 3.9). Thus, the change of D with the modulation of gel concentration was found to be one of the reasonable parameters to explain the experimental results. Why the modulation of the diffusion rate is responsible for the change in the periodicity of the pattern is discussed by using the results of the evolution

of the diffusion front of A (Cu^{2+}) and the reaction front of C ($CuCrO_4$ molecules) (Figure 3.14b and c). The evolution of the diffusion front (solid line) slows down after crossing the modulation boundary (x = 40 mm) and the evolution of the reaction front slows down behind the boundary when $D_{A\text{-}C}$ is varied, where the position of the difference with and without consideration of D change is indicated by a black arrow.

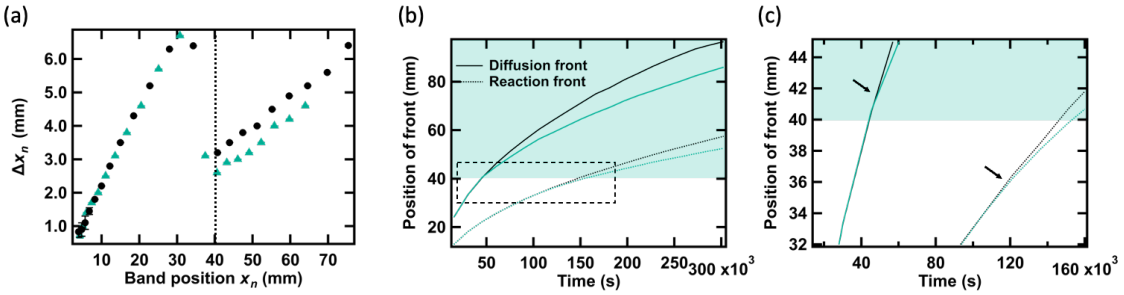

Figure 3.14. (a) Relationship between Δx_n and x_n in simulations under K_2 modulation with and without varying $D_{A\text{-}C}$ (●: only K_2 modulation, ▲: K_2 modulation with varying $D_{A\text{-}C}$). In both simulations, at x = 40 mm, K_2 was varied from K_2^{upper} = 3.7×10^{-3} to K_2^{lower} = 2.2×10^{-3} M and $D_{A\text{-}C}$ from 1.0×10^{-5} to 0.6×10-5 cm^2s^{-1}. The dotted line indicates the boundary of the K_2 and $D_{A\text{-}C}$ modulations. (b) The position of the diffusion front of A (solid line) and the reaction front of C (dotted line) as a function of time (green line: only K_2 modulation, black line: K_2 modulation and $D_{A\text{-}C}$ change). (c) Magnified view of (b) from the black dashed rectangle in (a). The pale red area shows the K_2^{lower} region.

These results can be attributed to the fact that the deceleration of the diffusion front after crossing the modulation boundary propagates to the dynamics of the reaction front behind the boundary. Namely, the modulation of the diffusion rate induces a modulation of the dynamics of the backward reaction process, which may have resulted in the early Δx_n transition. Thus, the early transitions observed in the bi-layered gel experiments were caused by a combination of factors (i) changes in K_2 due to gel elution and (ii) changes in diffusion rate. As one demonstration to support this consideration, we have investigated the Δx_n transition behavior with respect to the position of the gel-gel interface. In a typical bi-layered gel experiment, the gel-gel interface was fixed at x = 60 mm. As a result, the earlier Δx_n transition before the gel-gel interface occurred at approximately the same position for all conditions (Figure 3.9). However, this position starting the earlier change recedes towards the interface between the aqueous solution and the upper gel as the gel-gel interface approaches the solution-gel interface (Figure 3.15). Furthermore, at a position much closer to the gel interface, the coexistence of periodicity due to the overlap of the initial transitions disappears in the bi-layered gel. Therefore, it is important to consider the position of the gel interface (especially the "first gel-gel interface"). However, it is noted that these factors do not inherently affect the geometrical transition behavior

from the regular- to revert-types of LPs.

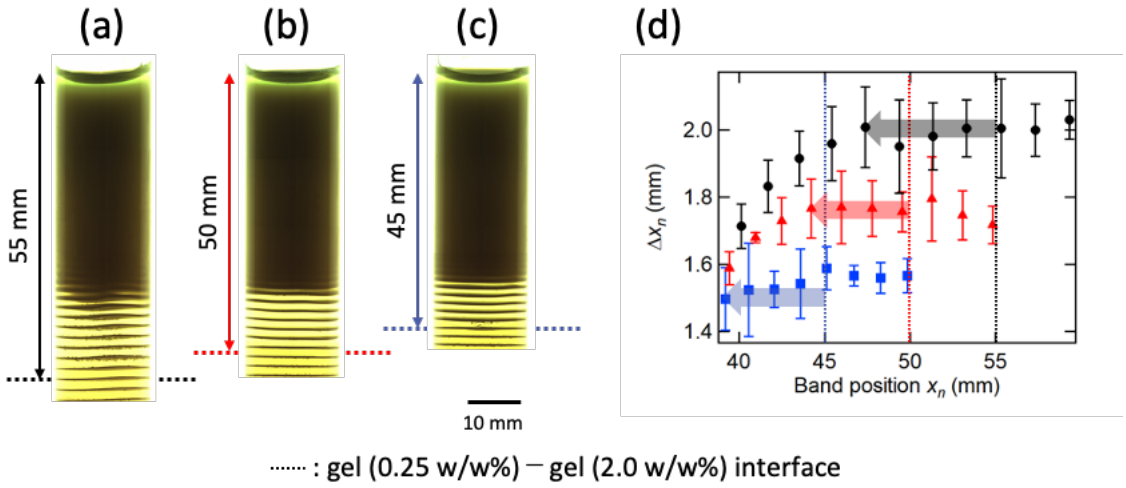

Figure 3.15. Partial images of pattern formation in bi-layered gels constructed using agarose gels (0.25 w/w% upper and 2.0 w/w% lower) with different gel-gel interface positions: (a) x = 55 mm, (b) x = 50 mm, and (c) x = 45 mm. (d) Relationships between Δx_n and x_n (●: (a), ▲: (b), and ■: (c)). The dotted lines in the pictures and the plot indicate the gel-gel interface, and each horizontal pale arrow indicates the gap to the starting position of the Δx_n transition.

3.3.7 Pattern formation in bi-layered gels with increasing K_2

Since the focus of this work has been on the mechanism for the transition from regular-type to revert-type, namely the decrease in Δx_n, the spatial decrease in K_2 has been discussed in detail so far. In order to prove the universality of the effect of K_2 modulation on the pattern, in this section we have experimented with deceasing agarose concentration (increasing K_2) rather than decreasing agarose concentration in a bi-layered gel system as shown in Figure 3.9 (Figure 3.16). In this case, it was predicted that different from the decreasing K_2 situation, the value of Δx_n increased dramatically close to and after crossing the gel-gel interface. Actually, Δx_n increases dramatically compared with the 4.0 w/w% mono-layered gel for all bi-layered gels (Figure 3.16e). Furthermore, the rate of increase in Δx_n enhanced as Δ[agarose] increased. Thus, the effect of increasing K_2 is in contrast to that of decreasing K_2, suggesting that the coexistence of these two effects results in the complex rock pattern periodicities introduced in Sec. 3.1.

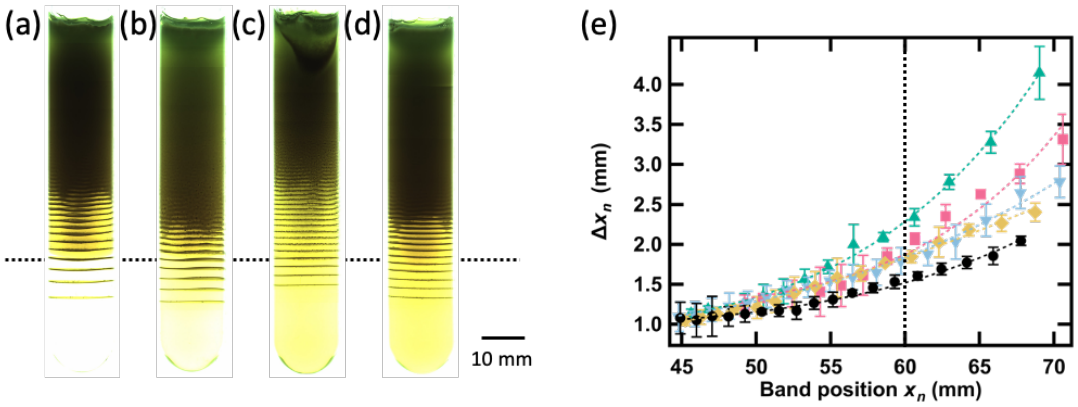

Figure 3.16. Pattern formation in bi-layered agarose gels constructed with a 4.0 w/w% upper agarose gel and (a) 0.25 w/w%, (b) 1.0 w/w%, (c) 2.0 w/w%, or (d) 3.0 w/w% lower agarose gel. (e) Relationship Δx_n and x_n (●: fixed [agarose] = 4.0 w/w% (mono-layered gel), $[\text{agarose}]_{\text{lower}}$ = ▲: 0.25 w/w%, ■: 1.0 w/w%, ▼: 2.0 w/w%, and ◆: 3.0 w/w%). Dotted horizontal line in (a)-(d) and dotted vertical lines in (e) indicate the gel-gel interface.

3.3.8 Pattern formation in multi-layered gels

From the previous results and discussion, it was found that Δ[agarose] is the important factor controlling the periodicity of the LP. However, in the bi-layered gel experiments, the modulation of the agarose concentration was only within a local area, so that such periodicity transitions were only observed in a limited area. On the other hand, the exceptional LPs observed in other reaction systems, such as those described in Sec. 3.1, show a characteristic periodicity throughout the system. Therefore, to reproduce such complete exceptional LPs, it was necessary to modulate the agarose concentration throughout the system. To demonstrate it, I preparade two types of multi-layered gels with different distribution of agarose concentrations: (i) multi-layered gels with stepwise decreasing [agarose] at whole region of reaction medium (Figure 3.17a), and (ii) with repeated high and low agarose concentrations (Figure 3.17b). In type (i), Δx_n was almost constant at 1.5 mm throughout the whole formed pattern, indicating that the complete equidistant-type LP was successfully formed (Figure 3.17a). This result was consistent with the previous simulation study that proposed decreasing K_2 led to form exceptional LPs.[102] Therefore, I provide the first experimental evidence that LP geometrical transition phenomena are governed by the control parameters of the nucleation rate in the nucleation-based scenario. Furthermore, in type (ii), a complex change in Δx_n was observed (Figure 3.17b). At the early bands from near the solution-gel interface, Δx_n increases rapidly and reaches a maximum value at x_n = 44mm. Then it decreases and approaches a minimum constant value until x_n = 57mm. This is because the agarose

concentration increased with respect to x = 50 mm from 0.25 to 4.0 w/w%. Thereafter, Δx_n increases again and reaches a maximum value at x_n = 71 mm due to the decrease in agarose concentration. Finally, Δx_n decreases dramatically after entering the region of 4.0 w/w% agarose concentration. Such oscillation of Δx_n is due to repeating stepwise increase and decrease in agarose concentration. Thus, the two periodicities coexist with the regular- and revert-types in type (ii) multi-layered gel. Although this is not the case in previously reported LPs with monotonic periodicity, analogical patterns in nature frequent shows such complex periodicities. Therefore, it is clear that tuning of spatial K_2 distribution due to such modulation of gel concentration decide the destiny of transition behavior and complexity of LP periodicities.

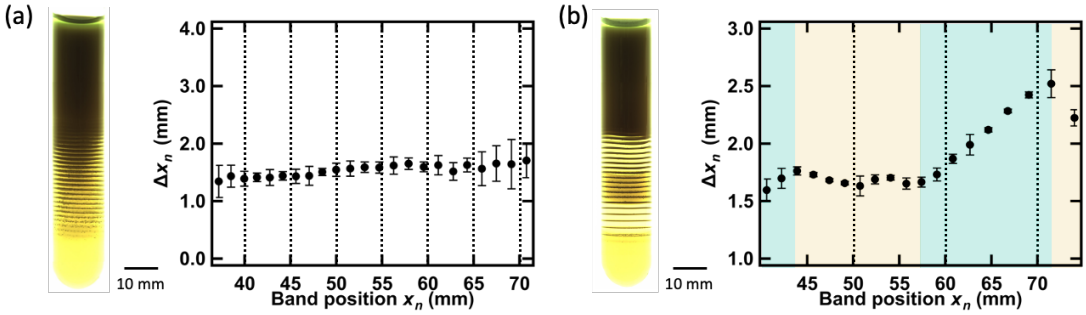

Figure 3.17. Pattern formation in multi-layered agarose gels (left) and the relationship between Δx_n and x_n (right). (a) Type (i) with stepwise decreasing agarose concentration ([agarose] changed from 0.25 to 4.0 w/w% from x = 40 mm to 75 mm). (b) Type (ii) with repeated increasing and decreasing agarose concentrations ([agarose] changed to 0.25 or 4.0 w/w% repeatedly at x = 50, 60, and 70 mm). Dotted lines indicate the interfaces of the agarose gels. The pale green and yellow regions in (b) represent the regions with increased and decreased Δx_n,.

3.4 Conclusions

The nucleation-based scenario has been widely used to understand the mechanisms of LP formation, and considerations based on this scenario provide us with fundamental insights into the question of Liesegang phenomena. However, the geometrical transition of LP was one of the unresolved issues in the nucleation-based scenario. In this study, we focused on nucleation, the most important process determining the periodicity in this scenario, and found that the control of the spatial distribution of K_2, the control parameter of the nucleation kinetics, controls the transition behavior of the LP. This control was demonstrated by using bi-layered or multi-layered gels made by layering gels of different concentrations. From the bi-layered gel experiments, only in the region where there was a local modulation of K_2 due to the concentration gradient of the gel show characteristic changes in Δx_n, and the intensity of this change depends on ΔK_2. Furthermore, the complete exceptional type of LP was formed over the whole reaction space in the case of multi-layered gels where the K_2 modulation region can be extended over the whole area. In addition, in contrast to the simple increase or decrease of K_2, complex changes in the spatial distribution of K_2 led to the formation of the complex periodicity that followed this K_2 changes. Therefore, it is suggested that the spatial modulation of the nucleation rate needs to be incorporated into the mathematical model when discussing pattern transitions using the nucleation-based scenario, which would make this scenario the most practical model for understanding LP formation mechanisms arising from thermodynamic metastable states.

Chapter 4 Phase Separation Mechanism Driven by the pH-Induced Aggregation of Gold Nanoparticles

4.1 Introduction

As introduced in Sec. 1.7.3, most of experimental reaction systems for studying Liesegang phenomenon so far (such as salt formation reactions[57-58, 63, 66, 68-69, 71, 78, 86-89] and nanoparticle formation by chemical reduction reactions[59-60, 82, 100]) included the nucleation process while solid-phase transition processes. In such systems, the nucleation dominates the pattern formation mechanism. The nucleation-based scenario is therefore universal and practical for discussing the obtained results of such classical Liesegang systems such as those described above. However, it has not yet achieved a reasonable explanation for the formation mechanisms of helix formation, tree-like structures, and spot structures, which are known to be specific morphological changes in the Liesegang phenomenon introduced in Sec. 1.6.2, by using this scenario. Furthermore, one of the main targets of modelling via the Liesegang phenomenon, geoscientific patterns (e.g. stripe formation in agate rocks,[110-111] oscillatory zoning on magma crystallization,[146-147] and the orbits in the solar system[113]), has traditionally been suggested to be driven by phase separation-like mechanism rather than nucleation.[130-131, 148] It is therefore essential to validate the phase separation-based scenario by experimental and mathematical modelling in order to consider their practicality for these special classes of Liesegang phenomena. As mentioned in Sec. 1.7.3, various studies on mathematical modelling have been carried out using a combination of the Cahn-Hilliard (CH) equation and RD equation.[116-117, 129] Common to all these studies is that patterns are formed by phase separation due to spinodal decomposition, which occurs when the concentration of precipitating precursors increases due to salt formation reactions or external chemical or physical perturbations and reaches a thermodynamically unstable state. (Fig.1.1.8b and 1.22). Actually, these simulation results showed LP can be formed and indicates good agreement with LP characters such as the spacing law (Figure 1.2.3). Therefore, there is some progress in the understanding of the phase separation-based scenario at the numerical simulation study. On the other hand, most of the experimental systems in previous studies to test the consistency of this mathematical model were based on salt formation reactions.[86, 124-125] In these reports, phase separation was assumed to occur when C is formed by the salt formation reaction reached a certain threshold. However, the consistency of this assumption is very ambiguous, because such a reaction system

should be dominated by nucleation under some conditions as discussed in chapters 2 and 3 so far. Therefore, experimental validation using this system is not suitable for understanding the essence of the phase separation-based scenario, because such systems potentially involve the effects of nucleation.

Therefore, it is important to select an aggregation/precipitation system that exhibits aggregation and phase separation behavior with zero interparticle energy based on DLVO theory, as one indicator to search for an experimental system that faithfully reproduces the phase separation-based scenario (Sec. 1.7.2 Figure 1.21). As a candidate for such a reaction system, we have focused on the pH-induced aggregation of nanoparticles (NPs),[149-152] which has been frequently reported and occurred when surface modified metal NPs with a weakly acidic functional group (e.g. carboxylic acid) are exposed to an environment with below pK_a that derived from the functional group (Figure 4.1).

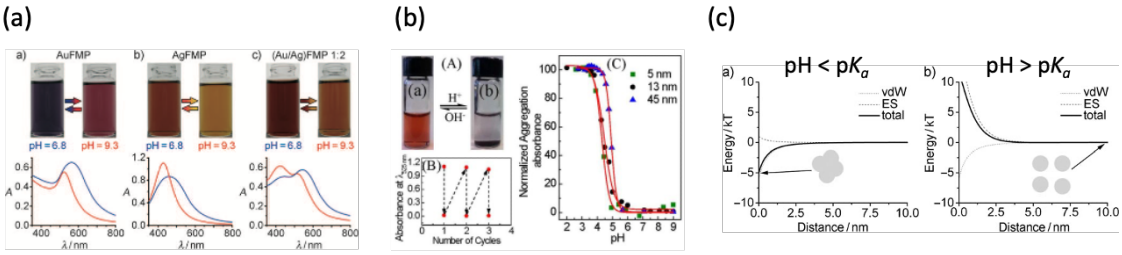

Figure 4.1. (a) Color variations of different types of surface modified NPs and UV-vis spectra corresponding to the below and above pK_a. (b) Color changes of MUA-Au NPs dispersion and oscllation of LSPR absorbance with periodc pH changes, and changes in absorvance for aggregation as a function of pH with different particle sizes, adopted from Ref. 152. (c) Caluculated DLVO potential for the surface modified NPs below and above pK_a. (a) and (c) were reprinted with permission from Ref. 151. Copyright 2010 John Wiley and Sons.

Since such surface-modified NPs have negative charged on itself surface under basic condition of a solution (higher pH) due to deprotonation of the acidic functional ligands, the electrostatic repulsion between particles is bigger and the DLVO energy barrier appears, thus NPs disperse in the solution. Therefore, this dispersed solution exhibits a color corresponding to the localized surface plasmon resonance (LSPR) of NPs (e.g. a bright red color in the case of typical Au NPs) (Figure 4.1a). On the other hand, when the solution becomes more acidic than the pK_a (lower pH), the surface ligands are protonated and the electrostatic repulsion that stabilizes the dispersion state is lost and the barrier disappears, resulting in aggregation of the particles and a corresponding color change in the solution (e.g. a dark purple in the case of typical Au NPs). Such dispersion/aggregation behavior is independent of the metal type and is determined by the pK_a of the surface ligand and the pH change of the solution (Figure 4.1a). As a candidate of ligand, we focused on 11-mercaptoundecanoic acid (MUA), which is a

typical carboxylic acid surface modifier for gold NPs (Au NPs).[153-155] Figure 4.1b shows a typical color changes of a solution and optical properties of synthesized surface modified Au NPs with MUA molecules (MUA-Au NPs) between a dispersion and an aggregation states depending on pH values.[152] In addition to the above experimental insights, such pH-induced aggregation has also been well discussed by calculations using DLVO theory.[151] Indeed, Figure 4.1c shows, the aggregation state results from the loss of the energy barrier for pH < pK_a (Figure 4.1b left), whereas for pH > pK_a, the dispersion state is stabilized (Figure 4.1b right), which is providing theoretical support for the above experimental considerations. Hence, the pH-induced aggregation can give rise to spontaneous precipitation predicted by the DLVO theory as introduced in Sec. 1.7.3, excluding nucleation. Namely pattern formation in the phase separation-based scenario can be caused by this principle, which is another scenario different from the nucleation-based scenario bifurcated by the thermodynamic stability of the system. Thus, the pH-induced aggregation is completely different from conventional salt formation reaction systems and is one of the most suitable reaction systems to experimentally explore the intrinsic influence of processes other than nucleation.

In this chapter, instead of the salt formation reaction system to demonstrate the nucleation-based scenario, we aimed to construct an experimental system that faithfully reproduces the phase separation-based scenario by combining the pH-induced aggregation of MUA-Au NPs with the experimental setup of the Liesegang phenomenon, where hydrochloric acid and MUA-Au NPs were used as the invading (outer) and pre-doped (inner) electrolytes, respectively. Furthermore, the practicality of the phase separation-based scenario, which has not been achieved so far, is experimentally verified by investigating the concentration dependence of the invading and pre-doped electrolytes and the pattern formation dynamics in detail using the constructed experimental system. In addition, the validity of the experimental results through a mathematical approach was verified by operating the RD equation incorporating the CH equation for the obtained experimental results.

4.2 Experiments

4.2.1 Reagents and instruments

Hydrogen tetrachloroaurate (III) tetrahydrate ($HAuCl_4$•$4H_2O$, 99.0%), trisodium citrate dihydrate ($C_6H_5Na_3O_7$•$3H_2O$, Cit), 0.01 M sodium hydroxide solution (NaOH, factor (20 °C) = 1.0), agarose (fine powder) as a gel medium, and bromo thymol blue solution (BTB, 0.04 w/v%) were purchased from FUJIFILM Wako Pure Chemical Industry (Japan). 11-Mercaptoundecanoic acid (MUA, 95%) was purchased from Sigma-Aldrich (USA). Hydrochloric acid (HCl, 35%) was purchased from Nacalai Tesque Industry (Japan). All reagents were used without further purification. Ultraviolet-visible (UV-vis) and Fourier transform-infrared spectrometer (FT-IR), Transmission electron microscopy (TEM), and Dynamic light scattering (DLS) measurements were performed using a JASCO V630, a Thermo Fisher Scientific Nicolet 6700, a JEOL JEM-2100F at 200 kV, and an Otsuka electronics ELS-Z2M. The pH measurement was performed by using a pH meter (HORIBA F-51) with a pH electrode (HORIBA 9618S-10D). Optical microscopy and microspectrophotometry (MSP) measurements are carried out using an OLYMPUS BX-51 and a HAMAMATSU PMA-12. All pattern formation experiments were performed in glass test tubes (∅ = 10 mm). The formed patterns were observed using the same microscope as the above. Image analysis such as a line profiling and making grayscale images was performed using Image J software.

4.2.2 Synthesis of MUA-Au NPs[156]

$HAuCl_4$ aq. soln. (250 mM, 400 μL) was added to ultra-purified water (99.6 mL) that is beforehand boiled by heating at 250 °C with stirring at 600 rpm. Immediately after it, Cit aq. soln, (38.8 mM, 10 mL) was added to the above $HAuCl_4$ solution and kept heating and stirring for 5 min. Subsequently, heating was stopped, and only stirring was kept for 60 min at room temperature. This mixture was then centrifugated at 15000 rpm for 30 min and redispersed by ultra-purified water. In the previous processes, dispersion of Au NPs stable by Cit (Cit-Au NPs) was prepared. Also, we prepared a NaOH aq. soln. (0.20 M, 10 mL) with dissolving MUA (moral ratio; added $HAuCl_4$:MUA = 1:5) by heating at 40 °C with stirring at 600 rpm for 30 min, where MUA was neutralized (deprotonated) at this basic condition. Subsequently, this basic MUA solution was added to the Cit-Au NPs dispersion with stirring at 300 rpm and keeping stirring at 25 °C at least 12 h to modify the surface of Cit-Au NPs with MUA molecules (Figure 4.2). After the modification, this mixture was centrifugated at 15000 rpm for 30 min and redispersed by ultra-purified water. The centrifugation was then repeated with the same condition and redispersed by ultra-

purified water (1-2 mL). This obtained MUA-Au NPs dispersion was stored at 5 °C. Also, we used up this dispersion within a week to keep it fresh.

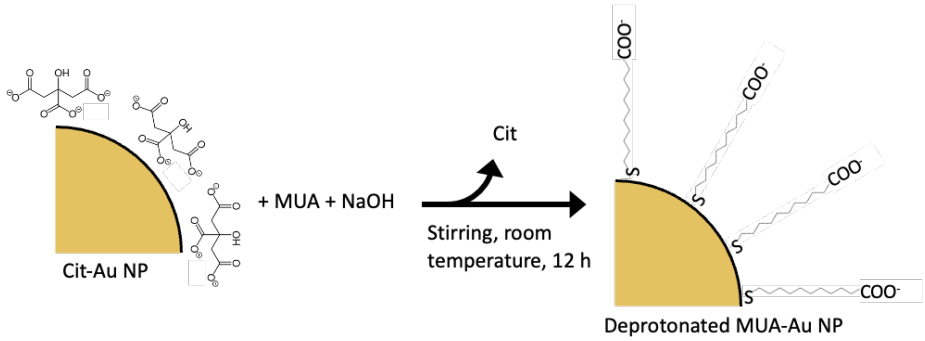

Figure 4.2. Scheme of synthesis of MUA-Au NPs.

4.2.3 UV-vis and FT-IR measurements

To evaluate the synthesis and modification of Cit- and MUA-Au NPs, I performed UV-vis measurement. I used Cit-Au NPs after purification by the centrifugation processes. Also, MUA-Au NPs after the set of centrifugations and redispersion process was used. The concentration of dispersion was decided by an extinction intensity of LSPR peak around 520-530 nm of MUA-Au NPs.[157] In briefly, the concentration was calculated by the following relationships:

$$ln\varepsilon = klnD + \alpha \quad (47)$$

$$Extinction\ intenisty = \varepsilon lC \quad (48)$$

where ε, D, l, and C are the extinction coefficient in $M^{-1}cm^{-1}$, the core diameter of the nanoparticles in nm the optical path length in cm, and the concentration in M. Also, k and α is the coefficient obtained by the fitting to eq. (47). In this study, we used the value set obtained in the previous study.[157] Furthermore, I also performed FT-IR measurement to evaluate the modification by MUA molecules and deprotonated in the basic condition. The purified Cit-Au NPs and MUA-Au NPs were used, in which the former one was vacuum dried, while the letter one was reprecipitated by EtOH and then vacuum dried. After the characterization of the synthesized particles is complete, we investigated the behavior of pH-induced aggregation of MUA-Au NPs in an agarose gel (0.20 w/v%) by UV-vis measurement. At first, an agarose powder was roughly dissolved in ultra-purified water by heating in a microwave oven, and then it was heated on a hot stirrer at 90 °C with stirring at 150 rpm to complete dissolving. After that, the concentrated MUA-Au NPs dispersion was added to this hot sol to be the final concentration of MUA-Au NPs 2.0 nM. This mixture was cooled at room temperature and the crude heat was removed.

Just before gelation, this mixture was poured into the measurement cell (10×10 mm) and mixed with a prescribed concentration of HCl to prepare MUA-Au NPs-doped gels under different pH conditions. These samples were gelation at 18 °C for 30 min. Then, we performed UV-vis measurement.

4.2.4 TEM observation

We used the purified Cit-Au NPs and MUA-Au NPs for TEM measurement. To prepare the samples for TEM measurement, 10 μL of dispersion was doped on a grid (Okenshoji, ELS-C-10) and dried at room temperature.

4.2.5 pH titration[158]

The pH titration was performed to investigate pK_a of the synthesized MUA-Au NPs. Before, the titration, I prepared the mixture of MUA-Au NPs and NaOH with a total volume of 10 mL, in which the final concentrations of MUA-Au NPs and NaOH were 1.0 nM and 1.0×10^{-2} M. For the titration, HCl aq. soln. (10 mM) was used. The titration was performed at room temperature with an *in-situ* pH measurement. The pH value was read after stirring for 5 min for each drop of HCl solution to allow sufficient time for each chemical process to reach the equilibrium state.

4.2.6 DLS measurement

To investigate the aggregation kinetics of MUA-Au NPs, I carried out DLS measurement. There were two ways to measure it. At first, to obtain simple information on aggregation responsiveness to pH, I prepared a mixture of MUA-Au NPs (fixed 2.0 nM) with HCl (prescribed concertation) and measured a hydrodynamic radius against different pH values by DLS measurement 180 min after mixing of MUA-Au NPs and HCl. On the other hand, to obtain detailed information on aggregation kinetics, I performed DLS and pH measurements of change over time. The mixed solutions ([MUA-Au NPs] = 1.0 nM and [HCl] = 1.0×10^{-4}, 2.0×10^{-4}, and 1.0×10^{-3} M) were used for this measurement. All procedure in this section was performed at room temperature.

4.2.7 Patten formation by pH-induced aggregation of MUA-Au NPs

The NaOH solution (1.0×10^{-4} M) was mixed with MUA-Au NPs dispersion to be total volume 10 mL and the concentration of MUA-Au NPs became desired values. Subsequently, the agarose powder was added to this mixed solution at 0.20 w/v% and

heated in a microwave oven to dissolve it. The solution was then immediately heated at 90 °C for 3 min with stirring at 150 rpm. Finally, heating with microwave oven again to dissolve agarose completely. This hot agarose sol was poured into a glass test tube to a height of 120 mm, and stood at 18 ± 0.5 °C for 3 h for complete gelation. Afterward, an HCl aq. soln. with prescribed concentration (1.0 – 1.75×10^{-4} M) was poured on the top of the gel (Figure 4.3). The H^+ invading into the gel with diffusion began immediately, and a pH gradient with a diffusion gradient of H^+ was formed. In all conditions of pattern formation, the system was kept in a thermostat at 18 ± 0.5 °C, and the duration of pattern formation was fixed at 2 weeks. After the pattern formation, the HCl solution was removed from the top of the gel. Then, the obtained sample was observed using microscopy measurement.

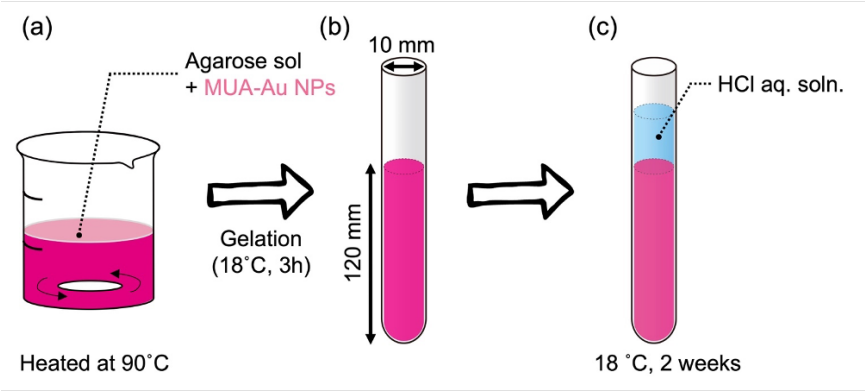

Figure 4.3. Illustration of experimental procedure of pattern formation in MUA-Au NPs aggregation system. (a) Preparation of agarose sol doped with MUA-Au NPs. (b) Making the agarose gel in a test tube. (c) Initiation of pattern formation by pouring HCl aq. soln. on the top of the gel.

4.2.8 Image analysis of obtained patterns

I carried out the line profile analysis of the obtained images of pattern formation. Before the profiling, original images were converted to grayscale images using the Image J software. Then, the line profile was carried out from an interface between the HCl reservoir and the gel. The result was output as a gray value for spatial coordinates toward the bottom of the gel. For our setting, the gray value was represented with a range from 0 to 255, where 0 and 255 corresponded to black (dark color in original images) and white (light color in original images). Then, I obtained the inverted gray value (IGV) by reversing this relationship using the following method.

$$IGV = 255 - gray\ value \qquad (49)$$

The higher value, the color of the analyzed area is close to black in IGV.

4.2.9 Visualization of H^+ diffusion front with BTB

Basically, the procedures of the gel preparation and the pattern formation were according to the description in Sec. 4.2.7. However, I added BTB solution instead of MUA-Au NPs solution to be the concentration 8.0×10^{-4} w/v%.

4.2.10 pH-induced aggregation of MUA-Au NPs in rectangular agarose gel

I made the rectangular mold by sandwiched a silicone rubber sheet that hollow out inside as rectangular-shaped with two glass plates. Based on the same procedure as described in Sec. 4.2.7, the gel pre-doped MUA-Au NPs was prepared in this mold. After the gelation, the pattern formation was carried out with the HCl diffusion. The obtained pattern was observed using the optical microscope equipped with a microspectrophotometer.

4.3 Results and discussion: Characterization of synthesized MUA-Au NPs

4.3.1 Evaluation of synthesis of MUA-Au NPs by UV-vis and FT-IR measurements

Figure 4.4a shows the result of UV-vis measurement for a pre-modification (Cit-Au NPs) and a post-modification (MUA-Au NPs) by deprotonated MUA molecules. The LSPR peak shifted from 518 nm to 528 nm after the modification. Since such red-shift was also observed in the previous study for the synthesis of MUA-Au NPs,[156] therefore, it was suggested that the modification was succeeded. Also, the FT-IR spectrum showed stronger evidence for the modification (Figure 4.4b). The blue region (i) and (ii) corresponds to the absorbance of S-H stretching and COOH stretching. Since the broad peak of absorbance disappeared in the region (i) through the modification, we found that the S-H bond was replaced by the Au-S bond. Furthermore, the strong sharp peak in region (ii) also disappeared after the modification, indicating that the COOH was deprotonated and formed COO^-. Therefore, it found that the synthesis of deprotonated MUA-Au NPs was succeeded from above the results of UV-vis and FT-IR measurements.

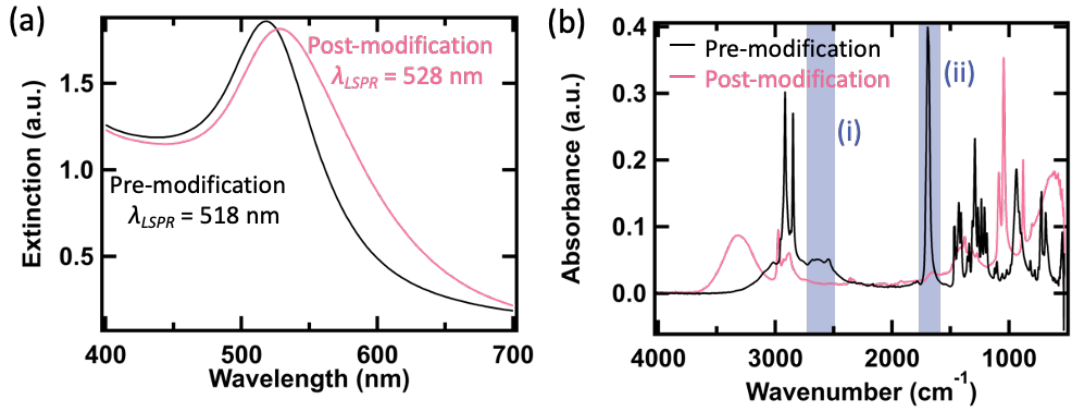

Figure 4.4. (a) UV-vis and (b) FT-IR spectra for the pre-modification NPs (synthesized Cit-Au NPs) and the post-modification MUA sodium.

4.3.2 Average size of synthesized NPs calculated by TEM observation

TEM observation was performed for Cit-Au NPs (Figure 4.5a) and MUA-Au NPs (Figure 4.5b). While the average size of Cit-Au NPs was 13 ± 3.6 nm, MUA-Au NPs was 15 ± 3.5 nm, where the average size was calculated from at least the particle number of 100. The size was almost unchanged before and after the modification.

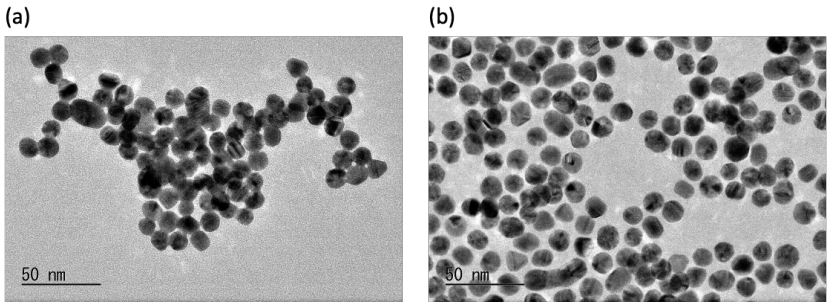

Figure 4.5. TEM micrographs of (a) Cit-Au NPs and (b) MUA-Au NPs. The average particle sizes of each NPs are 13 ± 3.6 nm (Cit-Au NPs) and 15 ± 3.5 nm (MUA-Au NPs).

4.3.3 Determining pK_a of MUA-Au NPs by pH titration

Figure 4.6a shows a titration curve of the full range of titration HCl volume. We can see the first plateau until around the $V_{titration}$ = 7500 µL, corresponding to the titration of excess hydroxide ions. Then, the second plateau appears between two broken lines in Figure 4.6b, resulting from the titration of carboxylates on the MUA-Au NPs surface and buffering by them. According to the previous study,[158] the pK_a of MUA molecules on the Au NPs surface was estimated from the pH halfway through the second plateau. To calculate this value quantitatively, Figure 4.6b was differentiated to obtain the exact area of the second plateau (Figure 4.6c). Thus, the pK_a of our synthesized MUA-Au NPs was 6.5. This value is close to the other study of synthesizing MUA-Au NPs.[159]

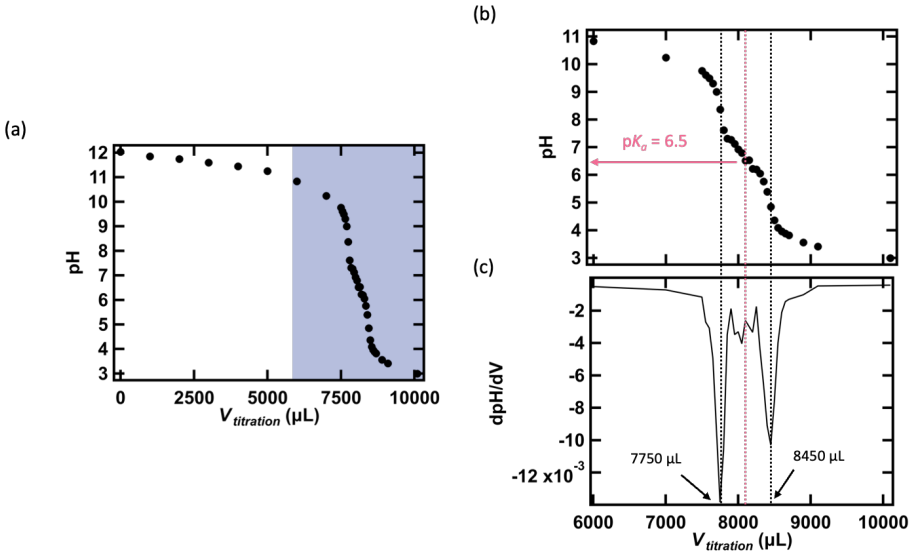

Figure 4.6. Experimental titration curve of the basic MUA-Au NPs solution ([MUA-Au NPs] = 1.0 nM, 10 mL) with the HCl solution ([HCl] = 1.0×10^{-2} M). (a) The range of all titration volume and (b) magnification of blue region in (a). (c) Differentiation result of (b)

4.3.4 Calculation of W_{tot} between synthesized MUA-Au NPs based on DLVO theory

Based on our previous results, we have successfully synthesized MUA-Au NPs and estimated their average particle size and pK_a. By applying these experimentally obtained values to equations (29)-(33), we have calculated the W_{tot} acting between the two MUA-Au NPs. The resulting value of the energy barrier allows us to estimate whether the synthesized NPs exhibit aggregation from a thermodynamically unstable state or not. In this calculation, the Hamaker constant (A) was 3.0×10^{-19} J that is the typical value of metal (Au, Ag, Cu);[127] [NaOH] (= [electrolyte] in eq. (33)) was 0.10 M. Assuming that the effect of pH on protonation/deprotonation was such that the surface potential is proportional to a present ratio of deprotonated MUA to protonated MUA molecules, the relationship is expressed by the following equation.

$$\psi_{pH} = \psi_0 \times \frac{\Gamma_{MUA^+}}{\Gamma_{MUA}} \qquad (50)$$

where ψ_{pH} and fraction about Γ represent the pH-dependent surface potential of MUA and the present ratio of deprotonated to protonated MUA. Also, this fraction was estimated referring previous studies.[151, 160]

$$\frac{\Gamma_{MUA^+}}{\Gamma_{MUA}} = \frac{1}{1+10^{pKa-pH}} \qquad (51)$$

Figure 4.7a shows the ratio of deprotonated MUA dramatically decreases around pK_a with increasing pH. Furthermore, Figure 4.7b shows that the energy barrier presenting at pH = 8 and 10 is reduced to zero below pH 7 (≒ pK_a). Namely, the synthesized MUA-Au NPs were found to exhibit pH-induced aggregation from an unstable thermodynamic state without nucleation, as in the previous study presented in Sec. 4.1.

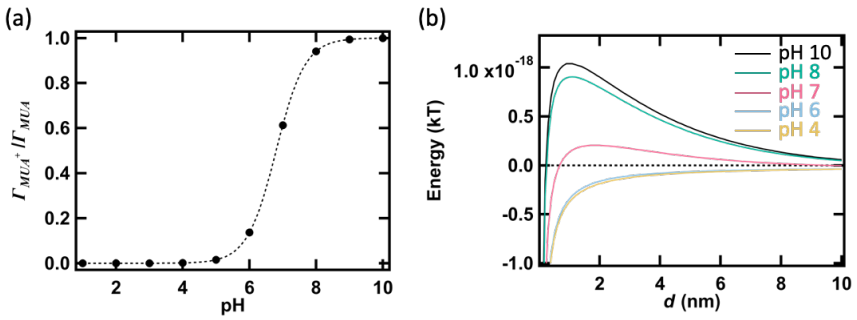

Figure 4.7. (a) Estimation of $\Gamma_{MUA+}/\Gamma_{MUA}$ by eq. (51) and pK_a = 6.5. (b) Calculation of W_{tot} from eqs. (29)-(33) and (50) ($A = 3.0\times10^{-19}$ J, $d = 1.5\times10^{-8}$ m, $\varepsilon = 6.9\times10^{-10}$, ψ_0 = -200 mV).

4.3.5 Evaluation of pH-induced aggregation dynamics by DLS measurements

Various early measurements and calculations have been carried out to characterize the synthesized MUA-Au NPs and to estimate their aggregation ability. Then, I tried to evaluation an aggregation dynamics of them by DLS measurements. Figure 4.8 shows a relationship between hydrodynamic radius and pH values 180 min after mixing MUA-Au NPs and HCl. The radius began increasing slightly below pK_a 6.5 but increased dramatically below pH 4. Therefore, it was found that a fast pH-induced aggregation occurred around pH 4.

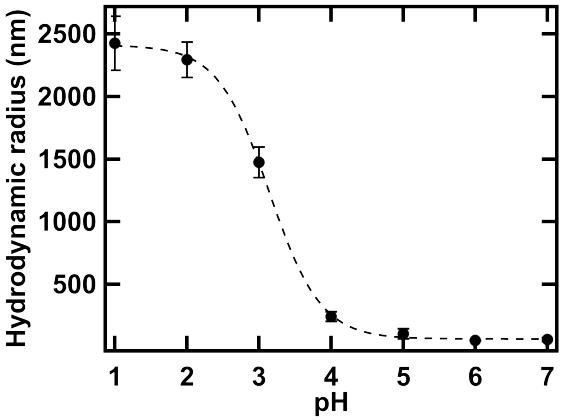

Figure 4.8. Variation of hydrodynamic radius of MUA-Au NPs as the function of pH, which was measured by DLS ([MUA-Au NPs] = 2.0 nM). The purple region indicates the pH range of aggregating MUA-Au NPs. Measurements were carried out 180 minutes after mixing with HCl.

Furthermore, the time course of pH and the mean particle size estimated by DLS measurements were shown in Figure 4.9. When the concentration of HCl is 1.0×10^{-4}, the pH value is almost constant around 7 from 0 h to 24 h (Figure 4.9a▲). On the other hand, the particle size increases slightly (Figure 4.9a●), namely, MUA-au NPs aggregated slowly in this HCl concentration. Although the pH value is also constant around 4 in the case of [HCl] = 2.0×10^{-4}, the particle size increases linearly from about 50 nm to 450 nm (Figure 4.9b). The rate of increase is greater for [HCl] = 2.0×10^{-4} than for [HCl] = 1.0×10^{-4}. When the concentration of HCl is further increased ([HCl] = 1.0×10^{-3}), the particle size increases dramatically until 5 h and becomes plateau, while the pH value was fixed at around 3 (Figure 4.9c). Therefore, it was found that the case of [HCl] = 2.0×10^{-4} behaved medium speed aggregation, and the [HCl] = 1.0×10^{-3} showed fast speed aggregation. In this study, the range of H^+ reservoir concentrations were from 1.0 to 2.0×10^{-4} M. Therefore, it is suggested that the pH-induced aggregation of this

experimental system was a relatively slow rate of aggregation dynamics, corresponding to Figure 4.9a and b

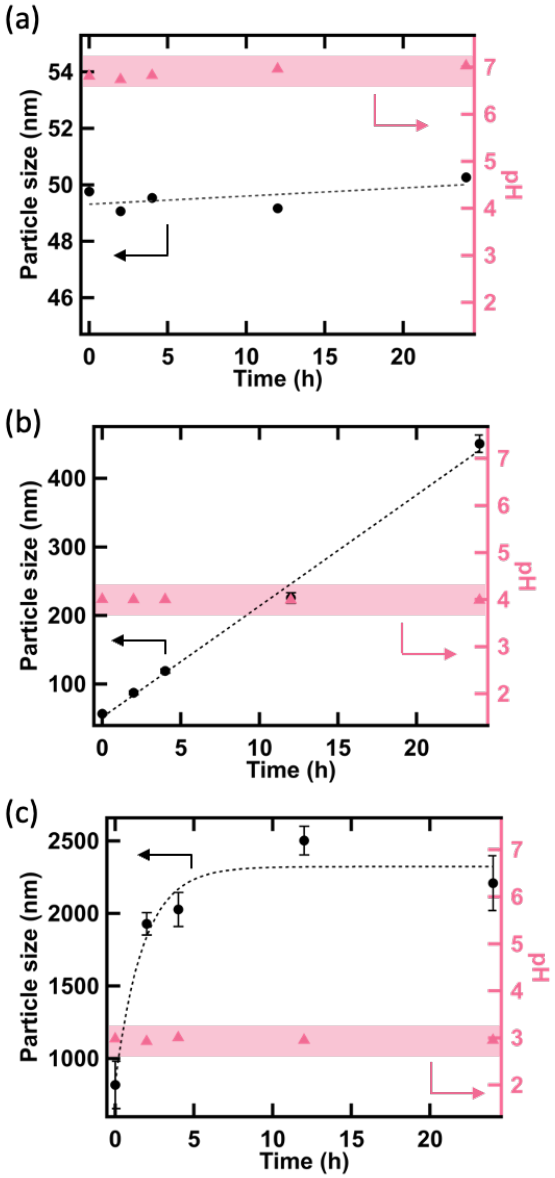

Figure 4.9. Changes in particle size (left black axis) and pH (right red axis) in MUA-Au NPs aq. soln. (1.0 nM) as a function of time and dependence on the concentration of adding HCl aq. soln.: (a) [HCl] = 1.0×10^{-4} M, (b) 2.0×10^{-4} M, and (c) 1.0×10^{-3} M. Particle size was measured by DLS.

4.3.6 UV-vis measurement with different pH in agarose gel

Figure 4.10a shows the color changes of agarose gels contained with MUA-Au NPs with different pH values from 2 to 7, which was adjusted by mixed with HCl. Until pH was 3, the color remained red, however it was changed to purple at pH 7. To discuss this pH responsibility, we performed UV-vis measurement (Figure 4.10b). As a result, LSPR peak intensity around 530 nm increases when pH decreases until 3. Also, this peak is red-shifted and broadening in the case of pH 2. The previous study reported that the LSPR peak just increased if nanoparticles aggregated weakly, then the peak was red-shifted if they aggregated strongly.[161] Therefore, it was suggested that MUA-Au NPs were aggregated weakly between pH 3 to 7. This pH range corresponded to the condition of pattern formation. Therefore, it was found that the pattern was formed via the weak pH-induced aggregation and following medium speed aggregation to form aggregates of MUA-Au NPs.

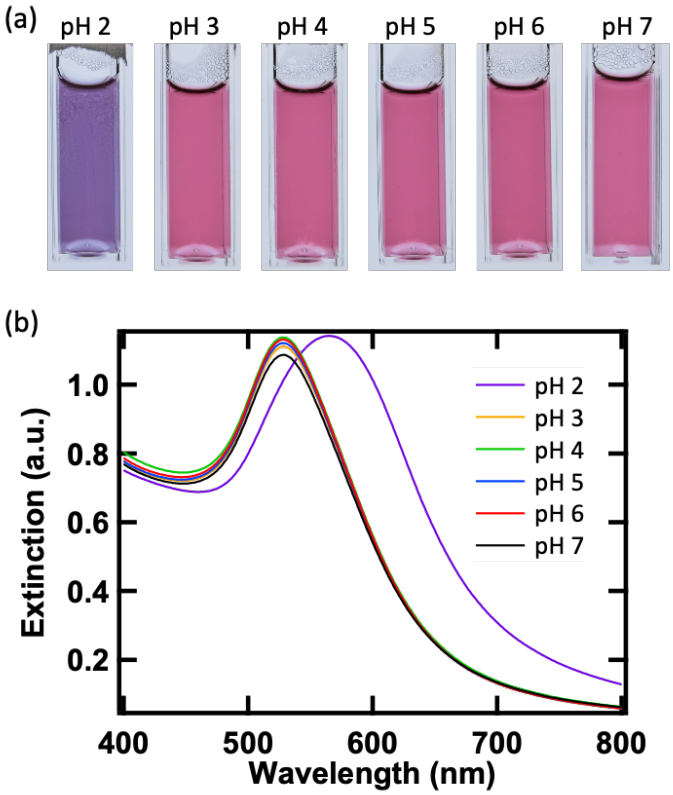

Figure 4.10. (a) Color changes of agarose gels doped with MUA-Au NPs 30 min after the pH is adjusted from 2 to 7 by HCl aq. soln. ([agarose] = 2.0 w/v% and [MUA-Au NPs] = 2.0 nM). (b) UV-vis spectra in (a).

4.4. Results and discussion: Pattern formation based on the pH-induced aggregation

4.4.1 Visualization of H^+ diffusion front with BTB

Before performing the pattern formation, a propagation behavior of the pH front due to the diffusion of H^+ was observed. Figure 4.11a-b shows the color changes of BTB indicator with the diffusion of H^+, where the color of BTB changes from blue to yellow when pH values change from 7.6 to 6.0. The pH of the region showing yellow means below 6.0, in which this value is the trigger of the aggregation (Figure 4.8). After 48h, the yellow front reached x = 60 mm (Figure 4.11d).

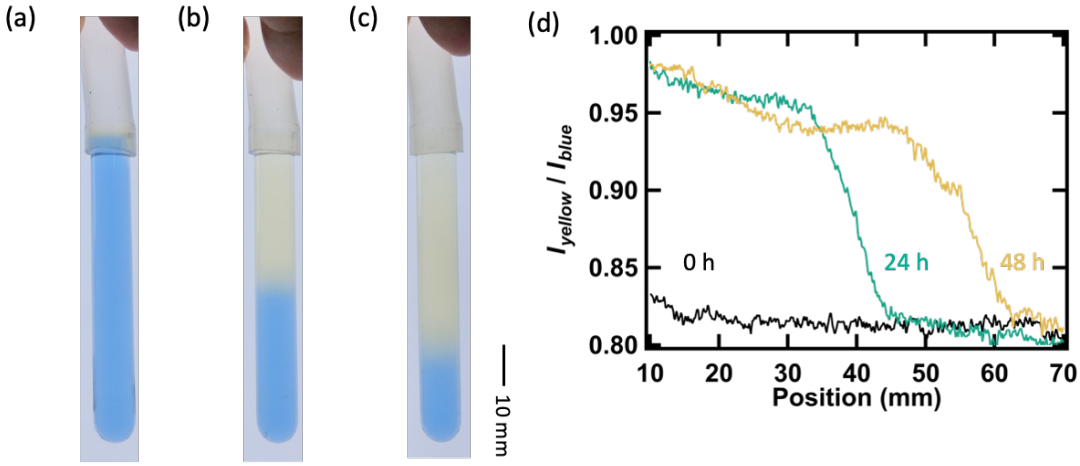

Figure 4.11. Visualization of H^+ diffusion front by BTB ([agarose] = 0.20 w/v%, $[HCl]_0$ = 1.0×10^{-4} M, and $[BTB]_0$ = 8.0×10^{-4} w/v%): (a) 0 h, (b) 24 h, and (c) 48 h. (d) Ratio of color intensity between yellow and blue as a function of position measured from the interface between the HCl reservoir and the gel.

4.4.2 pH-induced aggregation in the rectangular gel by directional H^+ diffusion

As shown in Figure 4.10, the pH-induced aggregation can be analyzed by spectroscopy. Therefore, I combined pattern formation in rectangular gels with MSP measurements to investigate the color change of pH-induced aggregation due to the directional diffusion of H^+ before pattern formation in test tubes (Figure 4.12a). When $[HCl]_0$ was 2.0×10^{-4} M, the MUA-Au NPs was strongly aggregated because the gel color changed to purple near the gel top (position 1). However, the concentrated red color appeared below the region 1 (position 2). Further below, the original red color was observed (position 3), meaning

MUA-Au NPs were dispersed. For each region, I performed MSP measurement (Figure 4.12b). Similar to the results of early UV-vis measurements, the LSPR peak intensity increased from position 3 to position 2. Previous study reported that such increase in peak value without red-shift indicates that Au NPs are weakly aggregated (transition (i)).[161] Furthermore, the peak became broadening and red-shifted at position 1 (transition (ii)), where such a red-shift in LSPR wavelength indicates that the nanoparticles are strongly aggregated. Thus, even in a test tube system, the contribution of aggregation can be clearly assessed by measuring the MSP at each position of the resulting pattern.

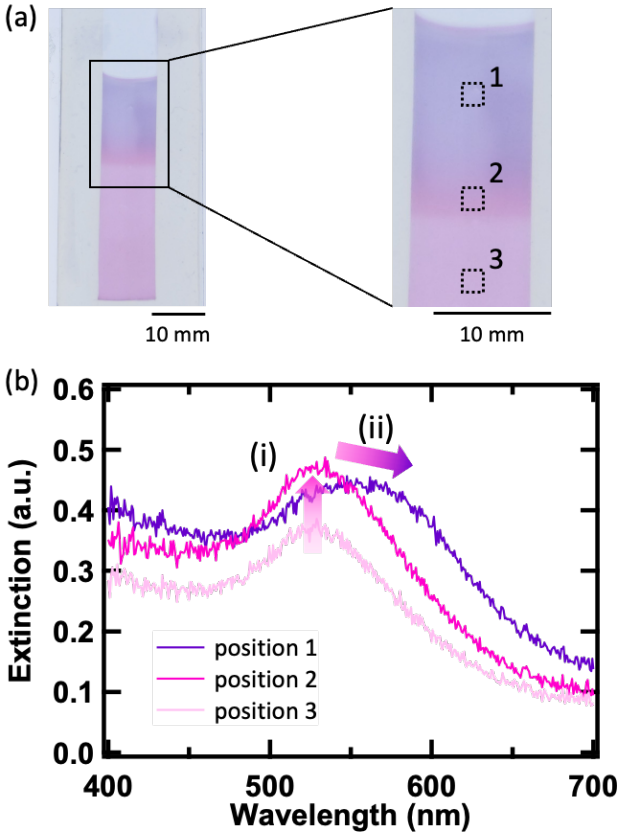

Figure 4.12. (a) Aggregation of MUA-Au NPs in the rectangular agarose gel by directional diffusion of HCl ([agarose] = 0.20 w/v%, $[HCl]_0 = 2.0\times10^{-4}$ M, and $[MUA\text{-}Au\ NPs]_0$ = 4.0 nM). (b) UV-vis spectra measured by MSP at the position from 1 to 3 in (a).

4.4.3 Pattern formation and observation

As mentioned in experimental section, NaOH was added in the gel (almost pH 10), thus MUA-Au NPs in the gel was deprotonated. After HCl solution was poured on the gel, H+ diffused into the gel (decreasing pH), and MUA-Au NPs were gradually protonated. Thus, aggregation of MUa-Au NPs was induced from the top of the gel. Figure 4.13a shows the obtained pattern in a test tube by pH-induced aggregation of MUA-Au NPs when the initial reservoir concentrations of HCl ($[HCl]_0$) and MUA-Au NPs ($[MUA\text{-}Au\ NPs]_0$) were 1.5×10^{-4} M and 4.0 nM, respectively. The boundary between the narrow black and bright red regions indicates the interface between the HCl reservoir and the gel, where this red color corresponds to the LSPR of MUA-Au NPs (Figure 4.4a). Also, the red color near the top of the gel became pale. To investigate the reason for it, I obtained the UV-vis spectra of different HCl concentrations in the HCl reservoir removed after pattern formation (Figure 4.14). Thus, the LSPR peak of MUA-Au NPs was observed at around 530 nm, indicating that MUA-Au NPs were eluted from the gel to the reservoir during the pattern formation and the color change was due to the elution. Therefore, such region with pale red color is represented as the elution ("*E*") region in Figure 4.13a. Below *E*, a relatively dark red region was continuously formed at approximately 5 mm. In this region, the peak value of LSPR increases without red-shift comparing with the brighter red regions (Figure 4.15). Therefore, it was indicated that MUA-Au NPs were weakly aggregated in this region. Thus, this region represents a region of continuous aggregation ("*CA*"). Below *CA*, the contrast between the dark and bright red regions appeared to form alternately. To make this contrast of alternative changes clearer, I transformed the original image (Figure 4.13a) into a grayscale image (Figure 4.13b) and conducted a line profile analysis (Figure 4.13c), where higher IGV values indicate that image colors at analyzed positions have darker gray color. In other words, IGV increases in the dark red region where the concentration of MUA-Au NPs is weakly aggregated. Near the interface (x = 0), the IGV is 0, corresponding to *E*, and then monotonically increases up to approximately x = 7 mm, namely, this region represents *CA*. The IGV after *CA* shows periodic oscillations, indicating that aggregation regions of MUA-Au NPs are formed discretely. Each IGV band corresponding to the peak position in oscillation is denoted by "*B*". The IGV gradually decreases farther from the interface as the H^+ concentration decreases because of reduced diffusion and aggregation force. Such a banding structure is in good agreement with characteristic LP morphologies.[20] While inorganic precipitates are distributed discretely in the classical LPs, the aggregation regions of MUA-Au NPs are distributed into bands, where each band contains many microscale aggregates (Figure 1d). As shown in Figure 4.11d, this *B* region is a well-diffused region of H^+ to induce the

aggregation. Therefore, this structure can be regarded as a novel LP structure based on the pH-induced aggregation. It is noted that the strong aggregation seen in Figure 4.12 does not occur in the test tube system because the change in the LSPR peak is not accompanied by a red-shift at *B* (Figure 4.15). Therefore, these aggregates might be formed through the only weak aggregation of NPs.

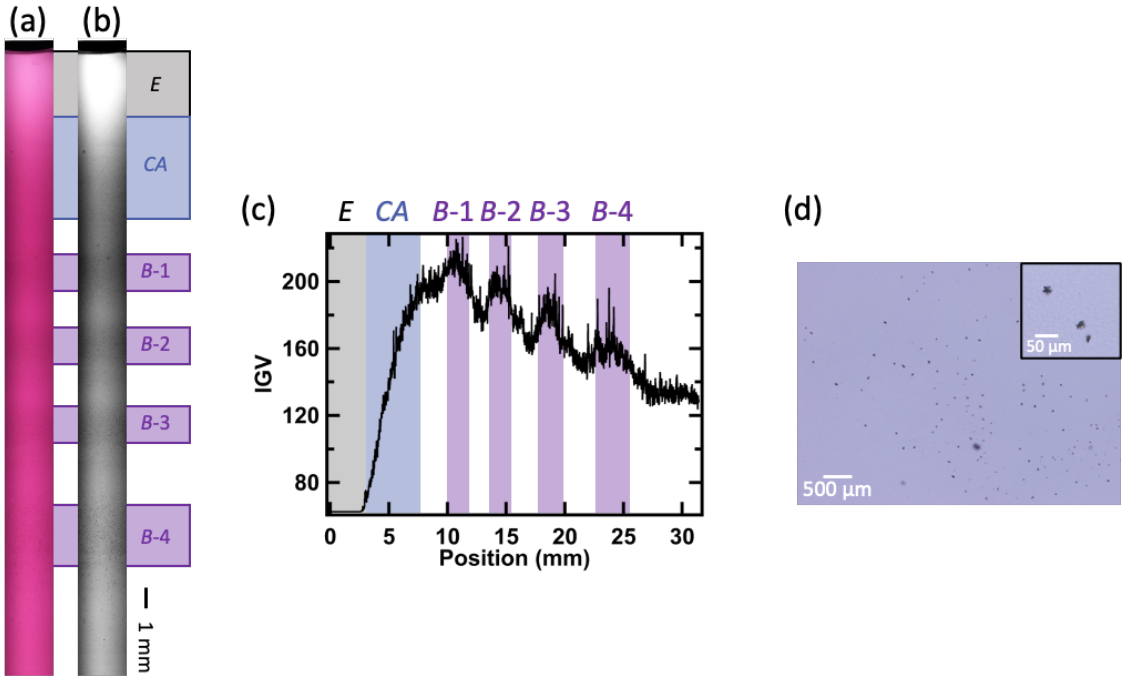

Figure 4.13. (a) Original image and (b) gray scale image of pattern formation by aggregation of MUA-NPs, where *E*, *CA,* and *B* represent the elution region, continuous aggregation region and aggregation band of MUA-Au NPs, respectively, and the number (*B*-*n*) associated with *B* is the band number. (c) Result of line profiling with inverted grey values in (b), the positions are measured from the interface between the HCl reservoir and the agarose gel. (d) Aggregates of MUA-Au NPs in *B*-4.

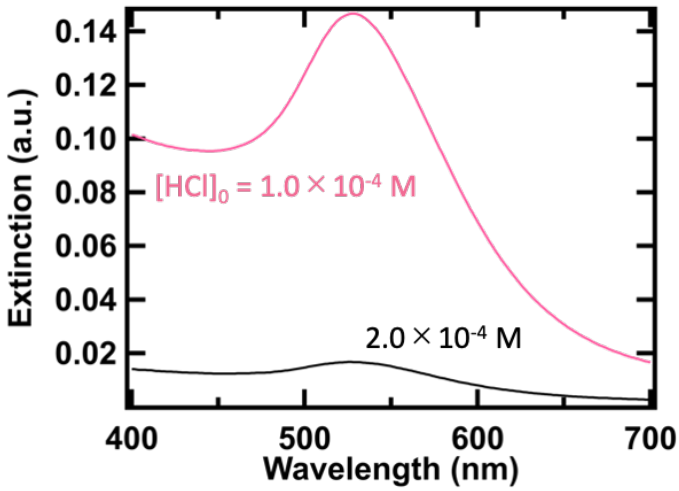

Figure 4.14. UV-vis spectra of HCl reservoir after pattern formation (2 weeks) with the different concentrations of HCl reservoir: $[HCl]_0 = 1.0\times10^{-4}$ M (red) and 2.0×10^{-4} M (black).

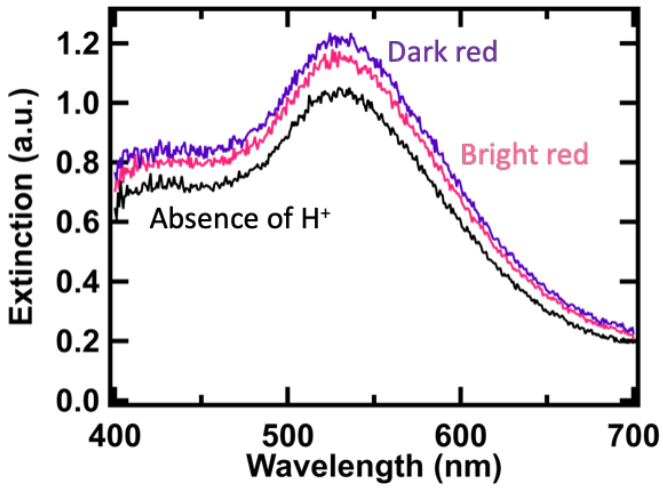

Figure 4.15. UV-vis spectra measured by MSP at the position of the dark red (purple) and bright red regions (red) in gel sample such as Figure 4.13a. The black spectrum is obtained out of the H^+ diffusion region.

4.4.4 Pattern formation dynamics

Then, I examined the dynamic process of pattern formation, which is crucial for establishing a model of the system. Figure 4.16a shows the time course of pattern formation until the formation of the first band region (*B*-1). Also, I defined the inter-band region with the decrease in IGV as the depletion region ("*D*") because significantly less

aggregates were formed in this region. As a result, *CA* appears by 12 h, and *D* and *B*-1 appear almost simultaneously after about 24 h. These dynamics were more clearly illustrated in the line profile (Fig. 4.16b), where the IGV of the *CA* (around x = 4 mm) increases with time, indicating progressive aggregation with time. The synthesized MUA-Au NPs were found to aggregate gradually in aqueous solutions with similar pH values (Figure 4.9). It was reported that the interaction between the polymer network and the nanoparticles reduces the diffusion coefficient of NPs in gels.[162-163] Therefore, the kinetics of aggregation slowed down in gels, resulting in prolonged aggregation. Furthermore, an interesting change was observed in the profiles of *D* and *B*-1: whereas there was no gap in IGV at the positions that would become *D* and *B*-1 (red and purple areas in Fig. 4.16b) after 12 h, there was a gap in IGV after 24 h, with negative and positive changes in IGV at each position. This indicates that the formation of *D* and *B*-1 occurs almost simultaneously and that the band domain of *B*-1 grows with time. These dynamics are consistent with the general properties of liquid-liquid and polymer-colloid phase separation systems.[164-165] Therefore, this pattern formation should be based on the phase separation mechanism of MUA-Au NPs. However, it is difficult to determine whether aggregation and phase separation are acting in concert or separately.

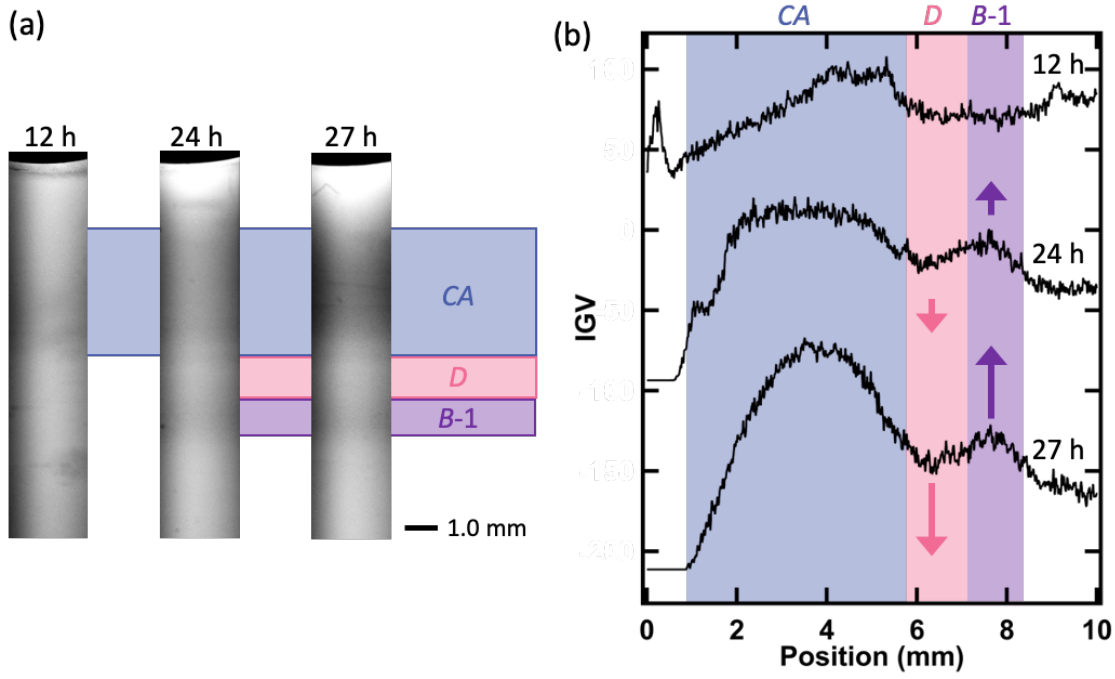

Figure 4.16. Successive images during the formation of the first band (*B*-1), in which *D* indicates the area where the aggregates are depleted. The experimental conditions are the same as in Figure 4.13. (b) Time course of the line profile in (a). The length of the arrows indicates the amount of change in each peak corresponding to the *D* (red) and *B*-1 (purple) regions.

4.4.5 Effect of the initial concentration of MUA-Au NPs and HCl

Having discussed the principles of pattern formation by the pH-induced aggregation, it is now necessary to evaluate the spatial periodic properties of the resulting patterns in comparison with conventional classical LPs. Then, I explored the effects of HCl and MUA-Au NPs concentrations on the spatial periodicity of the obtained LPs, using the spacing law (eq. (6)) and the MP law (eq. (8)). Firstly, the effect of $[\text{MUA-Au NPs}]_0$ was investigated (Figure 4.17).

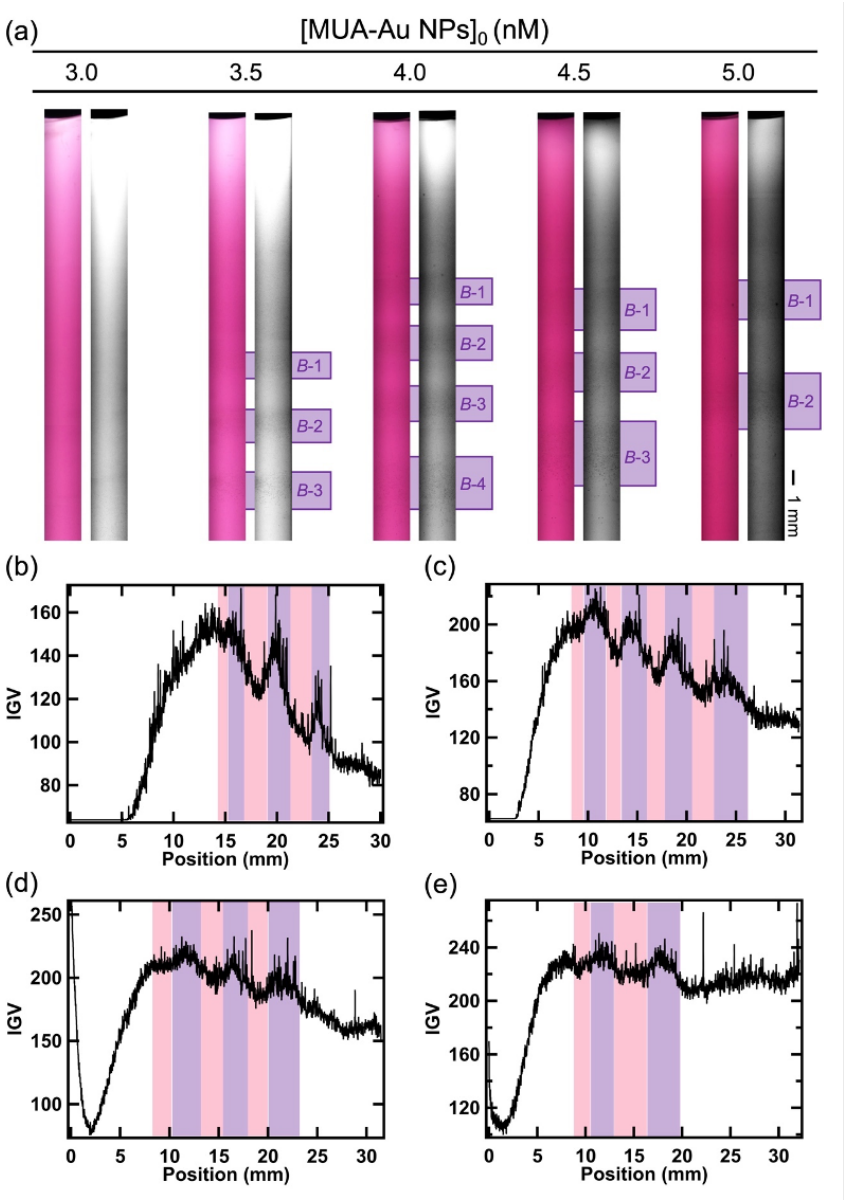

Figure 4.17. (a) Pattern formation with the different initial MUA-Au NPs concentrations ([agarose] = 0.20 w/v% and $[HCl]_0 = 1.5\times10^{-4}$ M). Left and right images in each set are original color and grayscale. Line profile in different $[\text{MUA-Au NPs}]_0$: (b) 3.5 nM, (c) 4.0 nM, (d) 4.5 nM, and (e) 5.0 nM. These profiles were obtained from grayscale images.

When $[\text{MUA-Au NPs}]_0$ = 3.0 nM, alternative regions between *B* and *D* were not formed. However, by increasing this concentration to 4.0 nM, up to four *B* regions could be obtained. On the other hand, the number of bands decreased again when this concentration increased further. To analyze the detail for the periodicity, the relationship between x_n and *n* were deduced from results of line profiles with different $[\text{MUA-Au NPs}]_0$ in this figure (Figure 4.18). At all concentrations ($[\text{MUA-Au NPs}]_0$ = 3.5, 4.0, 4.5 nM), x_n increases with *n* (Figure 4.18a), which is consistent with the characteristic properties of regular-type LPs. Therefore, this result clarifies that the patterns obtained by the pH-induced aggregation in this study are LPs. Furthermore, we plotted 1+*p* as a function of $[\text{MUA-Au NPs}]_0$ to compare the periodicities (Figure 4.18b). Originally, it was desirable to calculate 1+*p* by averaging the constant values obtained from x_{n+1}/x_n vs. *n* plots at large *n* for each concentration. However, because the number of bands is small in each sample in this system, 1+*p* is deduced by the ratio between x_{last} and $x_{last\text{-}1}$. The value of 1+*p* increases exponentially with $[\text{MUA-Au NPs}]_0$, which is good agreement with the prediction based on the classical MP law as shown in Figure 2.1.

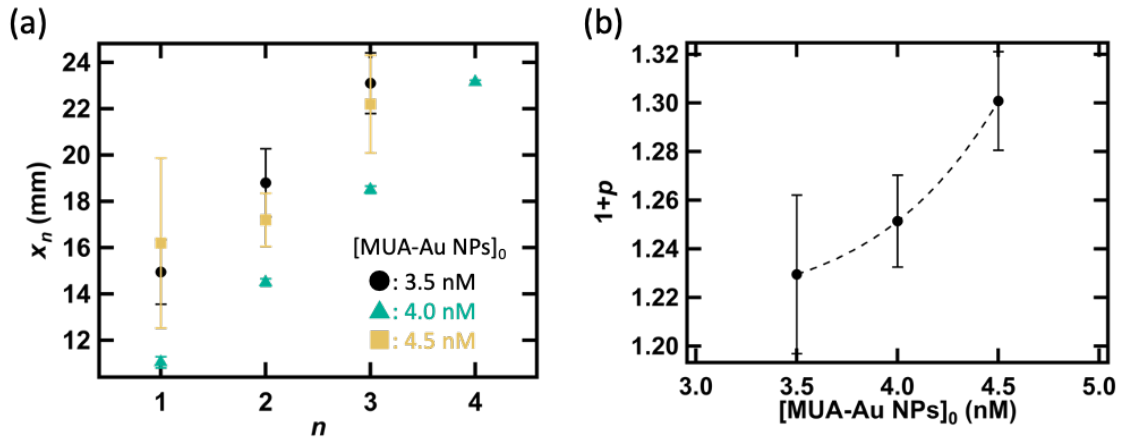

Figure 4.18. (a) The change in x_n as a function of *n* depending on $[\text{MUA-Au NPs}]_0$ (●: 3.5 nM, ▲: 4.0 nM, ■: 4.5 nM). (b) Relationship between 1+*p* and $[\text{MUA-Au NPs}]_0$.

I also demonstrated the effect of $[\text{HCl}]_0$ (Figure 4.19). Compared to the dependence for MUA-Au NPs, the conditions which a pattern consisting of multiple bands ($n \geq 3$) could be formed were limited (Figure 4.19a). In fact, only under conditions of $1.5\times10^{-4} \leq [\text{HCl}]0 \leq 1.75\times10^{-4}$ can a pattern consisting of several bands be formed (Figure 4.19b,c). Also, obtained patterns under this limited condition shows well-defined periodicities as the regular-type (Figure 4.19d). Therefore, the patterns formed are all of the regular-type regardless of the change in the concentrations of MUA-Au NPs and HCl. Furthermore, the *p* value is smaller in the case of $[\text{HCl}]_0 = 1.75\times10^{-4}$ M than the case of 1.5×10^{-4} M

(Figure 4.19e). This trend is consistent with the MP law prediction.

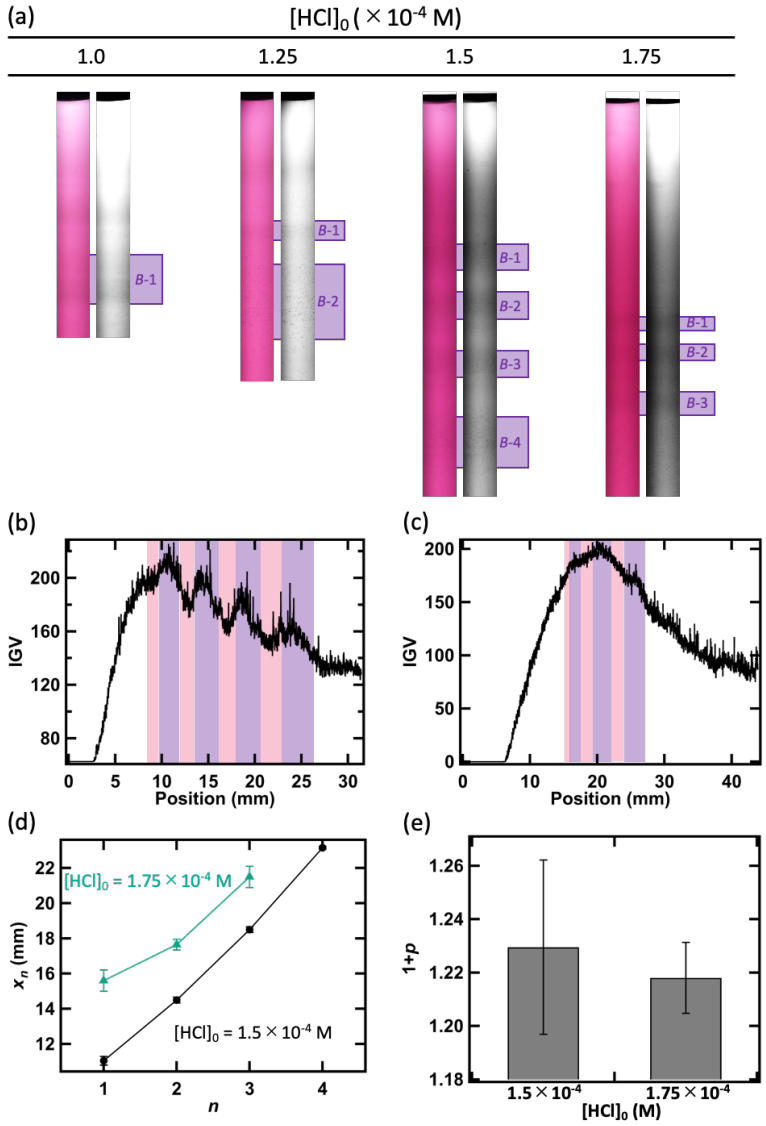

Figure 4.19. (a) Pattern formation with the different initial HCl concentrations ([agarose] = 0.20 w/v% and [MUA-Au NPs]$_0$ = 4.0 nM). Left and right images in each set are original color and grayscale. Line profile in different [HCl]$_0$: (b) 1.5×10^{-4} M and (c) 1.75×10^{-4} M. (d) Variation of band position (x_n) with band number (n) in different [HCl]$_0$ (●: 1.5×10^{-4} M and ▲: 1.75×10^{-4} M). (e) Relationship between $1+p$ and [HCl]$_0$.

Therefore, the variation of p depending on the concentrations of invading (HCl) and pre-doped (MUA-Au NPs) species are good agreement with the well-known prediction of MP law for the nucleation-based scenario, despite the LP formation due to the pH-induced aggregation is based on the phase separation-based scenario. This result suggests that it may be possible to describe the LP formation mechanism comprehensively, regardless of the nucleation or the phase separation-based scenarios.

4.4.6 Numerical RD simulations with CH equation

Finally, to gain deeper insight into the pattern formation mechanism of this system, we performed numerical simulations based on the RD equation coupled with the CH equation.[116-120, 129] The following chemical processes were included in the pH-induced aggregation scheme in this study:

Protonation:

$nH^+ + \text{Au NP-}(COO^-)_n \rightarrow \text{Au NP-}(COOH)_n$ (52)

Phase transition and separation:

$m\text{Au NP-}(COOH)_n \rightarrow (\text{Au NP})_m$ (53)

where $\text{-}(COO^-)_n$ and $(\text{Au NP})_m$ are the MUA molecules on the Au NP surface and aggregates of MUA-Au NPs, respectively. Subsequently, we express the above processes for the simulation as

***Protonation*:**

$A + Z \rightarrow Z^*$ (54)

***Phase transition and separation*:**

$Z^* \rightarrow Z^{**}$ (55)

Each species in Eqs. (54) and (55) corresponds to the chemical species in Eqs. (52) and (53), respectively. Based on these assumed processes, we constructed the following RD equations, referring to past numerical studies for the post-nucleation models:[116-117, 129]

$$\frac{\partial a}{\partial t} = D_a \frac{\partial^2 a}{\partial x^2} - 10kzPrt(x,t), \quad (56)$$

$$\frac{\partial z}{\partial t} = D_z \frac{\partial^2 z}{\partial x^2} - kzPrt(x,t), \quad (57)$$

where a and z are concentrations of A and Z, D_a and D_z are the diffusion coefficients of A and Z, respectively, and k is the rate constant of the protonation reaction. To consider the chemical amphipathic relationship between the number of MUA molecules per one MUA-Au NP surface and protons, we added the correction coefficient number (10) before $kzPrt(x,t)$ in eq. (56). The protonation progresses dramatically with pH changes as shown in Figure 4.6. Therefore, the term for the protonation should be denoted using the sigmoid function. Then, the protonation function $Prt(x,t)$ was represented by the following sigmoid-type function:

$$Prt(x,t) = z\left(\frac{1}{1+e^{-\alpha(a(x,t)-K_a)}}\right), \quad (58)$$

where α and K_a are a coefficient that determines the degree of change and acidity constant. The eq. (58) represents that the Z* is accumulated at the position where A was diffused and increased. Also, α controlled the responsibility of the Z* production (meaning protonation) to the increase in A. In this study, we fixed α and K_a at 1.0 and 12. When the system becomes unstable by the increase in Z*, a phase separation of Z* into regions of high (z_h) and low concentrations (z_l) takes place, where the region with z_h means existence of Z** (aggregation). This process is denoted by the following CH equation with protonation source ($kzPrt(x,t)$) and noise (η_Z) terms:

$$\frac{\partial X}{\partial t} = -\lambda \frac{\partial^2}{\partial x^2}\left(\varepsilon X - \gamma X^3 + \sigma \frac{\partial^2 X}{\partial x^2}\right) + kzPrt(x,t) + \eta_Z. \qquad (60)$$

Here X is the concentration of Z* shifted by $\overline{z^*} = (z_h + z_l)/2$ and scaled by $\widehat{z^*} = (z_h - z_l)/2$, such that $X = (z^* - \overline{z^*})/\widehat{z^*}$ is 1 for $z^* = z_h$ and X is −1 for $z^* = z_l$.The parameters λ and σ are the kinetic constant of the phase separation and surface energy, ε and γ are the characteristic constants. The ratio between λ and σ defines a characteristic timescale of the unstable region growing. Also, σ guarantees stability for perturbation, it is typically set positive value ($\sigma > 0$). In this study, we used 0.5 and 0.8 for λ and σ. The values of ε and γ define a binodal boundary and a spinodal boundary. Also, we set ε was positive, namely, the phase separation was driven by the spinodal decomposition. Values of ε and γ were 1.0. The above parameters were fixed in all simulations. Since fluctuations are inherent in various chemical phenomena, we have taken their effects into account with a noise term (η_Z) that is defined by $\eta_Z = r\sqrt{kzPrt(x,t)}$ where r is uniformly distributed in $[-\eta, +\eta]$. We used 0.02 as this parameter. Also, the space grid-step Δx = 1 is employed on a 100×400 grid, and the time step Δt = 0.001 and total time steps t = 500000 are used. Furthermore, the initial conditions were set as represented below: $a(x = 0, t = 0) = a_0$, $a(x > 0, t = 0) = 0$, and $z(x, t = 0) = z_0$, where a_0 and z_0 are initial concentrations of A and Z. Also, we used no-flux boundary conditions at the end of the calculation space (100×400 grid) and Dirichlet boundary conditions at the boundary between the A reservoir and the area pre-doped with Z, namely $a(x = 0, t) = a_0$. All parameters were treated as dimensionless.

Figures 4.20a and 4.20b show a typical output image and the corresponding concentration profile of X. Under the vertical position = 0, corresponding to the boundary where the Dirichlet condition of A was set, a periodic banding pattern was obtained (Figure 4.20a). In addition, a clear oscillation is formed in the concentration profile (Figure 4.20b), which is consistent with the oscillation obtained experimentally (Figure 4.13c). Furthermore, I show the time course in the simulation until B-1 (Figure 4.20c) and

further *B* formation (Figure 4.20d). At t = 15000, the concentration gradient of Z* is formed by the diffusion of A and protonation of Z, however there is no gap in *X* at positions that will become *D* (red region) and *B*-1 (purple region). However, at t = 22000, *X* shows negative and positive changes at *D* and *B*-1 and a gap is created, indicating the beginning of phase separation. Finally, this gap increases until t = 40000, where phase separation is completed. A further band (*B*-2) was formed by repeating the same protonation and phase separation processes (Figure 4.20d). These behaviours were consistent with the experimental results, indicating that the LP formation based on the pH-induced aggregation progressed via a phase separation mechanism.

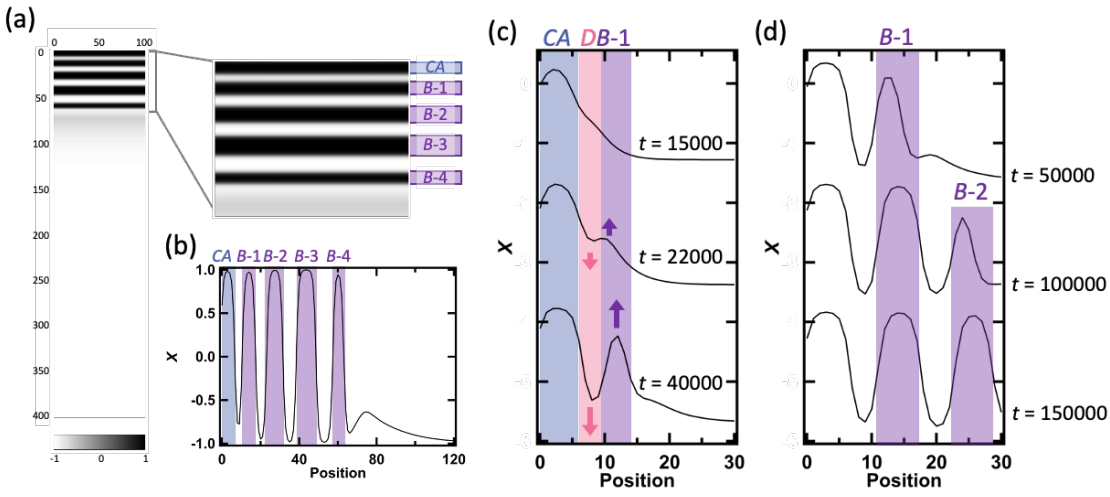

Figure 4.20. (a) Concentration distribution of *X* from the RD simulation (a_0 = 60, z_0 = 1.0). (b) Concentration profile of *X* in (a). The position "0" indicates the Dirichlet boundary for A ($a(x = 0, t) = a_0$). Time course of the concentration profile of *X* (c) during the 1st band (*B*-1) formation and (d) for longer periods of time under the same simulation condition in (a). The blue-, red-, and purple-colored regions in (c) correspond to the *CA*, *D*, and *B-1* bands, respectively.

Furthermore, similarly to the experiments showing the dependence of [MUA-Au NPs]$_0$ shown in Figures 4.17 and 4.18, the influence of the initial concentration of the pre-doped species (z_0) was also observed in the simulation results (Figure 4.21 and Figure 4.22). In Fig. 4.21a, no banding pattern was obtained at z_0 = 0.4, whereas increasing until z_0 = 1.0 resulted in the formation of clear discrete bands and an increase in the total number of bands. Any further increase in z_0 caused a thickening of the bands and a decrease in their number. This trend is consistent with the trend seen in Figure 4.17, where the appearance of the pattern changes in response to changes in the concentration of MUA-Au NPs. Furthermore, I explored x_n changes as a function of n, analyzed from Figure 4.21b-e (Figure 4.22a). As a result, the x_n values increased with increasing n for all conditions of

z_0. Furthermore, the $1+p$ values increased exponentially with an increase in z_0, which corresponds to the above experimental results (Figure 4.18a) and the classical MP law. To investigate the reason why the resulting pattern obtained from both experiment and simulation followed this classical rule, I carefully observed the changes in the simulation over time (Figure 4.22c,d). These figure show the time course of the profile of X for different z_0. For a low value of z_0 = 1.0 (Figure 4.22c), X only increases with time, indicating the growth of the B region (purple arrow (i)). At the same time, the valley of the profile corresponding to the next D deepens and moves away slightly (red arrow (i)). On the other hand, at the high value of z_0=1.2 (Figure 4.22d), the X in the B region becomes larger (purple arrow (i)) and the region spreads towards the distance (purple arrow (ii)). Furthermore, the valley in the D region moves clearly at first (red arrow (i)) and then becomes deeper (red arrow (ii)). This enlargement of the previous band (B_n) and the movement of the D region due to the increase of z_0 increase the central distance between B_n and the next band (B_{n+1}) and increases $1+p$. In the previous experimental result based on the nucleation-based scenario shown in Figure 2.1b, increasing b_0 caused such enlargement of each band, thus $1+p$ increased due to the greater distance between the bands and the centre of the bands. The consistency between the two scenarios is suggested to be since solid-phase transition processes such as nucleation and phase separation are driven under the limit of the diffusion flux of invading species. In other words, although the mechanisms of the various pattern formations in the Liesegang phenomenon is bifurcated depending on the thermodynamic state of the system, obtained patterns may be discussed in a unified mechanism.

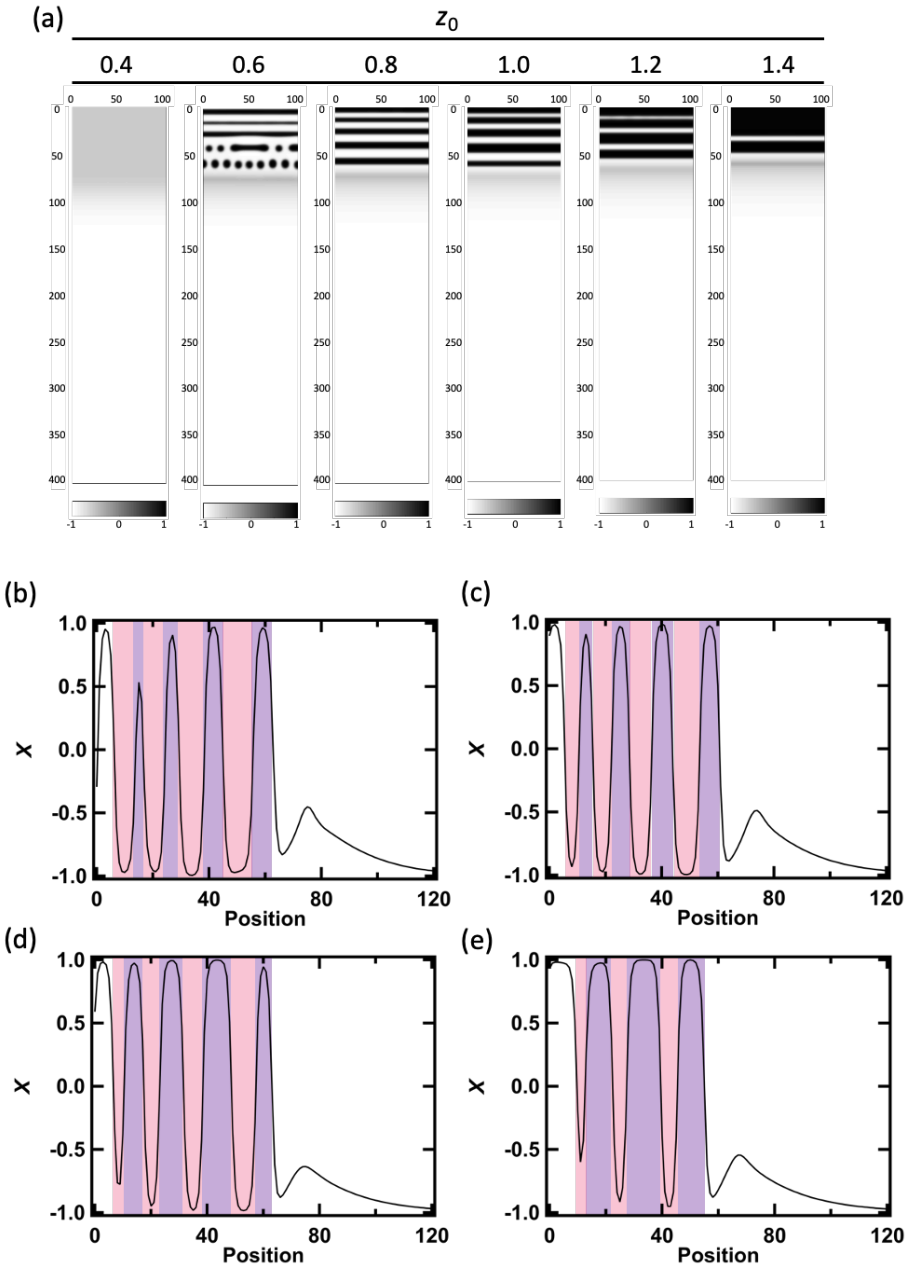

Figure 4.21. (a) Concentration distribution of X from RD simulation with different z_0 (t = 500000, a_0 = 60, D_a = 10, D_z = 1.0, α = 1.0, k = 1.0, K_a = 12, λ = 0.5, $\varepsilon = \gamma$ = 1.0, σ = 0.8, η = 0.02). Line profile in different z_0: (b) 0.6, (c) 0.8, (d) 1.0, and (e) 1.2.

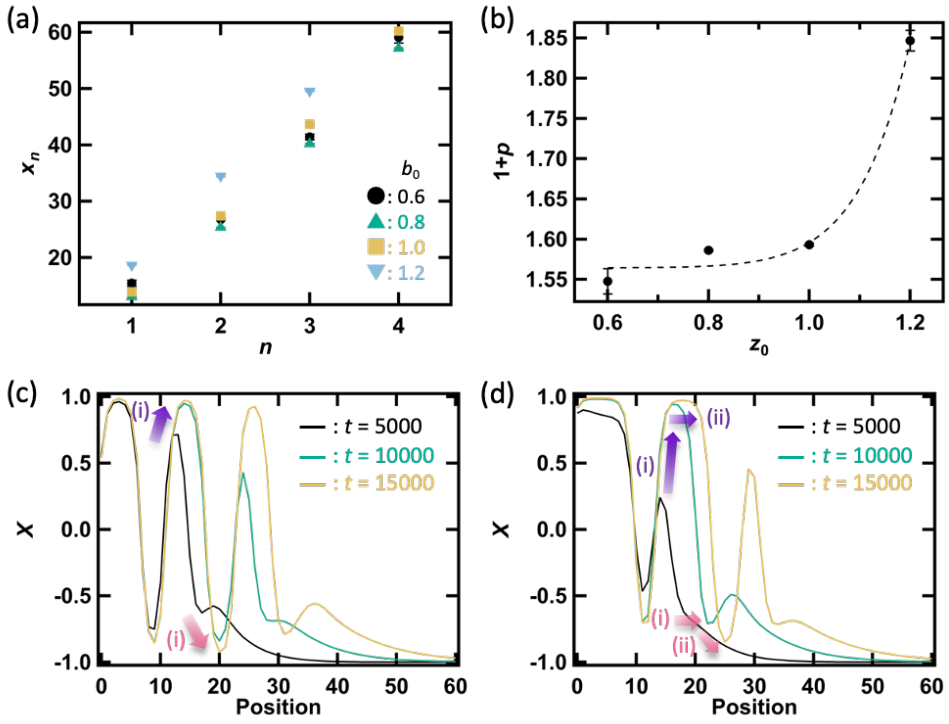

Figure 4.22. (a) Variation x_n as the function of the band number and dependence on z_0 (●: 0.6, ▲: 0.8, ■: 1.0, and ▼: 1.2). (b) Relationship between 1+p and z_0. (c) Dependence of z_0 on the time course of the concentration profile of X: (c) z_0 = 1.0 and (d) z_0 = 1.2. Numbers beside the arrows with gradation color represent steps of concentration changes.

In support of this expectation, the simulation with different a_0 showed a very good agreement with the experimental results (Figure 4.19) in terms of the a_0 dependence (Figure 4.23). Indeed, as a_0 was increased, 1+p was decreased (Figure 4.23d), which is similar trend to Figure 4. 19. As we can see, the spatial periodicity obtained in the phase separation-based scenario are in perfect agreement with those obtained in the nucleation-based scenario, and it is clear that the results obtained can be interpreted in a comprehensive way, even though the dynamics of pattern formation are different between the two.

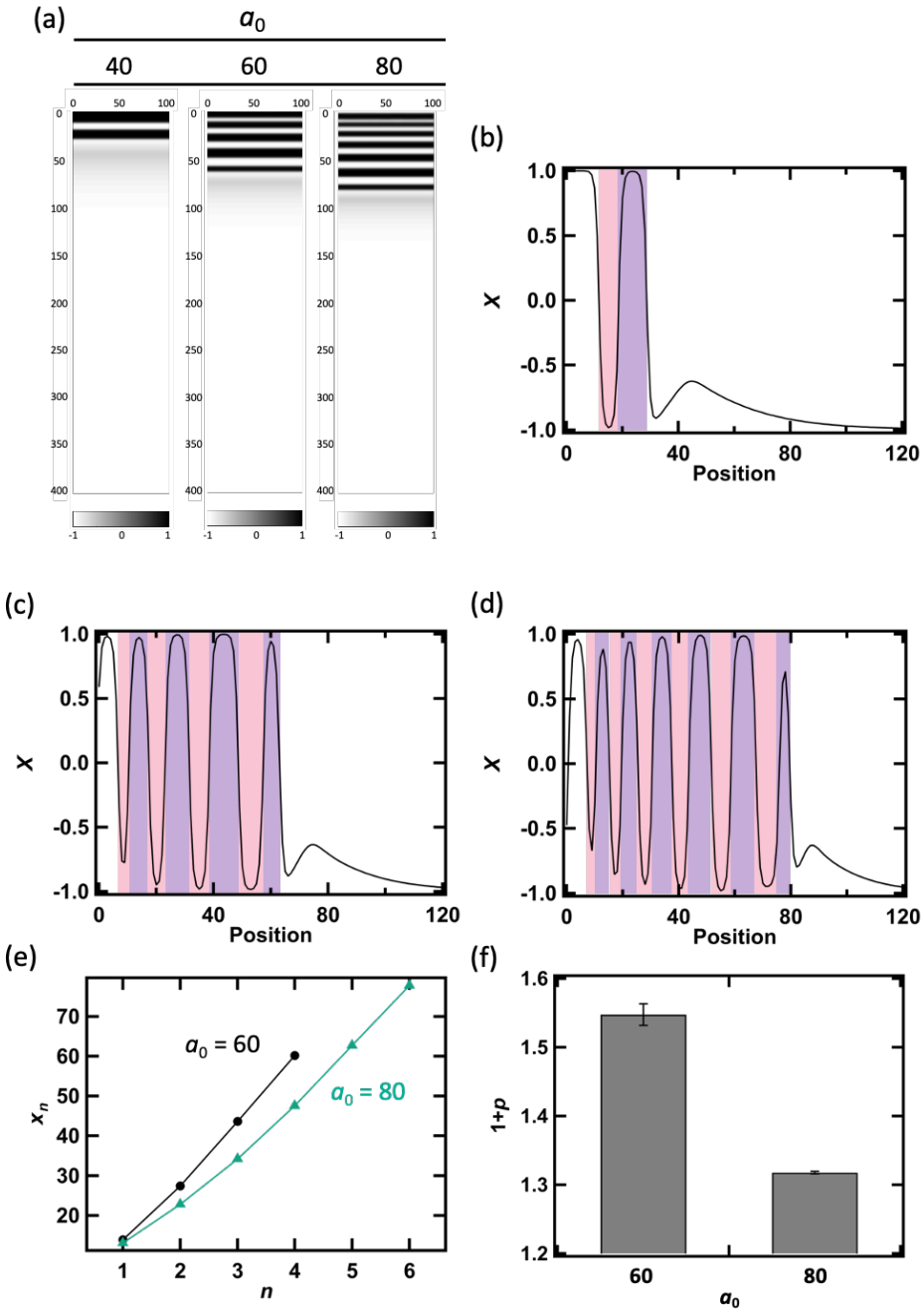

Figure 4.23. (a) Concentration distribution of X from RD simulation with different initial concentrations of A (a_0) (t = 500000, z_0= 1.0, D_a = 10, D_z = 1.0, α = 1.0, k = 1.0, K_a = 12, λ = 0.5, $\varepsilon = \gamma$ = 1.0, σ = 0.8, η = 0.02). Line profile in different a_0: (b) 40, (c) 60, and (d) 80. (e) Variation of x_n with n in different a_0 (●: 60 and ▲: 80). (e) Relationship between p and a_0.

4.4.7 Pattern formation mechanism based on the pH-induced aggregation

The results of both experiments and simulations suggest that the pattern is formed via the following phase separation process. The first trigger for the whole process is the formation of a H^+ diffusion gradient in the gel pre-doped with MUA-Au NPs due to the directional diffusion of H^+ (Figure 4.24 (i)). Subsequently, the protonation of the MUA-Au NPs proceeds according to the gradient and the protonated MUA-Au NPs accumulate in the gel and their concentration gradient evolves (Figure 4.24 (ii)). When the protonation gradient has grown to a certain extent, phase separation by spinodal decomposition proceeds, resulting in the simultaneous formation of banding and depletion regions (Figure 4.24 (iii)). These processes are repeated farther and farther by propagation of the phase separation front due to further H^+ diffusion, resulting in the formation of the LP with discrete regions of particle aggregation (Figure 4.24 (iv)).

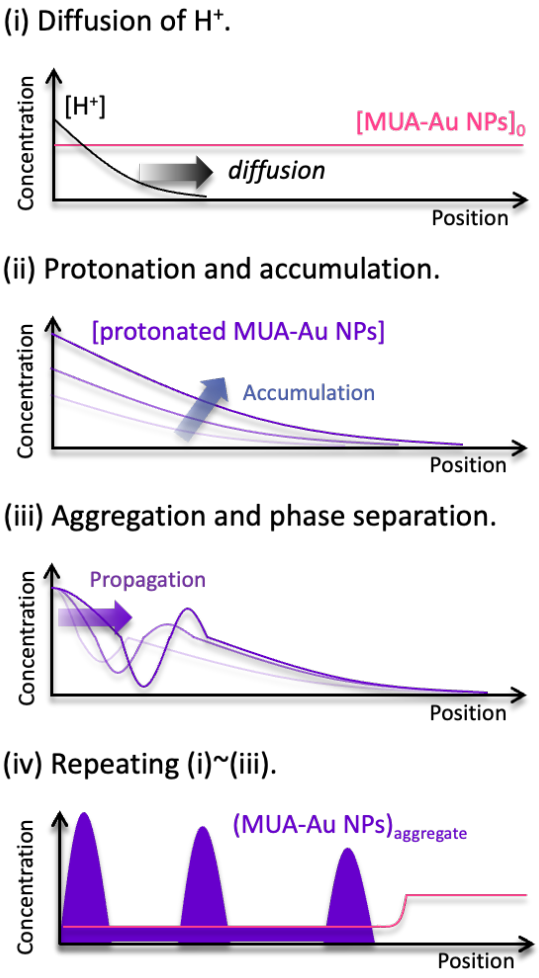

Figure 4.24. Illustration of formation mechanism for the phase separation-based scenario induced by the pH induced aggregation of MUA-Au NPs.

4.5 Conclusions

In this study, we successfully developed a novel experimental to be able to demonstrate the phase separation-based scenario by focusing on the pH-induced aggregation of MUA-Au NPs and the corresponding numerical RD simulation model. Furthermore, we demonstrated the effect of experimental conditions, such as the invading and pre-doped species concentrations, on the spatial periodicity of the obtained LP. As a result, we found that the periodicity in this system was modulated in a similar manner as LP formed thorough the nucleation-based scenario, with trends consistent with the classical MP law. So far, there have been studies that have examined for the phase separation effect separately from experimental[86, 124-125] and mathematical[116-117, 129] perspectives, however only a few studies have combined both perspectives. Also, to the best of our knowledge, there is no study that compares the features obtained in the phase separation-based and nucleation-based scenarios from both experimental and simulation points of view, as in this study. Hence, our experimental system can be regarded as a novel platform for describing the mechanism based on the phase separation-based scenario. Importantly, we found that Liesegang phenomenon provides similar spatial periodic properties irrespective of the bifurcated scenario. Therefore, it is suggested that both scenarios can be described in a unified way by using physical variables that represent thermodynamic states in mathematical model. Thus, the phase separation-based scenario is very practical as one of the mechanisms driving LP formation. From these perspectives, we can use LP as the chemical model to discuss LP-like patterns in nature[110-111, 113, 146-147] as well as other conventional RD studies.[13, 16-17]

Chapter 5 Conclusions and future perspectives

Spontaneous order formation under nonequilibrium conditions, namely self-organization, is ubiquitous in both natural and artificial environments. Dissipative structures are one of the most typical examples of such self-organized structures. To understand the mechanisms of their structure formation, experimental and mathematical scientific approaches are essential, and most of previous research to date has followed this process of thought. Dissipative structures can be classified into several classes according to the type of nonlinear reaction in the source of formation, among which systems in which directional diffusion and associated solid-phase transition processes act competitively can be modelled by the Liesegang phenomenon. However, more than a century after its initial discovery, the phenomenon remains fundamentally poorly understood and lacks practicality as a model. To address this issue, this thesis focused on the fact that the Liesegang phenomenon manifests itself via different bifurcated thermodynamic scenario, and aimed to understand the specific unresolved issues in each scenario by taking both experimental and mathematical approaches.

In Chapter 1, after an introduction to the thermodynamics of nonequilibrium and self-organization, examples of different classes of dissipative structure formation are presented and the history of model studies for each is described. Furthermore, the basic knowledge about the Liesegang phenomenon was explained from various points of view (e.g. spatiotemporal periodicity, material diversity, morphological features of the patterns, etc.). After that, considering that the formation mechanism of the Liesegang phenomenon can be bifurcated into two scenarios depending on the thermodynamic state of the system: the nucleation-based scenario and the phase separation-based scenario, the unresolved issues in each scenario are introduced, and the purposes of this study are described based on them.

In Chapter 2, I focus on the fact that the methods used to evaluate LPs periodicities formed by the nucleation-based scenario do not consider F_{diff}, which is important for the formation of LPs. To clear this effect, I used the volume effect of the reservoir. When the small reservoir ($V_{gel} > V_{res}$), which is the typical condition in most previous studies, the periodicity of obtained LP depended on decreasing a_{res} with the progress of diffusion. On the other hand, when the reservoir was relatively large, the approximation $a_{res} = a_0$ was valid and a_{res} was always kept constant. This means that even if we set the same a_0 between both reservoir conditions, the periodicity is decided by a different F_{diff} from the previous condition. Such a change in LP periodicity due to factors other than electrolyte concentration could not be considered in the existing classical MP law. Then, I modified

this law to use F_{diff} as a variable instead of a_0. Thus, it is now possible to describe the periodicity changes of the different reservoirs described above in a single unified relationship. This effect of F_{diff} is supported by both experiments and numerical simulations, which show that the Liesegang phenomenon exhibits periodicity in response to imposed F_{diff}.

In Chapter 3, I focused on the fact that, although the nucleation process is the most important determinant of the nucleation-based scenario, there is no experimentally validated explanation of the geometrical transitions that LPs show under specific conditions. By using gels involved in the kinetic control of nucleation in LP formation, I then preparade the spatial K_2 modulation by changing their spatial concentration. As a result, simulations of spatially fixed K_2 and experiment of mono-layered gels with spatially fixed gel concentrations showed that only regular-type periodicities were formed in both cases. On the other hand, the periodicity transited depending on Δ[agarose] when I used bi-layered gels made by stacking of two gels with different agarose concentrations. Furthermore, in order to understand the results of the experiment, a simulation was performed under the condition that K2 was modulated only once at an arbitrary position, and as in the experiment, the periodicity transition depending on ΔK_2 was observed at the modulation point. Thus, I found that the spatial modulation of the nucleation rate is the main key parameter dominating the transitions in the Liesegang phenomenon. To show that this consideration is more robust, I finally formed patterns in the multi-layered gels. Thus, this system showed that the periodicity was modulated throughout the whole of the system, unlike the local transitions that appear in the bi-layered gels system described above. Therefore, both experiments and supporting simulations showed that almost all the geometrical changes exhibited by the Liesegang phenomenon in the nucleation-based scenario can be explained in terms of the kinetics of nucleation.

In Chapter 4, I focused on the fact that there has been little experimental validation of the phase separation-based scenario. To make this possible, I combined the pH-induce aggregation of MUA-au NPs with the typical 1D Liesegang system, and the aim of the project was to construct an experimental system that could faithfully reproduce the above scenario. As the pH in the gel pre-doped with MUA-Au NPs decreased with H^+ diffusion, alternating regions with the presence or little presence of nanoparticle aggregates were gradually formed from the H^+ reservoir. In contrast to the nucleation-based scenario, these opposing regions formed simultaneously in this system. Therefore, it was suggested that the obtained LP was formed due to the phase separation mechanism. To support of this view, I have performed numerical simulations using the CH equation and RD equation, which can simulate the formation of periodic structures based on a phase separation

mechanism. As the pattern formation proceeded in exactly the same manner as the experimental results, this system provides a useful experimental model for demonstrating the phase separation-based scenario. Furthermore, it was that the spatial periodicity obtained from both experiment and simulation showed good agreement with the empirical law constructed on the basis of the nucleation-based scenario. These results not only show that the phase-separation-based model is a practical part of a bifurcated model of the Liesegang phenomenon, but also that it may provide a unified description of the mechanism by which periodic structures are formed in bifurcated scenarios with and without nucleation.

Based on the above discussion, the main highlight of this thesis is the achievement of a fundamental understanding of the Liesegang phenomenon through a comprehensive approach combining experimental and mathematical modelling of the unresolved issues in each of the thermodynamically bifurcated scenarios that have not been fully explored in previous studies. These results enable a rational interpretation of almost all the phenomena inherent in the Liesegang phenomenon, and can be applied to elucidate the formation mechanisms of similar patterns ubiquitous in nature, such as practical dissipative structure formation models of BZ reactions and Turing patterns. Therefore, it is hoped that the results of this thesis will lead to significant breakthroughs for researchers in a variety of fields targeting the Liesegang phenomenon.

However, even with this basic understanding, the detailed causes of the morphological changes, in particular, helix and spot structures formation described in Sec. 1.6.3 remain an open question. Since thermodynamic fluctuations probably underlie this problem, a systematic investigation of the effects of various physicochemical parameters (e.g., temperature, concentration, etc.) on the fluctuations is necessary to understand it. Furthermore, most of the previous studies on LPs have focused on the macroscopic view of the periodicity of formation, however recently attempts have been focusing on the morphology of individual particles in each precipitation band and to apply this to particle synthesis approaches (e.g. Figure 1.15c). However, these controls are empirical and there is no theoretical blueprint to predict them reasonably well. Therefore, the discussion of such particle morphological changes linked to the description of reaction-diffusion dynamics in the Liesegang phenomenon allows a comprehensive understanding of all macroscopic and microscopic phenomena in the Liesegang phenomenon.

References

[1] G. P. Nicolis, Ilya, *Self-organization in nonequilibrium systems: From dissipative structures to order through fluctuations*, Wiley, Germany, **1977**.

[2] M. C. Cross, P. C. Hohenberg, Pattern formation outside of equilibrium, *Rev. Mod. Phys.,* **1993**, *65*, 851-1112.

[3] I. R. P. Epstein, John A. , *An introduction to nonlinear chemical dynamics: Oscillations, waves, patterns, and chaos*, Oxford University, USA, **1998**.

[4] A. Goldbeter, Dissipative structures and biological rhythms, *Chaos: An Interdisciplinary Journal of Nonlinear Science,* **2017**, *27*, 104612.

[5] A. Goldbeter, in *Special volume in memory of ilya prigogine*, **2007**, pp. 253-295.

[6] P. E. Cladis, *Spatio-temporal patterns in nonequilibrium complex systems*, CRC Press, USA, **1994**.

[7] D. Walgraef, *Spatio-temporal pattern formation*, Springer, USA, **1997**.

[8] A. J. Koch, H. Meinhardt, Biological pattern formation: From basic mechanisms to complex structures, *Rev. Mod. Phys.,* **1994**, *66*, 1481-1507.

[9] M. Bode, H. G. Purwins, Pattern formation in reaction-diffusion systems - dissipative solitons in physical systems, *Phys. D,* **1995**, *86*, 53-63.

[10] F. Rossi, S. Ristori, M. Rustici, N. Marchettini, E. Tiezzi, Dynamics of pattern formation in biomimetic systems, *Journal of Theoretical Biology,* **2008**, *255*, 404-412.

[11] B. A. Grzybowski, K. Fitzner, J. Paczesny, S. Granick, From dynamic self-assembly to networked chemical systems, *Chemical Society Reviews,* **2017**, *46*, 5647-5678.

[12] B. A. Grzybowski, K. J. M. Bishop, C. J. Campbell, M. Fialkowski, S. K. Smoukov, Micro- and nanotechnology via reaction–diffusion, *Soft Matter,* **2005**, *1*, 114-128.

[13] F. Sagués, I. R. Epstein, Nonlinear chemical dynamics, *Dalton Trans.,* **2003**, 1201-1217.

[14] S. Kondo, R. Asai, A reaction–diffusion wave on the skin of the marine angelfish pomacanthus, *Nature,* **1995**, *376*, 765-768.

[15] S. Kondo, R. Asai, Turing patterns in fish skin?, *Nature,* **1996**, *380*, 678-678.

[16] A. Nakamasu, G. Takahashi, A. Kanbe, S. Kondo, Interactions between zebrafish pigment cells responsible for the generation of turing patterns, *Proc. Natl. Acad. Sci. U. S. A.,* **2009**, *106*, 8429 LP-8434.

[17] S. Kondo, T. Miura, Reaction-diffusion model as a framework for understanding

biological pattern formation, *Science,* **2010**, *329*, 1616.

[18] K. Asakura, R. Konishi, T. Nakatani, T. Nakano, M. Kamata, Turing pattern formation by the cima reaction in a chemical system consisting of quaternary alkyl ammonium cationic groups, *J. Phys. Chem. B,* **2011**, *115*, 3959-3963.

[19] R. E. Liesegang, Ueber einige eigenschaften von gallerten, *Naturwissenschaftliche Wochenschrift,* **1896**, *11*, 353-362.

[20] H. Nabika, M. Itatani, I. Lagzi, Pattern formation in precipitation reactions: The liesegang phenomenon, *Langmuir,* **2020**, *36*, 481-497.

[21] T. Hidejima, *Science of non-equilibrium systems vi oscillatory reactions in living systems, Vol. 1*, Kodansha Scientific Co., Ltd., Japan, **2002**.

[22] P. D. P. Atkins, Julio, *Atkins' physical chemistry 10th edition*, Oxford University Press, USA, **2014**.

[23] A. Sorrenti, J. Leira-Iglesias, A. J. Markvoort, T. F. A. de Greef, T. M. Hermans, Non-equilibrium supramolecular polymerization, *Chemical Society Reviews,* **2017**, *46*, 5476-5490.

[24] E. Bodenschatz, W. Pesch, G. Ahlers, Recent developments in rayleigh-bénard convection, *Annual Review of Fluid Mechanics,* **2000**, *32*, 709-778.

[25] L. P. Kadanoff, Turbulent heat flow: Structures and scaling, *Physics Today,* **2001**, *54*, 34-39.

[26] D. J. Tritton, *Physical fluid dynamics*, Oxford University Press, England, **1988**.

[27] M. Kavallaris, Microtubules and resistance to tubulin-binding agents, *Nature Reviews Cancer,* **2010**, *10*, 194-204.

[28] C. G. Nunalee, S. Basu, On the periodicity of atmospheric von kármán vortex streets, *Environmental Fluid Mechanics,* **2014**, *14*, 1335-1355.

[29] I. R. Epstein, B. Xu, Reaction–diffusion processes at the nano- and microscales, *Nat. Nanotechnol.,* **2016**, *11*, 312-319.

[30] H. M. Miike, Yoshihito; Yamaguchi, Tomohiko, *Science of non-equilibrium systems iii dynamics of reaction and diffusion systems, Vol. 1*, Kodansha Scientific Co., Ltd., Japan, **1998**.

[31] B. A. Grzybowski, *Chemistry in motion: Reaction-diffusion systems for micro- and nanotechnology, Vol. 1*, Wiley, USA, **2009**.

[32] C. Vilas, M. R. García, J. R. Banga, A. A. Alonso, Robust feed-back control of travelling waves in a class of reaction–diffusion distributed biological systems, *Phys. D,* **2008**, *237*, 2353-2364.

[33] K. K. Chiou, J. W. Rocks, C. Y. Chen, S. Cho, K. E. Merkus, A. Rajaratnam, P. Robison, M. Tewari, K. Vogel, S. F. Majkut, B. L. Prosser, D. E. Discher, A. J. Liu,

Mechanical signaling coordinates the embryonic heartbeat, *Proc. Natl. Acad. Sci. U. S. A.,* **2016**, *113*, 8939-8944.

[34] A. M. Turing, The chemical basis of morphogenesis, *Philosophical Transactions of the Royal Society of London. Series B, Biological Sciences,* **1952**, *237*, 37-72.

[35] R. J. Field, E. Koros, R. M. Noyes, Oscillations in chemical systems. Ii. Thorough analysis of temporal oscillation in the bromate-cerium-malonic acid system, *J. Am. Chem. Soc.,* **1972**, *94*, 8649-8664.

[36] A. M. Zhabotinskii, [periodic course of the oxidation of malonic acid in a solution (studies on the kinetics of beolusov's reaction)], *Biofizika,* **1964**, *9*, 306-311.

[37] B. Belousov, Collection of short papers on radiation medicine for 1958, chapter a periodic reaction and its mechanism, *Moscow: Med. Publ.[in Russian],* **1959**.

[38] J. Horváth, I. Szalai, P. De Kepper, An experimental design method leading to chemical turing patterns, *Science,* **2009**, *324*, 772.

[39] K. Torbensen, F. Rossi, S. Ristori, A. Abou-Hassan, Chemical communication and dynamics of droplet emulsions in networks of belousov–zhabotinsky micro-oscillators produced by microfluidics, *Lab on a Chip,* **2017**, *17*, 1179-1189.

[40] R. Yoshida, Self-oscillating gels driven by the belousov–zhabotinsky reaction as novel smart materials, *Adv. Mater.,* **2010**, *22*, 3463-3483.

[41] K. Inui, I. Saito, R. Yoshida, H. Minato, D. Suzuki, High-frequency swelling/deswelling oscillation of poly(oligoethylene glycol) methacrylate-based hydrogel microspheres with a tris(2,2′-bipyridyl)ruthenium catalyst, *ACS Applied Polymer Materials,* **2021**, *3*, 3298-3306.

[42] M. Orbán, K. Kurin-Csörgei, I. R. Epstein, Ph-regulated chemical oscillators, *Accounts of Chemical Research,* **2015**, *48*, 593-601.

[43] R. J. Field, R. M. Noyes, Oscillations in chemical systems. Iv. Limit cycle behavior in a model of a real chemical reaction, *J. Chem. Phys.,* **1974**, *60*, 1877-1884.

[44] R. Peng, M. Wang, Pattern formation in the brusselator system, *Journal of Mathematical Analysis and Applications,* **2005**, *309*, 151-166.

[45] V. K. Vanag, I. R. Epstein, Pattern formation in a tunable medium: The belousov-zhabotinsky reaction in an aerosol ot microemulsion, *Phys. Rev. Lett.,* **2001**, *87*, 228301.

[46] V. K. Vanag, I. R. Epstein, A model for jumping and bubble waves in the belousov–zhabotinsky-aerosol ot system, *J. Chem. Phys.,* **2009**, *131*, 104512.

[47] V. K. Vanag, I. R. Epstein, Design and control of patterns in reaction-diffusion systems, *Chaos: An Interdisciplinary Journal of Nonlinear Science,* **2008**, *18*,

026107.

[48] J. Ai, C. Zhai, W. Sun, Study on the formation of complex chemical waveforms by different computational methods, *Processes,* **2020**, *8*, 393.

[49] N. J. Suematsu, Y. Mori, T. Amemiya, S. Nakata, Oscillation of speed of a self-propelled belousov–zhabotinsky droplet, *The Journal of Physical Chemistry Letters,* **2016**, *7*, 3424-3428.

[50] N. J. Suematsu, K. Saikusa, T. Nagata, S. Izumi, Interfacial dynamics in the spontaneous motion of an aqueous droplet, *Langmuir,* **2019**, *35*, 11601-11607.

[51] N. J. Suematsu, Y. Mori, T. Amemiya, S. Nakata, Spontaneous mode switching of self-propelled droplet motion induced by a clock reaction in the belousov–zhabotinsky medium, *The Journal of Physical Chemistry Letters,* **2021**, *12*, 7526-7530.

[52] K. U. Torii, Two-dimensional spatial patterning in developmental systems, *Trends in Cell Biology,* **2012**, *22*, 438-446.

[53] P. Gray, S. K. Scott, Autocatalytic reactions in the isothermal, continuous stirred tank reactor: Oscillations and instabilities in the system a + 2b → 3b; b → c, *Chem. Eng. Sci.,* **1984**, *39*, 1087-1097.

[54] F. W. Schneider, A. F. Muenster, Chemical oscillations, chaos, and fluctuations in flow reactors, *The Journal of Physical Chemistry,* **1991**, *95*, 2130-2138.

[55] A. Fick, Ueber diffusion, *Annalen der Physik,* **1855**, *170*, 59-86.

[56] C. Jablczynski, The rhythmic formation of precipitates liesegang rings, *Bull. Soc. Chim. France,* **1923**, *33*, 1592-1602.

[57] Z. Shreif, L. Mandalian, A. Abi-Haydar, R. Sultan, Taming ring morphology in 2d co(oh)2 liesegang patterns, *Physical Chemistry Chemical Physics,* **2004**, *6*, 3461-3466.

[58] M. Itatani, Q. Fang, K. Unoura, H. Nabika, Programmable design of self-organized patterns through a precipitation reaction, *J. Phys. Chem. B,* **2020**, *124*, 8402-8409.

[59] M. Matsue, M. Itatani, Q. Fang, Y. Shimizu, K. Unoura, H. Nabika, Role of electrolyte in liesegang pattern formation, *Langmuir,* **2018**, *34*, 11188-11194.

[60] M. Itatani, Q. Fang, K. Unoura, H. Nabika, Role of nuclei in liesegang pattern formation: Insights from experiment and reaction-diffusion simulation, *J. Phys. Chem. C,* **2018**, *122*, 3669-3676.

[61] R. Matalon, A. Packter, The liesegang phenomenon. I. Sol protection and diffusion, *Journal of Colloid Science,* **1955**, *10*, 46-62.

[62] T. Antal, M. Droz, J. Magnin, Z. Rácz, M. Zrinyi, Derivation of the matalon-

packter law for liesegang patterns, *J. Chem. Phys.,* **1998**, *109*, 9479-9486.

[63] M. Itatani, Q. Fang, H. Nabika, Modification of the matalon–packter law for self-organized periodic precipitation patterns by incorporating time-dependent diffusion flux, *J. Phys. Chem. B,* **2021**, *125*, 6921-6929.

[64] S. Thomas, F. Molnár, Z. Rácz, I. Lagzi, Matalon–packter law for stretched helicoids formed in precipitation processes, *Chem. Phys. Lett.,* **2013**, *577*, 38-41.

[65] É. Kárpáti-Smidróczki, A. Büki, M. Zrínyi, Pattern forming precipitation in gels due to coupling of chemical reactions with diffusion, *Colloid and Polymer Science,* **1995**, *273*, 857-865.

[66] R. Sultan, R. Halabieh, Effect of an electric field on propagating co(oh)2 liesegang patterns, *Chem. Phys. Lett.,* **2000**, *332*, 331-338.

[67] A. Büki, É. Kárpáti-Smidróczki, M. Zrínyi, Computer simulation of regular liesegang structures, *J. Chem. Phys.,* **1995**, *103*, 10387-10392.

[68] M. Fialkowski, A. Bitner, B. A. Grzybowski, Wave optics of liesegang rings, *Phys Rev Lett,* **2005**, *94*, 018303.

[69] L. Badr, R. Sultan, Ring morphology and ph effects in 2d and 1d co(oh)2 liesegang systems, *J. Phys. Chem. A,* **2009**, *113*, 6581-6586.

[70] I. Lagzi, D. Ueyama, Pattern transition between periodic liesegang pattern and crystal growth regime in reaction–diffusion systems, *Chem. Phys. Lett.,* **2009**, *468*, 188-192.

[71] I. Lagzi, Controlling and engineering precipitation patterns, *Langmuir,* **2012**, *28*, 3350-3354.

[72] I. Bena, M. Droz, Z. Rácz, Formation of liesegang patterns in the presence of an electric field, *J. Chem. Phys.,* **2005**, *122*, 204502.

[73] L. Badr, H. El-Rassy, S. El-Joubeily, R. Sultan, Morphology of a 2d mg2+/nh4oh liesegang pattern in zero, positive and negative radial electric field, *Chem. Phys. Lett.,* **2010**, *492*, 35-39.

[74] H. W. Morse, G. W. Pierce, Diffusion und übersättigung in gelatine, *Zeitschrift für Physikalische Chemie,* **1903**, *45*, 589-607.

[75] I. Lagzi, A. Volford, A. Büki, Effect of geometry on the time law of liesegang patterning, *Chem. Phys. Lett.,* **2004**, *396*, 97-101.

[76] S. C. Mueller, S. Kai, J. Ross, Periodic precipitation patterns in the presence of concentration gradients. 1. Dependence on ion product and concentration difference, *The Journal of Physical Chemistry,* **1982**, *86*, 4078-4087.

[77] M. Droz, J. Magnin, M. Zrinyi, Liesegang patterns: Studies on the width law, *J. Chem. Phys.,* **1999**, *110*, 9618-9622.

[78] H. Batlouni, M. Al-Ghoul, Experimental study of the dynamics of front propagation in the co(oh)2/nh4oh liesegang system using spectrophotometry, *J. Phys. Chem. A,* **2008**, *112*, 8038-8045.

[79] I. T. Bensemann, M. Fialkowski, B. A. Grzybowski, Wet stamping of microscale periodic precipitation patterns, *J. Phys. Chem. B,* **2005**, *109*, 2774-2778.

[80] R. Klajn, M. Fialkowski, I. T. Bensemann, A. Bitner, C. J. Campbell, K. Bishop, S. Smoukov, B. A. Grzybowski, Multicolour micropatterning of thin films of dry gels, *Nature Materials,* **2004**, *3*, 729-735.

[81] S. K. Smoukov, A. Bitner, C. J. Campbell, K. Kandere-Grzybowska, B. A. Grzybowski, Nano- and microscopic surface wrinkles of linearly increasing heights prepared by periodic precipitation, *J. Am. Chem. Soc.,* **2005**, *127*, 17803-17807.

[82] H. Nabika, M. Sato, K. Unoura, Liesegang patterns engineered by a chemical reaction assisted by complex formation, *Langmuir,* **2014**, *30*, 5047-5051.

[83] J. Jiang, K. Sakurai, Formation of ultrathin liesegang patterns, *Langmuir,* **2016**, *32*, 9126-9134.

[84] A. Sahu, B. B. Kanrar, D. Panda, Evolution of micron-spaced patterns within precipitating patterns of in situ synthesized silver nanoparticles in a nanodot-embedded pva/pvp film, *Langmuir,* **2021**, *37*, 4460-4467.

[85] L. Badr, Z. Moussa, A. Hariri, R. Sultan, Band, target, and onion patterns in $Co(OH)_2$ liesegang systems, *Phys. Rev. E,* **2011**, *83*, 016109.

[86] S. Thomas, I. Lagzi, F. Molnár, Z. Rácz, Helices in the wake of precipitation fronts, *Phys. Rev. E,* **2013**, *88*, 022141.

[87] C. Pan, Q. Gao, J. Xie, Y. Xia, I. R. Epstein, Precipitation patterns with polygonal boundaries between electrolytes, *Phys Chem Chem Phys,* **2009**, *11*, 11033-11039.

[88] S. K. Smoukov, I. Lagzi, B. A. Grzybowski, Independence of primary and secondary structures in periodic precipitation patterns, *The Journal of Physical Chemistry Letters,* **2011**, *2*, 345-349.

[89] R. Toth, R. M. Walliser, I. Lagzi, F. Boudoire, M. Duggelin, A. Braun, C. E. Housecroft, E. C. Constable, Probing the mystery of liesegang band formation: Revealing the origin of self-organized dual-frequency micro and nanoparticle arrays, *Soft Matter,* **2016**, *12*, 8367-8374.

[90] I. Lagzi, B. Kowalczyk, B. A. Grzybowski, Liesegang rings engineered from charged nanoparticles, *J. Am. Chem. Soc.,* **2010**, *132*, 58-60.

[91] R. Zakhia Douaihy, M. Al-Ghoul, M. Hmadeh, Liesegang banding for controlled size and growth of zeolitic-imidazolate frameworks, *Small,* **2019**, *15*, 1901605.

[92] H. Hayashi, S. Aoki, T. Suzuki, Spontaneous precipitation pattern formation by crystallites of mn–fe-based prussian blue analogues in agarose gel, *RSC Adv.,* **2019**, *9*, 36240-36247.

[93] J. H. Park, J. Paczesny, N. Kim, B. A. Grzybowski, Shaping microcrystals of metal-organic frameworks by reaction-diffusion, *Angew. Chem. Int. Ed.,* **2020**, *59*, 10301-10305.

[94] Y. Shimizu, J. Matsui, K. Unoura, H. Nabika, Liesegang mechanism with a gradual phase transition, *J. Phys. Chem. B,* **2017**, *121*, 2495-2501.

[95] K. Sasaki, M. Itatani, D. Sato, K. Unoura, H. Nabika, Interplay between spinodal decomposition and gelation and their role in two- and three-dimensional pattern formation at the gelatin gel surface, *J. Phys. Chem. C,* **2019**, *123*, 13782-13788.

[96] D. Sato, M. Itatani, J. Matsui, K. Unoura, H. Nabika, Interplay between two radical species in the formation of periodic patterns during a polymerization reaction, *Physical Chemistry Chemical Physics,* **2020**, *22*, 21672-21677.

[97] A. J. Ackroyd, G. Holló, H. Mundoor, H. Zhang, O. Gang, I. I. Smalyukh, I. Lagzi, E. Kumacheva, Self-organization of nanoparticles and molecules in periodic liesegang-type structures, *Sci. Adv.,* **2021**, *7*, eabe3801.

[98] R. M. Walliser, F. Boudoire, E. Orosz, R. Tóth, A. Braun, E. C. Constable, Z. Rácz, I. Lagzi, Growth of nanoparticles and microparticles by controlled reaction-diffusion processes, *Langmuir,* **2015**, *31*, 1828-1834.

[99] M.-k. Jo, Y. S. Cho, G. Holló, J.-M. Choi, I. Lagzi, S. H. Yang, Spatiotemporal and microscopic analyses of asymmetric liesegang bands: Diffusion-limited crystallization of calcium phosphate in a hydrogel, *Crystal Growth & Design,* **2021**, *21*, 6119-6128.

[100] M. Itatani, Q. Fang, K. Unoura, H. Nabika, Effect of diffusion dimension on the geometry of precipitation patterns in the liesegang phenomenon, *ECS Transactions,* **2018**, *88*, 335-341.

[101] I. Lagzi, D. Kármán, Equidistant precipitate pattern formation behind a propagating chemical front, *Chem. Phys. Lett.,* **2003**, *372*, 831-835.

[102] F. Molnár, F. Izsák, I. Lagzi, Design of equidistant and revert type precipitation patterns in reaction–diffusion systems, *Physical chemistry chemical physics : PCCP,* **2008**, *10*, 2368-2373.

[103] I. Bena, M. Droz, I. Lagzi, K. Martens, Z. Rácz, A. Volford, Designed patterns: Flexible control of precipitation through electric currents, *Phys. Rev. Lett.,* **2008**, *101*, 075701.

[104] M. Morsali, M. T. A. Khan, R. Ashirov, G. Hollo, H. T. Baytekin, I. Lagzi, B.

Baytekin, Mechanical control of periodic precipitation in stretchable gels to retrieve information on elastic deformation and for the complex patterning of matter, *Adv. Mater.,* **2020**, *32*, e1905779.

[105] N. Kanniah, F. D. Gnanam, P. Ramasamy, G. S. Laddha, Revert and direct type liesegang phenomenon of silver iodide, *Journal of Colloid and Interface Science,* **1981**, *80*, 369-376.

[106] N. Kanniah, F. D. Gnanam, P. Ramasamy, Revert and direct liesegang phenomenon of silver iodide: Factors influencing the transition point, *Journal of Colloid and Interface Science,* **1983**, *94*, 412-420.

[107] N. Kanniah, F. D. Gnanam, P. Ramasamy, A new spacing law for liesegang rings, *Proceedings of the Indian Academy of Sciences - Chemical Sciences,* **1984**, *93*, 801-811.

[108] T. Karam, H. El-Rassy, R. Sultan, Mechanism of revert spacing in a pbcro4 liesegang system, *J. Phys. Chem. A,* **2011**, *115*, 2994-2998.

[109] L. Kalash, H. Farah, A. Z. Eddin, R. Sultan, Dynamical profiles of the reactive components in direct and revert liesegang patterns, *Chem. Phys. Lett.,* **2013**, *590*, 69-73.

[110] S. Sadek, R. Sultan, *Precipitation patterns in reaction-diffusion systems*, Research Signpost, India, **2010**.

[111] M. Msharrafieh, M. Al-Ghoul, F. Zaknoun, H. El-Rassy, S. El-Joubeily, R. Sultan, Simulation of geochemical banding i: Acidization-precipitation experiments in a ferruginous limestone rock, *Chem. Geol.,* **2016**, *440*, 42-49.

[112] M. Saad, A. Safieddine, R. Sultan, Revisited chaos in a diffusion–precipitation–redissolution liesegang system, *J. Phys. Chem. A,* **2018**, *122*, 6043-6047.

[113] A. Toramaru, K. Ito, S. Kai, The liesegang model of the titius-bode's law, *Forma,* **1991**, *6*, 247-266.

[114] G. T. Dee, Patterns produced by precipitation at a moving reaction front, *Phys. Rev. Lett.,* **1986**, *57*, 275-278.

[115] H.-J. Krug, H. Brandtstädter, Morphological characteristics of liesegang rings and their simulations, *J. Phys. Chem. A,* **1999**, *103*, 7811-7820.

[116] T. Antal, M. Droz, J. Magnin, Z. Rácz, Formation of liesegang patterns: A spinodal decomposition scenario, *Phys. Rev. Lett.,* **1999**, *83*, 2880-2883.

[117] Z. Rácz, Formation of liesegang patterns, *Phys. A,* **1999**, *274*, 50-59.

[118] J. W. Cahn, J. E. Hilliard, Free energy of a nonuniform system. I. Interfacial free energy, *J. Chem. Phys.,* **1958**, *28*, 258-267.

[119] J. W. Cahn, On spinodal decomposition, *Acta metall.,* **1961**, *9*, 795-801.

[120] P. C. Hohenberg, B. I. Halperin, Theory of dynamic critical phenomena, *Rev. Mod. Phys.,* **1977**, *49*, 435-479.

[121] N. T. K. Thanh, N. Maclean, S. Mahiddine, Mechanisms of nucleation and growth of nanoparticles in solution, *Chemical Reviews,* **2014**, *114*, 7610-7630.

[122] S. Shinohara, A theory of one-dimensional liesegang phenomena, *Journal of the Physical Society of Japan,* **1970**, *29*, 1073-1087.

[123] S. Thomas, I. Lagzi, F. Molnár, Z. Rácz, Probability of the emergence of helical precipitation patterns in the wake of reaction-diffusion fronts, *Phys. Rev. Lett.,* **2013**, *110*, 078303.

[124] M. Dayeh, M. Ammar, M. Al-Ghoul, Transition from rings to spots in a precipitation reaction–diffusion system, *RSC Adv.,* **2014**, *4*, 60034-60038.

[125] P. Papp, B. Bohner, Á. Tóth, D. Horváth, Fine tuning of pattern selection in the cadmium–hydroxide-system, *J. Chem. Phys.,* **2020**, *152*, 094906.

[126] B. Derjaguin, L. Landau, Theory of the stability of strongly charged lyophobic sols and of the adhesion of strongly charged particles in solutions of electrolytes, *Progress in Surface Science,* **1993**, *43*, 30-59.

[127] J. Israelachvili, *Intermolecular and surface forces*, Academic Press, United States, **2011**.

[128] S. D. Kulkarni, A. Rashid Mir, P. S. Kulkarni, Periodic precipitation of cobalt hydroxide in agar gel: Effect of ionic strength, *Journal of Molecular Liquids,* **2017**, *241*, 37-42.

[129] T. Antal, I. Bena, M. Droz, K. Martens, Z. Rácz, Guiding fields for phase separation: Controlling liesegang patterns, *Phys. Rev. E,* **2007**, *76*, 046203.

[130] H. Furukawa, Phase separation by directional quenching and morphological transition, *Phys. A,* **1992**, *180*, 128-155.

[131] R. Kurita, Control of pattern formation during phase separation initiated by a propagated trigger, *Sci. Rep.,* **2017**, *7*, 6912.

[132] M. Morsali, M. T. A. Khan, R. Ashirov, G. Hollo, H. T. Baytekin, I. Lagzi, B. Baytekin, Mechanical control of periodic precipitation in stretchable gels to retrieve information on elastic deformation and for the complex patterning of matter, *Adv. Mater.,* **2020**, *32*, e1905779.

[133] H. K. Henisch, J. M. García-Ruiz, Crystal growth in gels and liesegang ring formation: I. Diffusion relationships, *Journal of Crystal Growth,* **1986**, *75*, 195-202.

[134] M. Maaloum, N. Pernodet, B. Tinland, Agarose gel structure using atomic force microscopy: Gel concentration and ionic strength effects, *Electrophoresis,* **1998**,

19, 1606-1610.

[135] L. Huang, C. H. Yu, P. K. Hopke, J. Y. Shin, Z. Fan, Trivalent chromium solubility and its influence on quantification of hexavalent chromium in ambient particulate matter using epa method 6800, *Journal of the Air & Waste Management Association,* **2014**, *64*, 1439-1445.

[136] D. Chen, Z. Lewandowski, F. Roe, P. Surapaneni, Diffusivity of cu2+ in calcium alginate gel beads, *Biotechnology and Bioengineering,* **1993**, *41*, 755-760.

[137] A. C. F. Ribeiro, M. A. Esteso, V. M. M. Lobo, A. J. M. Valente, S. M. N. Simões, A. J. F. N. Sobral, H. D. Burrows, Diffusion coefficients of copper chloride in aqueous solutions at 298.15 k and 310.15 k, *Journal of Chemical & Engineering Data,* **2005**, *50*, 1986-1990.

[138] S. D. Kulkarni, P. C. Walimbe, R. B. Ingulkar, J. D. Lahase, P. S. Kulkarni, Revert banding in one-dimensional periodic precipitation of the (agno3 + kbr) system in agar gel, *ACS Omega,* **2019**, *4*, 13061-13068.

[139] D. Ezzeddine, H. El-Rassy, R. Sultan, Surface and structural studies in a pbcro4 liesegang pattern with revert spacing, *Chem. Phys. Lett.,* **2019**, *734*, 136735.

[140] R. M. L. Kettler, D. B.; Weber, K. a.; Niles, P. B., Life and liesegang: Outcrop-scale microbially induced diagenetic structures and geochemical self-organization phenomena produced by oxidation of reduced iron, *Astrobiology,* **2015**, *15*, 616-636.

[141] A. Toramaru, A. Iochi, Transition between periodic precipitation and tree-like crystal aggregates, *Journal of the Mineralogical Society of Japan,* **1996**, *26*, 103-106.

[142] M. R. Letherby, D. A. Young, The gelation of agarose, *Journal of the Chemical Society, Faraday Transactions 1: Physical Chemistry in Condensed Phases,* **1981**, *77*, 1953-1966.

[143] V. Normand, D. L. Lootens, E. Amici, K. P. Plucknett, P. Aymard, New insight into agarose gel mechanical properties, *Biomacromolecules,* **2000**, *1*, 730-738.

[144] K. Nishinari, Y. Fang, Relation between structure and rheological/thermal properties of agar. A mini-review on the effect of alkali treatment and the role of agaropectin, *Food Structure,* **2017**, *13*, 24-34.

[145] M. Takahashi, H. Takeuchi, Concentration distribution of ions for diffusion with chemical reaction in agar-agar gel, *Nippon Kagaku Kaishi,* **1977**, *1977*, 1395-1399.

[146] I. Lheureux, Oscillatory zoning in crystal-growth - a constitutional undercooling mechanism, *Phys. Rev. E,* **1993**, *48*, 4460-4469.

[147] T. Holten, B. Jamtveit, P. Meakin, M. Cortini, J. Blundy, H. Austrheim, Statistical characteristics and origin of oscillatory zoning in crystals, *Am. Mineral.,* **1997**, *82*, 596-606.

[148] C. Hayashi, K. Nakazawa, Y. Nakagawa, Formation of the solar system, *Protostars and planets II,* **1985**, 1100-1153.

[149] Y. Chen, C. Mao, Ph-induced reversible expansion/contraction of gold nanoparticle aggregates, *Small,* **2008**, *4*, 2191-2194.

[150] J. Nam, N. Won, H. Jin, H. Chung, S. Kim, Ph-induced aggregation of gold nanoparticles for photothermal cancer therapy, *J. Am. Chem. Soc.,* **2009**, *131*, 13639-13645.

[151] I. Lagzi, B. Kowalczyk, D. Wang, B. A. Grzybowski, Nanoparticle oscillations and fronts, *Angew. Chem. Int. Ed.,* **2010**, *49*, 8616-8619.

[152] S. M. Ansar, S. Chakraborty, C. L. Kitchens, Ph-responsive mercaptoundecanoic acid functionalized gold nanoparticles and applications in catalysis, *Nanomaterials,* **2018**, *8*, 339.

[153] M. Chirea, C. M. Pereira, F. Silva, Catalytic effect of gold nanoparticles self-assembled in multilayered polyelectrolyte films, *J. Phys. Chem. C,* **2007**, *111*, 9255-9266.

[154] G. Sener, L. Uzun, A. Denizli, Colorimetric sensor array based on gold nanoparticles and amino acids for identification of toxic metal ions in water, *ACS Applied Materials & Interfaces,* **2014**, *6*, 18395-18400.

[155] T. Morais, M. E. Soares, J. A. Duarte, L. Soares, S. Maia, P. Gomes, E. Pereira, S. Fraga, H. Carmo, M. d. L. Bastos, Effect of surface coating on the biodistribution profile of gold nanoparticles in the rat, *European Journal of Pharmaceutics and Biopharmaceutics,* **2012**, *80*, 185-193.

[156] J. Piella, N. G. Bastús, V. Puntes, Size-controlled synthesis of sub-10-nanometer citrate-stabilized gold nanoparticles and related optical properties, *Chem. Mater.,* **2016**, *28*, 1066-1075.

[157] X. Liu, M. Atwater, J. Wang, Q. Huo, Extinction coefficient of gold nanoparticles with different sizes and different capping ligands, *Colloids and Surfaces B: Biointerfaces,* **2007**, *58*, 3-7.

[158] G. Charron, D. Hühn, A. Perrier, L. Cordier, C. J. Pickett, T. Nann, W. J. Parak, On the use of ph titration to quantitatively characterize colloidal nanoparticles, *Langmuir,* **2012**, *28*, 15141-15149.

[159] D. Wang, R. J. Nap, I. Lagzi, B. Kowalczyk, S. Han, B. A. Grzybowski, I. Szleifer, How and why nanoparticle's curvature regulates the apparent pka of the coating

ligands, *J. Am. Chem. Soc.,* **2011**, *133*, 2192-2197.

[160] H. Nabika, T. Oikawa, K. Iwasaki, K. Murakoshi, K. Unoura, Dynamics of gold nanoparticle assembly and disassembly induced by ph oscillations, *J. Phys. Chem. C,* **2012**, *116*, 6153-6158.

[161] H. Nakanishi, A. Deák, G. Hólló, I. Lagzi, Existence of a precipitation threshold in the electrostatic precipitation of oppositely charged nanoparticles, *Angew. Chem. Int. Ed.,* **2018**, *57*, 16062-16066.

[162] N. Fatin-Rouge, K. Starchev, J. Buffle, Size effects on diffusion processes within agarose gels, *Biophys. J.,* **2004**, *86*, 2710-2719.

[163] K. K. Senanayake, E. A. Fakhrabadi, M. W. Liberatore, A. Mukhopadhyay, Diffusion of nanoparticles in entangled poly(vinyl alcohol) solutions and gels, *Macromolecules,* **2019**, *52*, 787-795.

[164] I. Zhang, C. P. Royall, M. A. Faers, P. Bartlett, Phase separation dynamics in colloid–polymer mixtures: The effect of interaction range, *Soft Matter,* **2013**, *9*, 2076-2084.

[165] E. B. Nauman, D. Q. He, Nonlinear diffusion and phase separation, *Chem. Eng. Sci.,* **2001**, *56*, 1999-2018.

Publication list

Chapter 2

Masaki Itatani, Qing Fang, and Hideki Nabika,
"Modification of the Matalon–Packter Law for Self-Organized Periodic Precipitation Patterns by Incorporating Time-Dependent Diffusion Flux",
J. Phys. Chem. B, **125**(25), 6921-6929 (2021).

Chapter 3

Masaki Itatani, Qing Fang, István Lagzi, and Hideki Nabika,
"Programmable Design of Self-Organized Patterns through a Precipitation Reaction",
J. Phys. Chem. B, **124**(38), 8402-8409 (2020).

Chapter 4

Masaki Itatani, Qing Fang, István Lagzi, and Hideki Nabika,
"Phase Separation Mechanism for a Unified Understanding of Dissipative Pattern Formation in a Liesegang System",
Phys. Chem. Chem. Phys., **24**, 2088-2092 (2022).

Related Publications

Masaki Itatani and Hideki Nabika,
"Self-propelled Motion of an Oil Droplet Containing a Phospholipid and its Stability in Collectivity",
Front. Phys., (submitted).

Szabolcs Farkas, Gábor Holló, Gabor Schuszter, Ágota Deák, László Janovák, Viktoria Hornok, **Masaki Itatani**, Hideki Nabika, Dezsö Horváth, Ágota Tóth, and István Lagzi,
"Reaction-Diffusion Assisted Synthesis of Gold Nanoparticles: Route from the Spherical Nano-Sized Particles to Micrometer-Sized Plates",
J. Phys. Chem. C, **125**(47), 8402-8409 (2021).

Masaki Itatani, Qing Fang, and Hideki Nabika,
"Role of Nucleation Process in Formation of Self-Organized Periodic Precipitation Patterns",

Bull .Nano. Sci. Tech., **20**(1), (2021).

Shun Sakamoto, **Masaki Itatani**, Kanta Tsukada, and Hideki Nabika,
"Regular-Type Liesegang Pattern of AgCl in a One-Dimensional System",
Materials, **14**(6), 1526 (2021).

Daisuke Sato, **Masaki Itatani**, Qing Fang, Kei Unoura, and Hideki Nabika,
"Interplay between Two Radical Species in the Formation of Periodic Patterns during a Polymerization Reaction",
Phys. Chem. Chem. Phys., **22**, 21672-21677 (2020).

Hideki Nabika, **Masaki Itatani**, and István Lagzi,
"Pattern Formation in Precipitation Reactions: The Liesegang Phenomenon",
Langmuir, **36**(2), 481-497 (2019).

Kazuto Sasaki, **Masaki Itatani**, Daisuke Sato, Qing Fang, Kei Unoura, and Hideki Nabika,
"Interplay between Spinodal Decomposition and Gelation and Their Role in Two- and Three-Dimensional Pattern Formation at the Gelatin Gel Surface",
J. Phys. Chem. C, **123**(22), 13782-13788 (2019).

Masaki Itatani, Qing Fang, Kei Unoura, and Hideki Nabika,
"Effect of Diffusion Dimension on the Geometry of Precipitation Patterns in the Liesegang Phenomenon",
ECS Trans., **88**(1), 335-341 (2018).

Masayo Matsue, **Masaki Itatani**, Qing Fang, Kei Unoura, and Hideki Nabika,
"Role of Electrolyte in Liesegang Pattern Formation",
Langmuir, **34**(37), 11188-11194 (2018).

Masaki Itatani, Qing Fang, Kei Unoura, and Hideki Nabika,
"Role of Nuclei in Liesegang Pattern Formation: Insights from Experiment and Reaction-Diffusion Simulation",
J. Phys. Chem. C, **122**(2), 3669-3676 (2018).